SANDIA REPORT

SAND2002-1395
Unlimited Release
Printed May 2002

Stochastic Modeling of Fracture Frequency along a Cross-Section at the MIU Site, Tono Region, Japan

Christopher A. Rautman and Sean A. McKenna

Prepared by
Sandia National Laboratories
Albuquerque, New Mexico 87185 and Livermore, California 94550

Sandia is a multiprogram laboratory operated by Sandia Corporation, a Lockheed Martin Company, for the United States Department of Energy under Contract DE-AC04-94AL85000.

Issued by Sandia National Laboratories, operated for the United States Department of Energy by Sandia Corporation.

SAND2002-1395
Unlimited Release
Printed May 2002

Stochastic Modeling of Fracture Frequency along a Cross-Section at the MIU Site, Tono Region, Japan

Christopher A. Rautman, Sean A. McKenna
Underground Storage Technology Department

Sean A. McKenna
Geohydrology Department

Sandia National Laboratories
P. O. Box 5800
Albuquerque, New Mexico 87185

ABSTRACT

Four hypothetical drilling sequences have been defined to examine the effects of the sequential addition of actual, drill-hole-derived information regarding fracture frequency in granitic rocks along a north–south, two-dimensional cross section one kilometer long and two kilometers deep. The cross section passes near the future location of the MIU research facility site in central Japan. Beginning with a pre-drilling situation, in which the only available information on fracture frequency in the subsurface is based on outcrop fracture-mapping studies, measured fracture frequency data from four deep boreholes are added, one drill hole at a time, and the fracture frequencies throughout the entire modeled domain are modeled probabilistically using geostatistical techniques.

Uncertainty is defined empirically as variability among members of a particular suite of geostatistical realizations generated by sequential Gaussian simulation and has been demonstrated to vary spatially. Uncertainty has also been summarized on a global basis. Spatial variability of uncertainty among different realizations for a particular modeling case is in part a function of knowledge regarding the position of the Tsukiyoshi Fault in the subsurface. The exact position of the fault trace at depth is uncertain unless and until that fault plane is penetrated in one or more boreholes. The position of the fault in the subsurface is modeled stochastically, with a variety of potential fault dips bounded by geologically and geophysically inferred limits and with a modal expectation identical to the dip of the fault in outcrop.

A number of interpretive conclusions and potential implications for the conduct of actual drilling campaigns result from this modeling activity. First, the global uncertainty measures exhibit a progressive decrease with successive additions of information based on the drill-hole-

based measurements of fracture frequency. This is essentially as expected, although the magnitude of the decrease was less than anticipated.

Second and perhaps most importantly, knowledge of the correct spatial continuity structure model (variogram) exerts a profound control on both spatially distributed and global uncertainty. Prior assumption of an apparently inaccurate anisotropy ratio in the range of spatial correlation in the horizontal and vertical directions for the pre-drilling case led to a situation in which progressive correction of the variogram model by the addition of more drilling information roughly offset the reductions in uncertainty related to the presence of that additional conditioning data. This second observation implies that pre-drilling site characterization activities (potentially geophysically based or more intensive studies of surface outcrops) to determine the approximately correct spatial continuity model may have significant informational value.

A third observation is that accurate knowledge of the actual magnitude and univariate distribution (histogram) of fracture frequency in the subsurface is important and affects the global uncertainty measures. Pre-drilling information based on outcrop measurements appear to have provided a significantly biased estimate of the in-situ fracture frequencies. The implication that accurate pre-drilling information regarding the phenomenon under investigation is highly desirable to avoid offsetting the direct information gains from drilling by revisions to the underlying conceptual model.

A fourth observation is that precise determination of the subsurface location of the Tsukiyoshi fault, a major control on fracture intensity in the subsurface, exhibited less control on the global uncertainty measures than intuitively anticipated beforehand. Local, location-specific uncertainty (in contrast to global uncertainty), however, is profoundly influenced by the degree of certainty constraining the Tsukiyoshi Fault in the subsurface.

ACKNOWLEDGMENTS

The work described in this report was funded by the Japan Nuclear Cycle Development Institute (JNC) through an agreement with Sandia National Laboratories. We acknowledge the efforts of Masao Shiotsuki and Masahiro Uchida for their roles in making the cooperative agreement happen. The authors are appreciative of the guidance and helpful comments provided by Shinji Takeuchi, Katsushi Nakano, Hiromitsu Saeugusa, Katsuhiko Maeda, Toshiyuki Matsuoka and Kaoru Inaba. S.J. Altman at Sandia reviewed an earlier version of this manuscript and provided helpful comments.

Sandia is a multiprogram laboratory operated by Sandia Corporation, a Lockheed Martin Company, for the United States Department of Energy under Contract DE-AC04-94AL85000.

CONTENTS

FIGURES

TABLES

EXECUTIVE SUMMARY

Summary of Modeling Activities

Four hypothetical drilling sequences have been defined to examine the effects of the sequential addition of drill-hole-derived information regarding fracture frequency in granitic rocks at the future location of the MIU research facility site in central Japan. Beginning with a pre-drilling situation, in which the only available information on fracture frequency in the subsurface is based on outcrop fracture-mapping studies, measured fracture frequency data from deep boreholes are added, one drill hole at a time, and the fracture frequencies throughout the entire modeled domain are modeled probabilistically using geostatistical techniques.

The geostatistical algorithm of sequential Gaussian simulation has been employed for this modeling and uncertainty-assessment exercise. Following identification (or assumption) of the spatial correlation structure for a given modeling case, 100 equally likely, replicate realizations of fracture frequency, conditioned to the available drill hole measurements (if any), were generated and post-processed to yield both a model of "expected" fracture frequency for the domain and of the uncertainty associated with that expected-value model. Uncertainty in this case is defined as the variability across the 100 individual simulated models for each modeling case.

Uncertainty, or variability among members of a particular suite of geostatistical realizations, has been demonstrated to vary spatially. Uncertainty is effectively zero at the location(s) of conditioning data, specifically at boreholes, in that a *measured* value of, for example, 6 fractures per meter is not subject to *modeling* uncertainty. Uncertainty is large at great distances from conditioning data, and the specific spatial patterns of uncertainty distribution surrounding and in between boreholes is dependent upon both the data locations and the spatial continuity (variogram) model identified from the data.

Spatial variability of uncertainty among different realizations for a particular modeling case is also a function of knowledge regarding the position of the Tsukiyoshi Fault in the subsurface. The surface location of the fault trace is known, as well as the dip of the fault in outcrop. However, the exact position of the fault trace at depths of up to 2 km in the subsurface is uncertain unless and until that fault plane is penetrated in one or more boreholes. Three of the hypothetical drilling sequences identify the fault at depth in the first drill hole (borehole MIU-3). The fourth drilling sequence does not identify the precise subsurface position of the Tsukiyoshi Fault until addition of the final borehole. For both this fourth drilling sequence and the pre-drilling case for which no drill-hole information exists, the position of the fault is modeled stochastically, with a variety of potential fault dips bounded by geologically and geophysically inferred limits and with a modal expectation identical to the dip of the fault in outcrop. Spatial contrasts in uncertainty between modeling cases involving stochastic fault-prior models and those with a deterministic fault-prior model are considerable.

Uncertainty has also been summarized on a "global" basis for each drilling and modeling case, both for the entire model domain as a whole and for the "drilled" quadrant. This distinction was presumed necessary in that only somewhat more than one-quarter of the entire domain was sampled (and conditioned in the simulation process) by drilling. Two different measures of global

uncertainty have been defined: one based on the standard deviation and one on concepts of the coefficient of variation. The two measures differ in absolute magnitude, but the coefficient-of-variation-based measure tends to discount the effect of statistical heteroscedasticity and locally varying prior expectations of variable fracture intensity by normalizing the standard deviations by the locally varying mean values.

Interpretive Conclusions and Implications

The geostatistical modeling activities involved in this analysis and generation of stochastic fracture-frequency models lead to some definite conclusions and implications for sequential drilling site-characterization activities. These are given below in list form for emphasis, with additional discussion interspersed.

1. *Comparison of the two global uncertainty measures for each drilling sequence indicates a common, progressive decrease in uncertainty from the pre-drilling (no subsurface data) case to lower values with the successive additions of information based on the drill-hole-obtained fracture-frequency measurements.*

Interestingly, the addition of even a single drill hole to any of the drilling sequences results in a marked reduction of global uncertainty, and the global uncertainty associated with the addition of more drill holes to the data sets decreases the global uncertainty disproportionately less.

2. *It is possible that it is the introduction of a layered background-fracture-frequency prior (based on the subsurface data from at least one drill hole, in the current instance) that is generating the "one-drill-hole" reduction in global uncertainty.*

It would be possible to test whether it is the presence of the layered (spatially-specific) prior frequency model alone that is driving the uncertainty reduction by generating a layered fault prior and generating a suite of simulations, but *not* explicitly introducing a conditioning drill hole data set. The results of this test might lead to conditional implication 3, below.

3. *If the uncertainty reduction is observed in the proposed numerical experiment, then it may be that geophysical investigations, or other remotely sensed data bearing on the subsurface fracture distribution for large vertical intervals of rock, would be of substantial value* prior *to drilling.*

Returning to the actual observations from modeling effort:

4. *It was demonstrated that there is a general lack of large, progressive reduction in uncertainty with increasing drill-hole data content. In other words, the additions of boreholes 2, 3, and 4 in each sequence did not produce an apparently proportional decrease in uncertainty compared with the addition of drill hole number 1.*

This lack of continued substantial reductions in global uncertainty is interpreted as follows. For the pre-drilling case, the only spatial correlation model that can be used is necessarily wholly assumed. For the cases involving one drill hole, a reasonable, measurement-based model

of spatial correlation can be developed in the vertical dimension, but the model of continuity in the horizontal dimension remains an assumed quantity. A somewhat arbitrary, and presumably (in retrospect) flawed *prior assumption* of horizontal-to-vertical anisotropy in the two ranges of spatial correlation affected the modeled ranges of horizontal correlation until quite late in the various drilling sequences, at which point, even the limited (sparse) experimental variogram computed in the horizontal dimension suggested a far shorter horizontal range of correlation than had been assumed a priori.

Thus, even though the "drilling" of additional boreholes in each hypothetical drilling sequence contributed more and more hard conditioning data, the revisions to the initial (unreasonably long-range) variogram models in the horizontal dimension meant that those additional measurements of fracture frequency exert a progressively diminishing sphere of influence within the model. The "plateau" of both global uncertainty measures across all drilling-related cases suggests that the drilling density thus far achieved at the MIU site, even within the drilled quadrant of the model, still is relatively insufficient to reduce global uncertainty to small values. The implication is:

5. *Knowledge of the correct spatial correlation structure (variogram) exerts a very pronounced control on the uncertainty of modeling based upon limited subsurface data. Specifically, revisions to the spatial continuity model may more-or-less* completely offset *gains in information content produced by direct subsurface data acquisition.* **Investments in estimating the correct spatial correlation model, and particularly in understanding the anisotropy between the ranges of correlation in different directions, should be particularly worthwhile** (see also item 9, below).

Demonstration of this implication, number 5, would be relatively easy (although time-consuming) to accomplish. One could simply rerun each of the modeling cases considered in this study using a prior assumption of *isotopic* spatial correlation patterns (variograms) instead of the anisotropic, 5:1 horizontal-to-vertical ratio assumed a priori in the present activities. We suspect that this closer approximation to the (apparently) true spatial correlation structure from the very beginning would indicate a much more substantial decrease in global uncertainty with the addition of each successive drill hole to the various drilling sequences.

The global uncertainty associated with each modeling case has been partitioned into a portion that is related to uncertainty in the prior models of fracture frequency, principally including uncertainty related to the position of the Tsukiyoshi Fault, and uncertainty associated with the simulation process and the incompleteness of data to condition the models.

6. *For modeling cases with a deterministic fault-prior model (Drilling Sequences 1, 2, and 3, as well as the final modeling case for Drilling Sequence 4), that portion of global uncertainty related to uncertainty in the fault is zero.*

7. *For Drilling Sequence 4, in which the position of the Tsukiyoshi Fault is progressively more constrained with each stage of drilling, the uncertainty associated with the fault-prior model decreases as more constraints on the location of the fault at depth are added***.**

However, the uncertainty associated with the simulation and with the available data has been observed to *increase* with the addition of more drill holes at the same time that the total uncertainty is decreasing. This counter-intuitive uncertainty behavior is attributed to the previously mentioned (item 5, above) changes in the spatial continuity model, or variogram, brought about by increased knowledge of spatial correlation patterns in the horizontal dimension associated with larger numbers of boreholes.

The most important contributors to *global* uncertainty that have been identified by this modeling exercise appear to be two-fold (items 8 and 9 below).

8. *The basic distribution of likely fracture frequencies (the histogram) was highly uncertain prior to drilling (as the only estimate available was from outcrop studies), and that pre-drilling estimate turned out to be (apparently) quite inconsistent in representing actual subsurface conditions. Recall, however, that the original fracture frequency data from outcrop were* not *in the desired form (units of* m^{-1}*), and that several assumptions were required to bring the available data (units of* m^{-2}*) into the required format.*

The standard-deviation global uncertainty measure is unquestionably greatest for Case 0, and is very much smaller for all drilling-related cases. This applies to both the full-field and the drilling-quadrant analyses. That a pronounced reduction of the standard-deviation based global uncertainty measure was obtained for Case 0a suggests that *a "reasonably accurate" global histogram is essential for a simulation-based study, in which the back-transformation of the simulated values is tied directly to that global histogram.* There is also clearly a heteroscedastic influence here, as the coefficient-of-variation-based global uncertainty measure for Case 0 was markedly different from the global uncertainty value based on the standard deviation. There is also a suspected influence of the locally varying mean incorporated into the prior estimates of fracture frequency (implication 2, above). Introduction of locally varying prior-estimated mean values definitely inserts spatial information into the modeling process, which might reasonably be expected to reduce global uncertainty. This effect was not directly investigated, however, and the existence of this effect was inferred based on indirect evidence.

9. *The broad form of the spatial continuity models were demonstrated to be very influential on the global uncertainty of the final simulated models. Specifically, the* prior assumption *of relatively strong horizontal-to-vertical anisotropy based on geological inference proved to be incorrect (or at least inconsistent with later data) in the light of more advanced drilling data. The revisions to the anisotropy ratio that came with more advanced stages of drilling appear to have offset most of the gains in information obtained through that drilling, with the* apparent *result that the net reduction in uncertainty across the sequential addition of four boreholes is essentially zero.* **This inference suggests that pre-drilling investigations directed toward confirming or eliminating gross anisotropy in the spatial correlation structure might have significant value.**

The impact of precisely locating the Tsukiyoshi fault in the subsurface was not as pronounced as might have been anticipated, at least on a global basis, as measured by our global uncertainty measures. However, the successive constraining of the fault location during Drilling

Sequence 4 clearly indicates some measure of progressive uncertainty reduction. Potentially the impact of a deterministic (Drilling Sequences 1–3) vs. a stochastic (Sequence 4) fault has been overshadowed in the modeling by the large error in assumed anisotropy ratio discussed in item 5, above. However:

10. *It is clear that identification of the precise position of the fault may have far-reaching consequences* with respect to location-specific issues, *in distinct contrast to a simple global evaluation of overall (non-location-specific) uncertainty.*

This page intentionally left blank.

Stochastic Modeling of Fracture Frequency along a Cross-Section at the MIU Site, Tono Region, Japan

INTRODUCTION

The Japanese Nuclear Cycle Development Institute (JNC) is constructing an underground research laboratory deep in granitic rocks at the MIU ("Mizunami") site near the town of Mizunami, Gifu Prefecture, approximately midway between Tokyo and Osaka, in central Japan (fig. 1). Sandia National Laboratories (Sandia, or SNL) is assisting JNC to develop, demonstrate, and apply probabilistic site characterization methodologies to the description of and other characterization activities at the MIU site. An ultimate goal of applying these probabilistic characterization and modeling methodologies is a quantitative assessment of uncertainty associated with various performance measures relevant to nuclear waste isolation, which is one of the justifications for the studies to be conducted at the MIU site.

Figure 1. Index map showing the location of the MIU site in central Japan.

As a part of this demonstration effort, Sandia has modeled fracture frequency along a vertical cross section through four deep drill holes in a stochastic (geostatistical) manner, with the objective of documenting the changes both in modeled fracture frequency values — and in the uncertainty in those modeled values — as a function of the sequence in which the boreholes were "drilled." In actual fact, all of the four drill holes existed at the time of the modeling exercise. However, only the information from the data available at a particular stage of the hypothetical "drilling" program were used in the construction of the models.

BACKGROUND GEOLOGY AND MODELING METHODOLOGY

Geologic Setting

Granitic intrusive rocks (Yusa and Yamakawa, 1992), known collectively as the Toki Granite of Cretaceous age, crop out in localized areas throughout an extensive region surrounding the MIU site, which is located near the town of Mizunami, Gifu Prefecture, in central Japan. The granites are generally relatively homogeneous, and medium to coarse grained, consisting of sub-equal portions of quartz, potassium feldspar, and plagioclase, with biotite and locally hornblende. Platy jointing is described as common. Outcrops of the granitic rocks are sparse in the immediate vicinity of the site because of extensive vegetation and surficial cover, but fracture frequencies have been measured at a total of six sites in the general vicinity of the proposed underground research laboratory. A Miocene sedimentary sequence, referred to as the Mizunami Group, typically about 200 m thick (Yusa and others, 1992) in the immediate vicinity of the MIU site, overlies the granitic rocks in part of the area and consists principally of arkosic sandstone and conglomerate derived from the Toki Granite, mudstones, and lignite-bearing sandstones and mudstones. The Mizunami Group becomes generally finer grained and more volcanic-rich (tuffaceous) upward.

Of specific relevance to the modeling exercise is the Tsukiyoshi Fault (figure 2), which runs approximately west-northwest to east-southeast a few hundreds of meters to the north of the proposed underground facility. The location of the Tsukiyoshi Fault with respect to the four existing drill holes (table 1) that were included in the frequency modeling study is shown in figure 2. Also shown in figure 2 is the location of the modeled cross section (the model domain). This two-dimensional, vertical profile is oriented north-south, runs directly through borehole MIU-2, and intersects the Tsukiyoshi Fault at an approximately 85-degree angle. As indicated on the figure, the various other boreholes have simply been projected east-west onto the line of cross section, as there is no particular structural reason within the massive granites for projecting in a different configuration.

Table 1: Location Data for Drill Holes Used in Modeling
[all measurements are in meters]

Drill Hole ID	X-Coordinate	Y-Coordinate	Surface Elevation	Total Depth
MIU-1	5488.83	-68629.36	220.07	1011.00
MIU-2	5433.30	-68552.40	223.76	1011.01
MIU-3	5340.23	-68455.29	230.48	1015.00
AN-1	5454.72	-68877.34	216.38	1008.71

Modeling Approach

The objectives of this modeling activity are two-fold:

1. to describe the uncertainty associated with our understanding of the spatial distribution of fracture frequency throughout the model domain, and

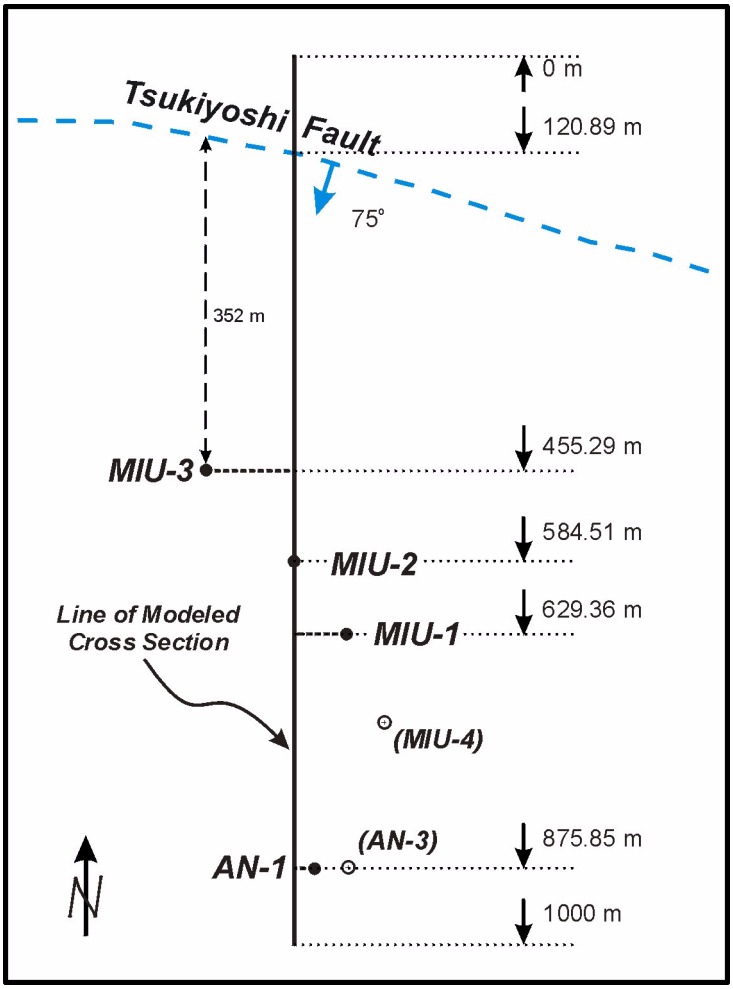

Figure 2. Geologic sketch map showing location of the modeled cross section passing through drill hole MIU-2 and the relationship of the cross section and drill holes to the Tsukiyoshi Fault. Drill holes are projected onto the plane of cross section normal to that plane at the distances shown in meters. Note that the "zero" point of the cross section corresponds to a regional *y*-coordinate value of –68,000 m North. Locations of selected drill holes *not* used in modeling shown in parentheses for reference.

2. to assess how that uncertainty changes from the pre-drilling case as information from up to four deep drill holes is added, one hole at a time, and in different sequences.

Four different drilling sequences have been defined, plus a pre-drilling "sequence," as indicated in table 2. These five specific drilling scenarios translate to a total of 11 unique modeling cases, identified in table 3 as Cases 1 through Case 10. A pre-drilling Case 0 implicitly precedes each of the numbered drilling sequences.

The cases are numbered, somewhat arbitrarily, by simple progression through the numbered sequences of table 2 and identifying combinations of drill holes not already enumerated.

Table 2: Hypothetical Drilling Sequences Used for Modeling

Drilling Sequence	Hole No. 1	Hole No. 2	Hole No. 3	Hole No. 4
Pre-Drilling	--	--	--	--
Sequence 1	MIU-3	MIU-2	MIU-1	AN-1
Sequence 2	MIU-3	AN-1	MIU-1	MIU-2
Sequence 3	MIU-3	AN-1	MIU-2	MIU-1
Sequence 4	AN-1	MIU-1	MIU-2	MIU-3

Thus, Sequence 1 includes (Case 0,) Case 1, Case 2, Case 3, and Case 4. Drilling Sequence 2 includes (Case 0,) Case 1, Case 5, Case 6, and Case 4. The other cases may be assigned to the remaining two sequences in a similar manner. These assignments are also given in table 3.

Table 3: Unique Modeling Cases Based on Drilling Sequences

Case ID	Sequence(s)	Hole No. 1	Hole No. 2	Hole No. 3	Hole No 4
Case 0	Pre-Drilling	--	--	--	--
Case 1	1, 2, 3	MIU-3	--	--	--
Case 2	1	MIU-3	MIU-2	--	--
Case 3	1	MIU-3	MIU-2	MIU-1	--
Case 4	1, 2, 3, 4	MIU-3	MIU-2	MIU-1	AN-1
Case5	2, 3	MIU-3	AN-1	--	--
Case 6	2	MIU-3	AN-1	MIU-1	--
Case 7	3	MIU-3	AN-1	MIU-2	--
Case 8	4	AN-1	--	--	--
Case 9	4	AN-1	MIU-1	--	--
Case 10	4	AN-1	MIU1	MIU-2	--

For various reasons that will be explained in greater detail in later sections of this report, a few alternate modeling cases (identified by a letter appended to the case number) were also defined; these cases are listed in table 4. Case 0a was defined to account for the fact that the baseline fracture-frequency prior identified from outcrop data for Case 0 seems anomalously high in light of "later" drilling information. This discrepancy is discussed at length in the section on *Pre-Drilling Fracture Frequency Information from Outcrop*, beginning on page 35. Case 10a is actually a better representation of Case 10 than Case 10 itself, in that the Tsukiyoshi Fault is represented stochastically and subject to the constraints on the fault dip that would actually have been available, had Drilling Sequence 4 been implemented in the field. These constraints are discussed in the section on *Information Regarding the Tsukiyoshi Fault* (page 46). However, at the time the models were being generated in production mode, it seemed simpler and faster to neglect the very slight uncertainty in the subsurface location of the Tsukiyoshi Fault allowed by Case 10a, and Case 10 with a deterministic (single-valued dip) fault was generated as a first-pass set of simulations. Case 8a is an experimental effort to investigate the influence of differing fracture frequencies in the hanging wall and footwall structural blocks.

Table 4: Alternate Modeling Cases
[Drill hole data content is identical to baseline cases in table 3]

Case ID	Difference from Baseline Case
Case 0a	Lower prior-expectation fracture-frequency value of 2.23 m^{-1} compared to baseline Case 0 value of 8.41 m^{-1}. The lower value is more consistent with subsurface frequencies observed in boreholes.
Case 10a	Stochastic fault dip, tightly constrained, as described in text.
Case 8a	Use of different prior frequency expectations for the hanging wall and footwall blocks

Model Domain

The modeling domain has been defined as a two-dimensional vertical cross section 1-km long by 2-km deep, and the plan view of this cross section in relationship to the various data available for projection onto the section has been presented in figure 2. Additional discussion of the geometry of the subsurface, including both the Tsukiyoshi Fault and the various boreholes will be presented under the heading of *Data*, beginning on page 35, below.

The top of the model domain is defined as the highest known topographic elevation at +232 m, and the bottom of the model is 2000 m below that elevation at –1768 m. The distance dimension of the model was determined arbitrarily (but conveniently) simply by truncating the first two digits of the drill hole northing coordinates (–68xxx.x) and converting the remaining digits to positive numbers. This truncation and sign-conversion process produces coordinate values for the various drill holes and for the Tsukiyoshi Fault that fall at appropriate positions within the range of zero to 1000 m, and which plot as though the north-south cross section were being viewed from the west. The process also amounts to projecting the several drill holes onto the plane of the cross section simply at right angles to the section profile, as illustrated in figure 2.

The model domain has been discretized for geostatistical modeling purposes using a 4-m by 4-m spacing of grid nodes. There are 250 grid blocks in the horizontal dimension (250 x 4 m = 1000 m) and 500 grid blocks in the vertical dimension (500 x 4 m = 2000 m). As will be described in greater detail under the *Data* section, on page 35, below, the available drill hole measurements of fracture frequency are averaged over 4-m vertical increments, and thus the scale of the input data values and the scale of the modeling units (“volumes”) are identical.

Because the surface elevations of the several drill holes appear to decrease from north to south, a few of the grid blocks near the southern end of the cross-sectional domain actually are above ground level. A maximum of three (3) grid blocks (vertically) are so affected at the location of drill hole AN-1, representing a vertical distance of 3 x 4 m = 12 m. Compared to the total vertical extent of the model at 2,000 meters, this physically “unreal” region is trivial, and no explicit correction for this non-physical space has been attempted.

Because the emphasis of the modeling exercise is on uncertainty and changes in uncertainty with successive additions of information, we have adopted the geostatistical construct of ***conditional simulation***[1] as our fundamental modeling algorithm. Conditional simulation is a probabilistic technique that can produce an arbitrary number of equally likely stochastic realizations of a particular measured property within the model domain. These alternative realizations exhibit a number of important properties, in addition to being equally likely. Each simulation:

- reproduces the observed data values at the spatial location of those data values;
- reproduces the univariate statistical nature of the input values: specifically the histogram; and
- reproduces the observed spatial correlation structure of the input values: specifically the variogram.

A consequence of these three attributes of geostatistical simulation is that the different simulations are essentially indistinguishable from one another based on objective statistical measures. Because the various realizations constituting a suite of simulations are thus both equally probable and statistically indistinguishable, variations among members of such a suite of replicate models should provide a rigorously quantitative measure of ***uncertainty*** related to the absence of "complete" or exhaustive knowledge.

For the sake of simplicity, we have further adopted the specific geostatistical algorithm of conditional Gaussian simulation, in which the internal computations make use of the bivariate (x and y) normal spatial distribution under the assumption that the conditional probabilities (of fracture frequency, in this case) are completely described by the ***conditional expectation*** and ***variance*** obtained through the ***kriging*** process. (Isaaks and Srivastava, 1989; Goovaerts, 1997; Deutsch and Journel, 1998). Kriging essentially is an estimation process involving computing a weighted average of nearby data values where the weights are determined in a "geologically based" manner using the original data values themselves.

An alternative modeling approach for assessing the desired information regarding uncertainty would have been to use ***indicator simulation***, which entails discretizing the distribution of fracture frequency values into a number of different frequency classes, modeling the spatial structure (***variogram***) of each class of indicators separately, and then simulating these classes in a sequential manner. Indicator simulation is therefore a much more labor and computationally intensive procedure. Kriging is again the mechanism underlying the simulation process.

1. Throughout this report, the first use of certain terms specific to geostatistics or that otherwise may be considered "jargon" are ***italicized***. We list these terms and provide a definition or expanded discussion of these terms, *in the context in which they are used for this report*, in the *Glossary* at the end of this report (beginning on page 117).

The Sequential Gaussian Simulation Algorithm

The ***sequential Gaussian simulation*** algorithm, as implemented in the GSLIB software routine, SGSIM (Deutsch and Journel, 1998), may be described in relatively straightforward manner as follows:

1. The available sample data are converted to normal-score values. The resulting distribution of values is Gaussian in form and has a mean of zero and a variance of one.

2. The ***experimental variogram*** of the normal-score-transformed data is calculated and a ***variogram model*** defining the spatial continuity structure is fitted to this variogram (here in two dimensions only).

3. The normal-score transformed data are mapped onto a regularly spaced modeling grid (here 4-m x 4-m) covering the cross-sectional domain, and these conditioned nodes are flagged so that the data values remain unchanged throughout the simulation process.

4. A random path through all unsampled grid nodes is generated for the sequential simulation process that follows. Note: the "seed" value for this random number determines not only the random path along which all unconditioned grid nodes are visited, but also the generation of the random numbers required in step 8 below.

5. At the first grid node along the path, a search is conducted for any "nearby" conditioning data (and after the initial point, for any previously simulated values). The specific definition of *nearby* is set by the user, but generally the procedure is to take the nearest 10–12 data or grid-node values up to approximately the range of spatial correlation.

6. The set of nearby data and previously simulated values is weighted by their geostatistical proximity to the node being simulated according to the model of spatial continuity structure (the model of the variogram) developed in step 2, above. This is the kriging process introduced above.

7. Under the assumption of a multivariate Gaussian spatial distribution, the weighted-average value computed in step 6 and the kriging variance define the mean and variance of the Gaussian conditional probability distribution of fracture frequency at this location.

8. A value is selected at random from this probability distribution so defined, and assigned as the (normal-score-transformed) fracture frequency value at that location.

9. The simulation process moves to the next grid node along the random path defined in step 4 and the generation process begins again as described in step 5. The simulation process is complete when all grid nodes within the model domain have been processed.

10. Following completion of the simulation, the normal score simulated values are back-transformed to "real" (fracture-frequency) space using the histogram of the frequency distribution.

Additional simulations are generated by restarting the process at step 4 using a different (uniformly distributed) random number seed value. For this study, we have generated suites of 100 replicate simulations for each modeling case.

Accounting for Prior Information Regarding Fracture Frequency

There are at least two types of ***prior information*** to be incorporated into the modeling process: information related to the fault plane and additional information regarding geologic controls on fracture frequency in the subsurface obtained as drilling proceeds. The fault may be assumed, a priori, to be associated with greater fracture frequencies, even though the specific frequencies — and, indeed, even the exact location of the fault at depth — may be uncertain. Additionally, the known geology of the site (Goto, personal communication, 2000), consisting of plutonic rocks overlain nonconformably by sediments, suggests that there may be a fundamental subhorizontal layering of fracture frequency, at least as related to the extent of sedimentary rocks at depth. As will be described below, this inference of a fundamental layering of fracture frequency has influenced our "early" selection of ***anisotropy ratios*** between the range of spatial correlation (variogram) in the horizontal dimension, in contrast to the range of correlation in the vertical direction. Note that the actual geology, and true ranges of spatial correlation, can be determined explicitly only through drilling. Thus, our ***prior estimate*** of fracture frequency may change not only in space, but also in "time" as the various hypothetical drilling sequences proceed.

Generation of the numerical fields (cross-sectional profiles) of prior expectations for fracture frequency is described below in the section entitled *Analysis and Modeling*, beginning on page 35. Conceptually, however, the process is relatively simple and intuitive.

Recall that the conditioning data were converted to their normal-score equivalent values in step 1 of the sequential simulation process (page 23). The resulting distribution is $N(0,1)$: mean zero and with variance equal to one. Step 7 of the simulation process involved computing the weighted average of the nearby data and previously simulated values; specifically the computation is what is termed ***simple kriging***. The simple kriging formula is generally given (Deutsch and Journel, 1992, eq. IV.1) as:

$$[Z^{*}_{SK}(\boldsymbol{u}) - m(\boldsymbol{u})] = \sum_{\alpha=1}^{n} \lambda_{\alpha}(\boldsymbol{u})[Z(\boldsymbol{u}_{\alpha}) - m(\boldsymbol{u}_{\alpha})], \quad (1)$$

where $Z^{*}_{SK}(\boldsymbol{u})$ is the simple kriging estimate at spatial location $\boldsymbol{u}$, the $Z(\boldsymbol{u}_{\alpha})$ are the n measured data at locations $\boldsymbol{u}_{\alpha}$ located close to $\boldsymbol{u}$, and the λ_{α} are the weights for location $\boldsymbol{u}_{\alpha}$ computed from the ***spatial covariance*** matrix based on the spatial continuity (***variogram***) model. The critical quantity is m, which is the mean of the distribution. Note that m is stated to be a function of spatial position, $\boldsymbol{u}$.

Effectively what equation (1) says is that we are estimating the ***residuals*** from some (potentially) spatially varying mean value, m. Mathematically, the mean value(s) are subtracted from the data values prior to computing the weighted average, and then is added back to that average to yield the final estimated value, $Z^*_{SK}(\boldsymbol{u})$.

In the more typical implementation of simple kriging as applied to sequential Gaussian simulation (step 7, above), the mean value of the distribution is constant and equal to zero, as the data have been transformed to be $N(0,1)$. The impact of m in this case is thus trivial. However, if we have ***prior*** evidence that m is not constant, and instead is a function of spatial location, we can provide an array of those locally varying mean values, $m(\boldsymbol{u})$ *at every grid node* and incorporate these "soft" data (in contrast to "hard," measured values) directly into our estimate of the conditional probability distribution used in step 8 to generate the simulated value. Note also that the locally varying mean values may be different for different realizations, thus allowing for incorporation of uncertainty in our prior estimates of what the fracture frequencies may be as well.

Spatial Correlation Analysis (Variography)

Spatial correlation analyses have been conducted for the composite data sets from each case shown in table 3 using standard variography techniques. The variogram (formally, the semivariogram, γ) is computed as one-half the average squared difference in fracture-frequency value, Z, between all pairs of points, $x_{(i)}$ and $x_{(i+h)}$, which are separated by a vector distance, h. Thus:

$$\gamma(h) = \frac{1}{2N(h)} \sum_{i=1}^{N(h)} [Z_{(x_i)} - Z_{(x_i+h)}]^2, \qquad (2)$$

where $N(h)$ is the number of available pairs that are separated by the particular vector-separation ("lag") distance. Note that there are two vector directions that are of interest in the current exercise: vertical (up and down the same drill hole) and horizontal (between drill holes). Note also that there will be a large number of separation distances (magnitude of h) that can be computed for the vertical direction, whereas there will be only a few separation distances that can be computed for the horizontal spacing of a mere four drill holes, maximum.

The variogram value, $\gamma(h)$, is then plotted for all the available separation vectors, h, and this plot is termed the ***experimental*** (or data) ***variogram***. It describes the observed variability [note the resemblance of the squared-difference term of equation (2) to the formula for a variance] of the fracture frequency pairs as a function of the distance between members of those pairs. Because the geostatistical modeling process requires that this variability, formally the ***spatial covariance***, be known for all possible separation distances and orientations during modeling, it is necessary to fit a ***variogram model*** to the experimentally determined data points. Because the mathematical form of the model selected must yield a positive-definite covariance matrix within the geostatistical modeling algorithms, it is typical to select the variogram model from a relatively limited, but nevertheless flexible, set of models that are known to yield these positive-definite covariance matrices. Additional flexibility with respect to fitting the experimental variogram may be had by ***nesting***, or combining different types of models to best approximate the experimental data. Figure 3 presents some common variogram model types, and also demonstrates the nesting,

or addition, of two individual models to produce a final model to be used in downstream modeling. Some common nomenclature used to describe various features of variogram models, the ***nugget*** (C_0), ***sill*** (C), and ***range*** (a), are also indicated in Figure 3(d). These quantities constitute the ***variogram parameters*** that enter into the mathematical computation of the spatial covariance matrix.

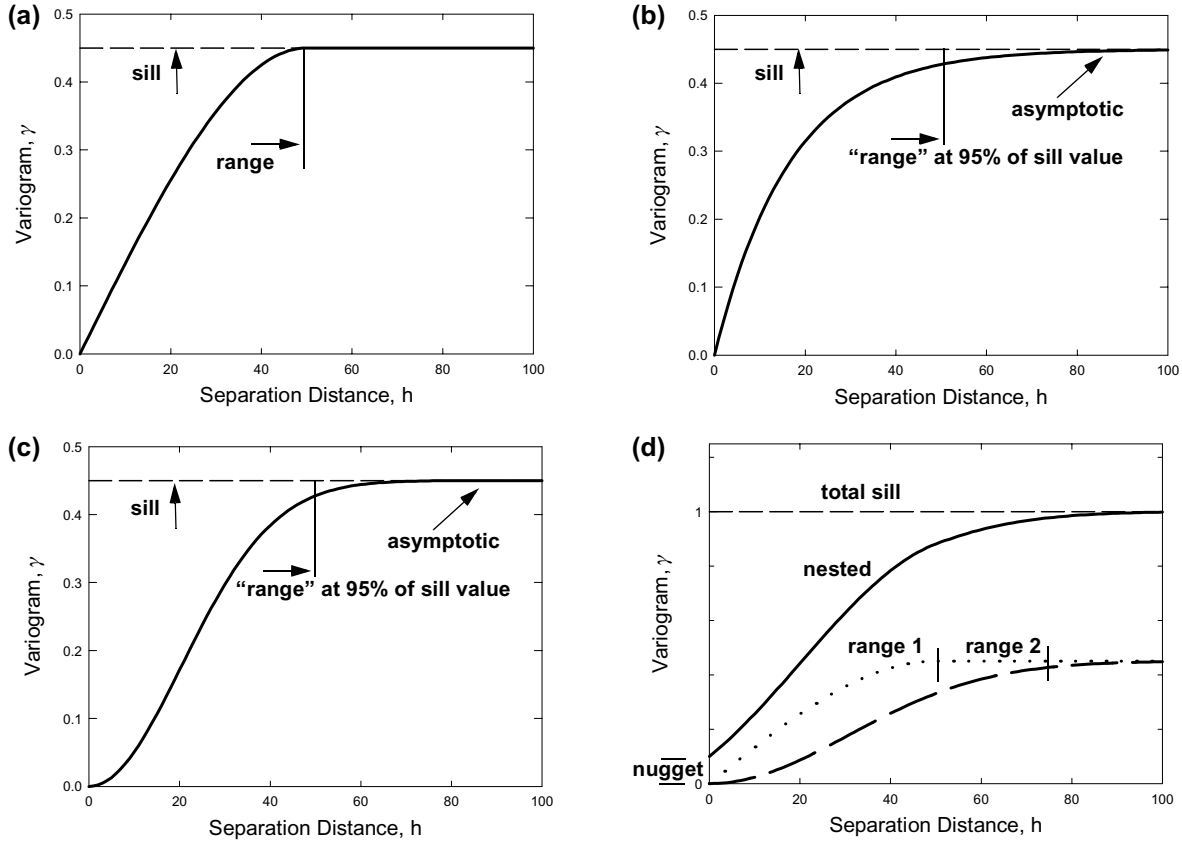

Figure 3. Plots showing (a) a spherical variogram model; (b) an exponential variogram model; and (c) a Gaussian variogram model. Part (d) illustrates the combination (addition) of a spherical and a gaussian model, together with a nugget-effect value, to yield a final, nested model. Terminology used to describe variogram models is also indicated.

Summarizing Large Suites of Replicate Simulations

Simulation as a modeling technique is well known for producing prodigious quantities of output that must be evaluated in some manner. Geostatistical simulation is no exception to this rule. In fact, we have generated 100 replicate realizations of each of the 14 cases identified in tables 3 and 4, each realization containing 125,000 grid nodes. It is thus important to be able to summarize and evaluate these many replicate models of fracture frequency in some efficient manner. In this modeling exercise, we are interested most specifically in evaluating uncertainty in our understanding of fracture frequency in the subsurface and in how the uncertainty in our under-

standing changes as a function of our adding "information" to the models, as obtained from differing combinations of drill holes.

It is convenient to break the summary of large suites of replicate simulations in geostatistical modeling into (at least) two portions. One part may best be conceptualized as evaluating the "average" or ***expected*** behavior of the system across the entire suite of realizations (see *Computation of "Expected-Type" Behavior Measures*, immediately following). Although each individual simulation should exhibit the three desirable attributes described by the bulleted items on page 22 under *Conceptual Modeling Framework*, it may be useful to examine patterns or features that are somewhat "common" across all the members of a suite of simulations. The second part of evaluating a large suite of replicate simulations is, in fact, that of evaluating the variability/uncertainty, or differences among the members of such a set of realizations. This, specifically, is the question we investigate in this report. The global measures of uncertainty/variability used in this report are described in an immediately following section entitled, *Computation of Global Uncertainty Measures*.

Note that a third part of an evaluation of a large suite of geostatistical simulations, and one which we do not address in this document, is the *propagation of the uncertainty* in a geostatistically simulated property of some type (fracture frequency, hydraulic conductivity, porosity, mechanical strength, etc.) *through a subsequent numerical model of some relevant physical process to describe uncertainty in some appropriate performance measure* of that physical system. An example specifically relevant to this modeling would be the use of a model of fracture frequency to predict bulk-rock hydraulic conductivity for a numerical flow-and-transport model. In such an instance, which is far beyond the scope of this modeling exercise, it is important to be aware that the behavior of the physical system in a downstream numerical model (as in reality), may be very dependent upon the complexity of the spatial distribution of the geostatistically modeled parameter (here, fracture frequency). Additionally, the physical/numerical behavior of the "expected parameter field" may be very much different than the "expected" or "average" physical behavior of the individual parameter fields processed one at a time.

If the purpose of this modeling exercise were not restricted simply to the stated objectives of describing and quantifying uncertainty in the fracture frequency generally, this loss of the low-fracture-frequency core (e.g., Caine and others, 1996; see also our figure 18 and associated discussion in the text, beginning on page 51) from the E-type summary-type model (see definition in the *Glossary*) could be more significant.

Consider the case of flow-and-transport modeling. In such a situation, the presence or absence of a *continuous* low-frequency zone throughout the vertical extent of a modeling domain could have very significant flow-related implications. Use of an expected-value-type model, such as generated for Case 10a, in which the low-frequency zone is obscured [figure 4(c)] by the averaging of replicate, equally probable simulations, might yield very different final results than the same flow-and-transport model computed on individual simulations of the underlying suite, because each individual realization will contain a continuous low-frequency zone along the full-length of the fault (even though the spatial position of that zone will vary slightly from realization to realization [figure 4, parts (a)–(c)]. The differences in the final flow field would not reflect so

much the slight differences in spatial position of the low-fracture-frequency zone as the complete disappearance of that zone locally in an averaged, E-type model [figure 4(c)].

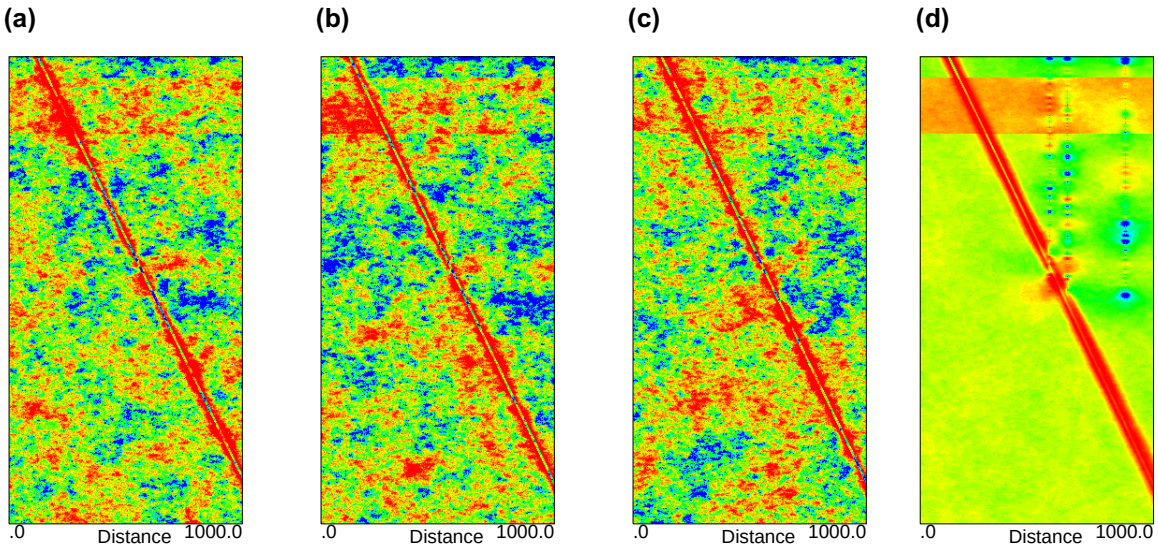

Figure 4. (a), (b), (c) Individual simulations (no. 22, 53, and 85, respectively) of fracture frequency from Case 10a, compared to (d) E-type summary model [repeated from figure 36(c)]. Note presence of a discrete, low-fracture-intensity "core" to the fault in the individual simulations and the obscuring of this core in the E-type model.

Computation of "Expected-Type" Behavior Measures

A very common and simple measure of that allows evaluation of overall "expected-type" behavior, or of the degree of "commonality" among a large number of replicate simulations is the so-called ***E-type*** (expected-value-type) ***model*** defined by Deutsch and Journel (1998). The E-type model is nothing more than the grid-node-by-grid-node average value of the simulated parameter computed across however many simulations have been generated. This quantity may be expressed mathematically as:

$$E\{Z_{\boldsymbol{u}}\} = \frac{1}{Nsim} \sum_{i=1}^{Nsim} Z_{\boldsymbol{u}_i}, \tag{3}$$

where $E\{Z_{\boldsymbol{u}}\}$ is the expected value of variable Z at a particular spatial location $\boldsymbol{u}$ within the model domain, and the $Z_{\boldsymbol{u}_i}$ are the $Nsim$ simulated values of variable Z at that same spatial location, $\boldsymbol{u}$. Because $E\{Z_{\boldsymbol{u}}\}$ is a still a function of spatial position, $\boldsymbol{u}$, it is a simple matter to display $E\{Z_{\boldsymbol{u}}\}$ graphically, just as one would display the simulated values for a single realization graphically. In this report, we display the E-type models as two-dimensional cross-sectional profiles. Note that because $E\{Z_{\boldsymbol{u}}\}$ is computed as a simple average over $Nsim$ realizations, the E-type model will reflect the attributes of this measure of "central tendency" of a distribution of simulated values for each grid node.

Another quantity that is useful in evaluating a large suite of individual, replicate simulations is the ***conditional variance***. In a manner analogous to computation of the spatially distributed expected value (E-type model), we can replace computation of the node-by-node "average" value across all realizations with computation of the variance. Thus:

$$Var\{Z_{\boldsymbol{u}}\} = \frac{1}{Nsim} \sum_{i=1}^{Nsim} (Z_{\boldsymbol{u}_i} - \bar{Z}_u)^2, \tag{4}$$

where $Var\{Z_{\boldsymbol{u}}\}$ is the conditional variance as a function of spatial position $\boldsymbol{u}$, the $Z_{\boldsymbol{u}_i}$ are the *Nsim* simulated values at that location, $\boldsymbol{u}$, and $\overline{Z}_{\boldsymbol{u}}$ is the average simulated value or $E\{Z_{\boldsymbol{u}}\}$. In practice, one of the computational formulae[1] for the variance is typically used, which allows computation of both the mean and the variance from the sums and sums-of-squares of the variable in one computational pass:

$$Var\{x\} = \frac{\sum x^2 - (\sum x)^2 / n}{n-1}, \tag{5}$$

where x is the variable of interest and n is the number of values. Because it is somewhat more intuitively interpreted, the conditional variance, $Var\{Z_{\boldsymbol{u}}\}$, is easily converted to the ***conditional standard deviation*** simply by taking the square root of the former quantity.

Note that there may be certain instances at grid nodes for which computation of the variance or the standard deviation may not be possible (or meaningful). Although the variance/standard deviation exists theoretically for any finite set of data larger than two values, the precision inherent in floating-point arithmetic in any particular computer implementation may not allow computation of a positive variance in certain low-variability situations. Such floating-point limitations are trapped in the post-processing step of simulation-related modeling routines, and any such grid nodes are "flagged" with a missing value code. We maintain a count of these missing values and examine the total count for evidence that our overall results might be numerically

1. After the modeling activities for this study were completed and Sandia was in the process of preparing this report, we becaue aware (C.V. Deutsch, personal communication, 2001) of the fact that the GSLIB post-processing software routine POSTSIM (Deutsch and Journel, 1998) actually uses a computational formula inside the compiled code that is equivalent to the typical definition of the variance of a *population*. In contrast, for reasons of convenience that are too involved to discuss here, we used a separate, custom-written program to perform the post-processing on *some* (but not all) of the simulations for this study. Within this in-house software code, known as program ETYPE, we have used the computational formula for the more traditional, and theoretically unbiased estimator of a *sample* variance. This is the formula presented in equation (5). The equivalent formula for a population variance lacks the (n-1) quantity in the denominator. In fact, the difference in resulting value of the conditional standard deviation, which is the ultimate quantity that we use for interpretations in this report, which results from a computation involving n = 100 or (n-1) = 99, can be demonstrated to be effectively trivial, and arithmetically is equivalent to approximately one-half of one percent (0.00504). Therefore, we have not bothered to re-run the various post-processing steps and our opinion is that the conclusions drawn from examining the conditional standard deviations across the various modeling cases are unaffected by this unfortunate mathematical difference. For the record, the modeling cases using stochastic fault-prior models were processed using the in-house software, whereas the cases using a deterministic fault-prior model were processed using the GSLIB algorithm.

biased as a result. This potential effect is discussed in the *Modeling Results* section of the report, but essentially our conclusion is that the number of grid nodes so affected (out of 125,000 nodes in the model domain) is so small that there is no such bias.

Computation of Global Uncertainty Measures

In the *Modeling Results* section below, we present comparisons of the various cases involved in each drilling sequence, based on the E-type models and models showing the conditional standard deviations. These comparisons are visual, and the graphical changes associated with the sequential additions of drill-hole-based information are quite revealing. However, it would also be helpful to have some type of global measure of the uncertainty associated with each of the modeling cases and with each drilling sequence. We have therefore defined two basic global-summary uncertainty measures, one based on the concept of the coefficient of variation and another based on the standard deviation.

Computation of the global average conditional standard deviation is entirely straightforward. The intent is to estimate on a global basis a measure of the average variability of the underlying realizations. The formula for the average standard deviation, $\overline{SD}$, is as follows:

$$\overline{SD} = \frac{1}{nx \cdot nz} \sum_{\alpha = 1}^{nx \cdot nz} s(\boldsymbol{u}_\alpha), \tag{6}$$

where $s(\mathbf{u}_\alpha)$ is the conditional standard deviation value for the suite of 100 replicate simulations at location $\mathbf{u}_\alpha$ [i.e., the square root of equation (5)], and the summation is over the model domain which measures *nx* by *nz* grid nodes.

The ***coefficient of variation***, in general, is defined simply as the standard deviation of a set of data divided by the mean. In the present case, we have a set of spatially variable means and conditional standard deviations that have been computed as part of the process of summarizing the suite of simulated realizations for each modeling case. Thus, it is a relatively straightforward to convert the mean and standard deviation for each grid node to a coefficient of variation, representing the variability of the suite of simulations at that spatial position, and to iterate across all grid nodes in the domain to compute a global average coefficient of variation, $\overline{CV}$. Thus:

$$\overline{CV} = \frac{1}{nx \cdot nz} \sum_{\alpha = 1}^{nx \cdot nz} s(\boldsymbol{u}_\alpha) / \bar{X}(\boldsymbol{u}_\alpha), \tag{7}$$

where $\overline{X}(\mathbf{u}_\alpha)$ is the E-type mean value for each suite of 100 replicate simulations at location $\mathbf{u}_\alpha$, $s(\mathbf{u}_\alpha)$ is the corresponding conditional standard deviation value, and the summation is over the model domain which measures *nx* by *nz* grid nodes. Of course, if the E-type value, $\overline{X}(\mathbf{u}_\alpha)$, at a particular grid location is zero fractures per meter, the concept of a coefficient of variation becomes meaningless, and the computation for that grid node is omitted. A similar action is taken if the conditional standard deviation does not exist (flagged as a missing value). These types of omissions of values at some grid nodes suggests that it might be possible to markedly overestimate the

actual global variability being computed. We have maintained a count of the number of such grid nodes for which the computation described by equation (7) was not possible and this number of omitted computations is displayed on some figures in the *Modeling Results* section. In general, the number of such omitted nodes is miniscule in comparison to the full-field count of 125,000 grid nodes, and we conclude that the numerical values of the global uncertainty measures are not compromised.

In addition to computing the global average conditional standard deviation ($\overline{SD}$) and global average coefficient of variation ($\overline{CV}$), we have computed a normalized version of these values for each drilling sequence identified in table 2. The normalization factor is the average value of each quantity for the four modeling cases of that sequence involving drill hole data. The effect of the normalization step is to compensate for the difference in magnitude of the two types of uncertainty measures and to allow comparison of both measures on a common scale.

The normalization process also allows a closer examination of the smaller changes in uncertainty that are associated with the modeling cases involving differing numbers of drill hole control data. In general, one might expect, a priori, to find a progressive decrease in the global uncertainty measures as one adds first a second drill hole, then a third, and finally a fourth borehole. Standardizing the uncertainty measures by the magnitude of the average drilling-constrained uncertainty allows more subtle variations in global uncertainty to be highlighted. For all the global uncertainty measures computed, the implication is that a larger value translates into more overall variability (without respect for spatial position) across the suite of 100 replicate simulations. Larger variability is equated (empirically, by assumption) with greater overall uncertainty of fracture-frequency distribution in the subsurface.

Methodological Summary and Process-Flow Diagram

The modeling activities documented in this report are complex and involve a number of different activities. We present a summary, overview process- and logic-flow diagram in figure 5, and describe each component briefly in the following paragraphs. The activities included in each paragraph are outlined (boxed) on the figure using a long-dashed line.

Pre-modeling Determinations

Definition of the four drilling sequences (upper left corner of figure 5) to be investigated precedes all modeling efforts. This definition is external to Sandia's modeling activities, and was provided directly by JNC. However, once the number of postulated drilling sequences is determined, the individual sequences of successive drill holes imply a number of unique modeling cases. These cases were determined in advance of any data examination or modeling activities. A limited number of "special" modeling cases were defined later in the modeling process, and these were generally intended to compensate for perceived weaknesses in certain of the baseline cases or to explore other aspects of the site geology as the modeling process proceeded. Even though definition of these special modeling cases "evolved" during the course of the ongoing work, they are included here under *Pre-modeling Determinations*.

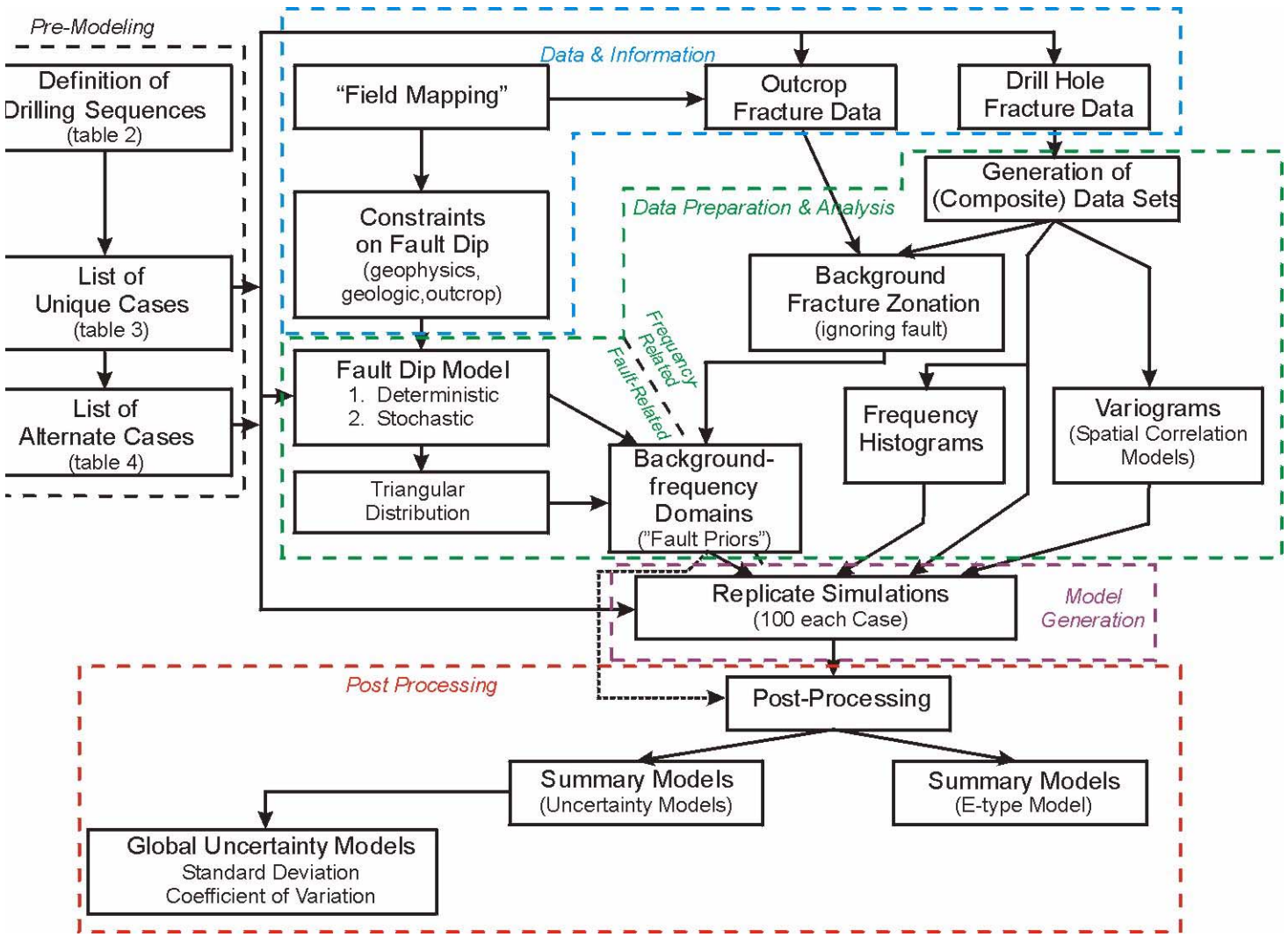

Figure 5. Summary process-flow diagram of the data-analysis and modeling activities conducted as part of this investigation of fracture frequency and the impacts of sequentially adding geologic information on the uncertainty in the modeled fracture frequency distributions. General data and processing flow is indicated by the solid lines. The short-dashed line indicates that the fault-prior models may be summarized by post processing also. The boxes outline by long-dashed lines separate the various groups of modeling activities described in the text.

Data and Other Information

A substantial quantity of data and other relevant geologic information was provided by JNC to Sandia for use in modeling. This information is represented at the top and in the left-center portion of figure 5. Measurements of actual fracture frequencies in outcrop and in the several boreholes are the principal data values provided. However, field activities also provided other types of information that constrained the major geologic feature of the MIU-site area: the Tsukiyoshi Fault. Most of this latter information went into determining the specific dip of the Tsukiyoshi Fault in any particular model of fracture frequency.

Data Preparation and Analysis

A great deal of manipulation of individual data values, groups of data, and analysis of information (broadly defined) is involved in the current study. These activities are indicated in much of the center portion of figure 5. Some of this manipulation is quite quantitative in nature, whereas some is fairly subjective.

Fault Related Preparation — Analysis and preparatory activities related to the Tsukiyoshi Fault itself comprised identification of whether a particular modeling scenario (a "case," in our terminology) was deterministic or stochastic with respect to the dip of the fault. If a drill hole contained within a particular modeling case provided a definitive location for the Tsukiyoshi Fault, the modeling was deterministic and the dip of the fault was held constant across the various modeling runs of that case. If the fault was not located definitively by the boreholes included in the particular modeling case, the dip of the fault was selected stochastically from a triangular distribution, the parameters of which were defined as closely as possible based on "then-existing" knowledge.

Fracture-Frequency-Related Preparation — Analysis and preparatory activities related to fracture frequency involved several aspects, but the principal outputs of this work are:

1. A spatially distributed "background" fracture frequency onto which both "fault-related" fracturing and location-specific drill-hole fracturing information would be superimposed.

2. A data set (potentially a composite set) representing the conditioning data used to constrain the simulated models and to "anchor" the models to the physical MIU site to the extent possible.

3. A fracture-frequency histogram representing the available frequency data that forms the target histogram for each simulated model. The histogram may be derived directly from conditioning data (where such exists) or inferred indirectly based on pre-drilling outcrop observations only.

4. A model (in two dimensions only) of spatial correlation or spatial continuity of fracture frequency. This is the variogram model. Again, the variogram model used for a

given simulation sequence may be derived directly from conditioning data or inferred indirectly from other information and assumptions.

Generation of Fault-Prior Models — The final step of data preparation is the combining of the fracture-frequency information and the fault-related information into what we term a "fault-prior model." In effect, this step involves superimposing the influence of the Tsukiyoshi Fault onto the background fracture frequency, based on whatever information exists given the "current" state of knowledge at each step in the drilling sequences.

Model Generation

Generating the simulated models is perhaps the easiest step in the entire modeling process. This step is represented in the lower-center portion of figure 5. Geostatistical simulation, once the inputs have been analyzed and defined, is a purely mechanical process. Nevertheless, it is one which takes the prior model of fracture frequency (including the elevated frequencies presumed induced by the presence of the Tsukiyoshi Fault), the conditioning fracture-frequency data from any drilled holes, and the inferred model of spatial continuity, and generates an arbitrary-but-large number of replicate stochastic "realizations," *all of which* are compatible with the known collection of data and which vary randomly at locations other than actual data measurements in a manner *consistent with* both the data and the modeled variogram. Collectively, the variation among a suite of simulations generated for a specific modeling case empirically represents the ***uncertainty*** associated with that particular state of knowledge.

Post Processing

Examination of each member of a suite of replicate simulations poses a tedious process in which the important factors related to both expectation and uncertainty are apt to become completely lost in a sea of overwhelming detail. Accordingly, the simulations associated with each modeling case have been post-processed to yield two distinctly different types of summaries.

1. *Spatial aspects* of both uncertainty and commonality are presented as cross-sectional maps in two dimensions. The E-type model represents what is common across the replicate simulations, and the conditional standard deviation model represents a succinct summary of the variability over the suite of simulated models

2. *Global aspects* of uncertainty are summarized for each modeling case in a single value (although two different measures of global uncertainty are computed and presented). Changes in the global uncertainty measure(s) with the progressive addition of "information" via drilling are easily presented and grasped.

ANALYSIS AND MODELING

Data

Pre-Drilling Fracture Frequency Information from Outcrop

Prior to drilling any of the drill holes at the MIU site, the only information available regarding fracture frequencies in the subsurface is from outcrop studies conducted in the vicinity of the site. Fracture measurements, given as absolute counts, are available from six different locations; also available are the approximate areas of each outcrop, given in square meters. These data are listed in table 5.

Table 5: Fracture Frequency Data from Outcrop Measurements
[Raw data (first 3 columns) are counts (absolute number); other units as indicated]

Outcrop Description	Cracks	"Open" Cracks	Total Fractures (sum)	Outcrop Area (m^2)	Total Fracture Frequency (m^{-1})
By Individual Outcrop					
P-1[1]	13	43	56	49.9	3.96
P-2[1]	12	35	47	39.7	3.73
P-31[1]	39	112	151	38.6	12.15
P-4[1]	25	82	107	7.7	19.28
Garaishi River[2]	64	19	83	40.0	6.56
East Side, Garaishi River[2]	27	5	32	625.0	0.64
Overall	180	296	476	800.9	8.41[3]
By Structural Domain					
South of Fault	89	272	361	135.9	15.48[3]
North of Fault	91	24	115	665	2.23[3]

[1] south of Tsukiyoshi Fault (hanging wall)
[2] north of Tsukiyoshi Fault (footwall)
[3] area-weighted average

For consistency with general practice in fracture modeling and with the information available from the four drill holes that is discussed below, the total fracture count for each measured area has been converted to fracture frequency with units of per-meter (m^{-1}). Because this desired quantity is not the original units of measure (we have number of fractures and area, which can easily be restated as number per meter-squared, m^{-2}), some assumptions are required.

If we may assume that the fractures are oriented approximately at right angles to each other (i.e., two fracture sets at ~90-degrees) and that each set is roughly equally developed, then the number of fractures that would encountered along a linear traverse perpendicular to either set would be expected to be *N/2*, where *N* is the total number of fractures observed. Note that there is

an implicit assumption in this *N/2* estimate that the dimensions of the surveyed outcrop are somewhat equal (approximately a square). We may then divide this result by the square root of the area of the outcrop, obtaining a count per meter, which represents the desired units:

$$Frequency = \frac{N/2}{\sqrt{Area}}. \tag{8}$$

Equation (8) has been applied to the raw data in table 5, and the results are given in the final column of that table. These fracture intensities must be recognized as only an approximation of the actual fracture frequencies, had the measurement process been more custom-tailored to the modeling problem at hand.

Histograms of the outcrop fracture-frequency data, which are required for the geostatistical simulation process, are presented in figure 6. Figure 6(a) shows the measurements in two ways. First, the raw values from the last column of table 5 are shown by the wide, uncolored (outlined only) bars. Recall that there are only six outcrops that have been sampled: this is a very sparse data set. Second, the six outcrop fracture frequencies from table 5 have been weighted by the area represented by each exposure, and these weighted frequencies are shown by the narrow, filled bars. Again, there are only six actual measurements, but the area-weighted values are interpreted as likely to be more representative of the granitic mass as a whole, given that we are limited at this point to surface observations in the pre-drilling case. These weighted fracture frequencies are represented in cumulative distribution format as the heavy red line.

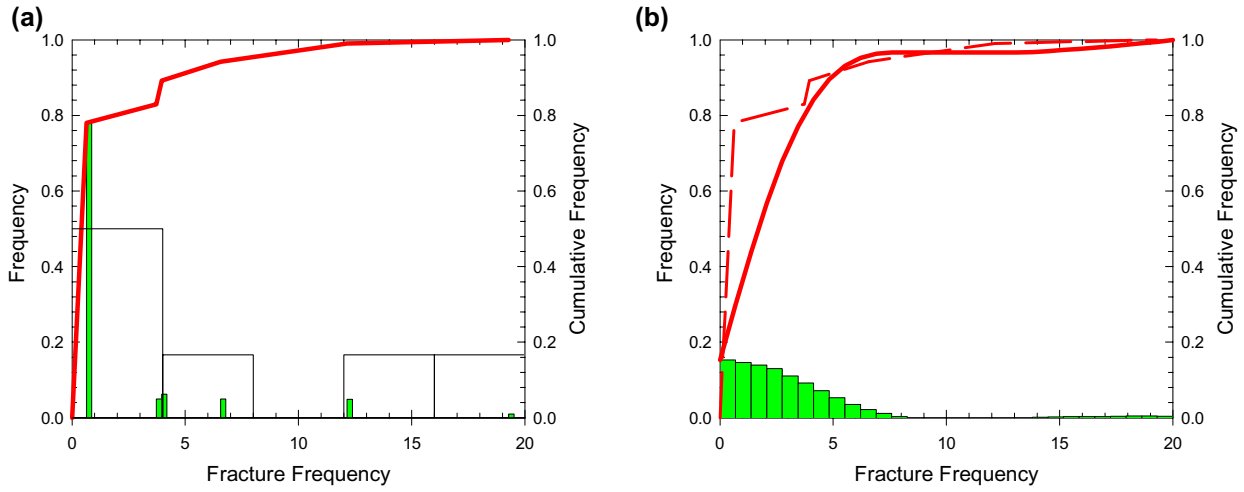

Figure 6. Histograms and cumulative distribution functions of fracture frequency measured in outcrop near the MIU site. (a) Raw data: outlined bars are as-measured; thin green bars are weighted by outcrop area. (b) Smoothed histogram used in geostatistical modeling.

Because the measured outcrop data are so sparse, we have attempted to "smooth" these values to determine a somewhat more even distribution of frequencies that have essentially the same cumulative distribution as the area-weighted fracture-frequency values. The GSLIB program, HISTSMTH (Deutsch and Journel, 1998), has been used to accomplish this smoothing. The

results are shown in part (b) of figure 6. The histogram bars and solid cumulative distribution function represent the smoothed distribution, which will be used in the back-transformation part of the simulation algorithm (step 10 on page 24). The weighted data cumulative distribution function has been reproduced for reference and comparison as the dashed curve. Although the very sparse nature of the actual measurements prohibits a more-faithful reproduction of the area-weighted CDF curve, the smoothed CDF is judged to be a reasonable, and less "discrete" representation of the small amount of information available for the pre-drilling modeling case.

Note in table 5 that there is a profound difference between the fracture frequencies observed north of and south of the Tsukiyoshi Fault, with the outcrops to the north of the fault exhibiting an average ("expected") fracture frequency of only slightly more than 2 m^{-1}, whereas the outcrops to the south of the fault exhibit average frequencies in excess of 12–15 m^{-1}. These values correspond to an implied difference of fracture frequency in the footwall and hanging wall respectively. Such geologic control on fracture frequency in different structural domains is not uncommon. However, as will be discussed at greater length below, it is not entirely obvious that this distinction with respect to fracture frequency is observable in the drill hole information. Lacking detailed geologic knowledge, it is also possible that the generally higher fracture frequencies observed in outcrop to the south of the fault are related more to surficial weathering and enhancement of incipient breaks, rather than to wholesale brittle deformation of the hanging-wall block overlying the fault.

Because there are no drill holes involved in the pre-drilling modeling scenario (tables 2, 3), the necessary prior estimates of fracture frequency throughout the entire model domain are taken directly from the outcrop data presented in table 5. Modeling Case 0 uses the overall observed fracture frequency of approximately 8.41 m^{-1} as the expectation of this prior distribution. This represents the relatively naive assumption that the best prior estimate of fracture frequency in the subsurface is simply the area-weighted average of all outcrop fracture observations, and that there is no known geologic control on fracture frequency. As will become apparent in discussing the fracture frequencies observed in the four drill holes available at the MIU site (immediately below), there is evidence that the measured outcrop fracture frequencies markedly overestimate the apparent in-situ fracture frequencies in the granites. Accordingly, an alternative modeling scenario, Case 0a, was also defined, for which the prior estimate of fracture frequency was selected as the area-weighted average fracture frequency to the north of the Tsukiyoshi Fault, approximately 2.23 m^{-1}. Note that this choice was guided by our observations of the typical fracture frequencies at depth in the various boreholes, and would *not necessarily* have been selected in a true pre-drilling situation.

Fracture Frequency Information from Drill Holes

Fracture frequency measurements for one-meter intervals are available from each of the four drill holes listed in table 1. An illustration showing the raw one-meter fracture frequency data is presented in figure 7. The data were already available as a function of actual elevation, rather than depth below ground level. The one-meter level of detail was judged to be excessive for modeling purposes, and the one-meter fracture counts (by definition in units of per meter) were converted to four-meter-average frequencies in the following manner.

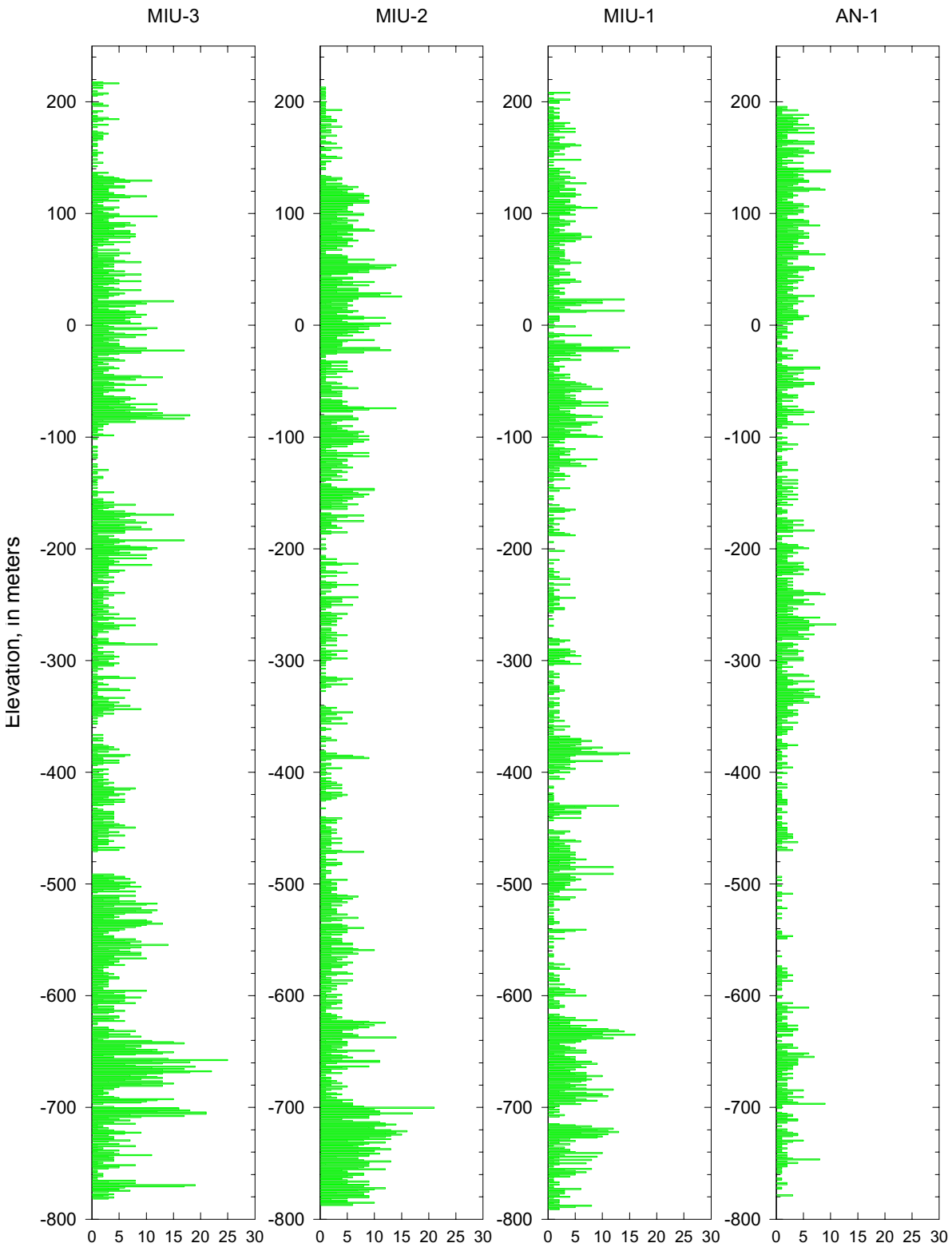

Figure 7. Drill hole plots showing the raw (as originally measured) fracture frequencies on one-meter intervals for the four drill holes available from the MIU site.

Aggregation intervals were defined with tops and bottoms that are even multiples of four meters. The top of the highest aggregation interval extended to the even 4-m increment above the elevation of the highest available measured data. The numbers of fractures counted in each one-meter interval within the relevant aggregation interval were summed, and the total divided by the number of one-meter intervals thus represented (i.e., four). A 1-m fracture frequency of zero within a 4-m aggregation interval reduces the average fracture frequency. This reduction of average frequency also applies at both the very top and very bottom of the drill hole, where, in fact, the "zeros" may represent missing input values rather than a measured absence of fractures. This limitation on the aggregation algorithm is not judged to be significant, as it can affect only the very top and bottom of a drill hole, where each drill hole is approximately 1000 meters deep (250 4-m increments). The four-meter-averaged frequencies for each of the four drill holes are presented graphically in figure 8, using a presentation format identical to that of figure 7. The averaged data values are assigned to a single depth corresponding to the midpoint of the 4-meter-averaging interval.

Following the creation of the four-meter-averaged frequency data sets for each borehole, the individual drill hole data sets (from fig. 8) were combined into composite data sets corresponding to each unique modeling case (tables 3 and 4, derived from the postulated drilling sequences of table 2). A consequence of the selection of even four-meter aggregation intervals is that the top and bottom of the composite intervals in each separate drill hole are easily aligned on elevation. For each of the various modeling cases, the composite 4-m average fracture frequencies for the relevant drill holes included in the specified case were combined simply by averaging directly "across" the included drill holes. Each composite (4-m average) value is entered into the composite data set at a common interval-mid-point elevation for display.

Following generation of the composite data sets, one for each case to be modeled, the overall vertical distribution of fracture frequencies in the composite data was plotted (figures 9, 10, and 11) and examined. These overall fracture frequencies for the composite data for a given drilling case were then used to define a ***prior estimate*** of "background" fracture distribution throughout the modeled region for that case. The prior estimates represent our best guess of the fracture distribution prior to conditioning that distribution by the measured data using geostatistical simulation, and these estimates are shown by the red lines on the composite figures. The prior estimates were generated simply by visual inspection of the composite drill hole profiles, and they are not formally defined in any particular manner, other than that we attempted to capture a subequal number of higher and lower frequency values within any one zone. Note the relatively prominent horizontal layering, especially within the upper 400–500 meters of each borehole.

For the sake of simplicity, the number of fracturing zones has been restricted to three, and that the definition of the three zones is based on largely on geology. Zone 1 extends from the top of the model (at an elevation of +232 m) to approximately the base of the sedimentary sequence overlying the granites at depth. Zone 2 is more highly fractured in general and is located entirely within the granitic rocks. It is presumed to represent a weathered interval that has had the degree of fracturing enhanced, either through unloading of in-situ stress or through weathering prior to deposition of the nonconformably overlying sedimentary sequence. Zone 3 is located below the more highly fractured granitic materials of Zone 2, and it extends to the base of the model at –1768 m (a total vertical extent of 2,000 m), even though there are no data directly bearing on the

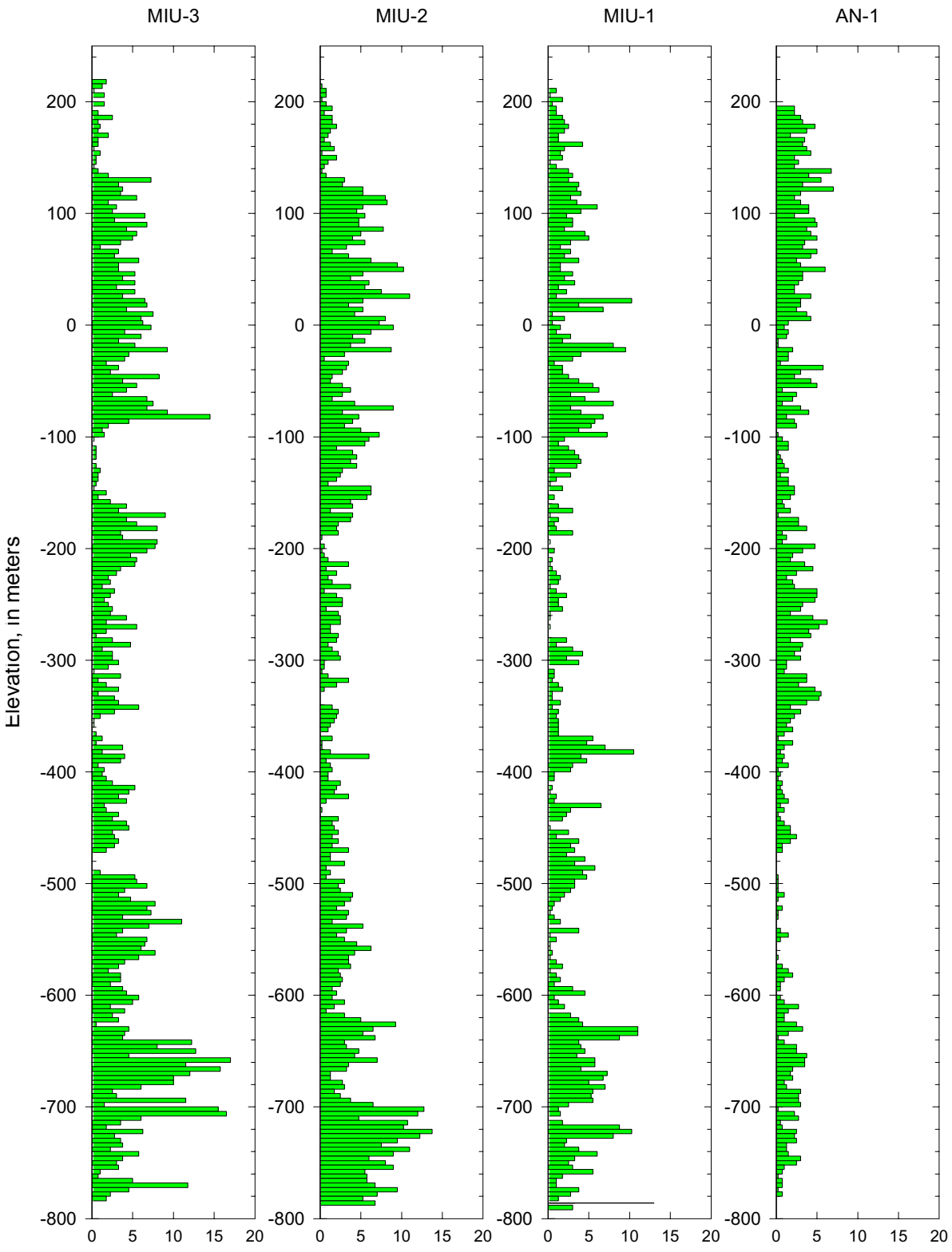

Figure 8. Drill hole plots showing the aggregated fracture frequencies on four-meter intervals for the four drill holes available from the MIU site.

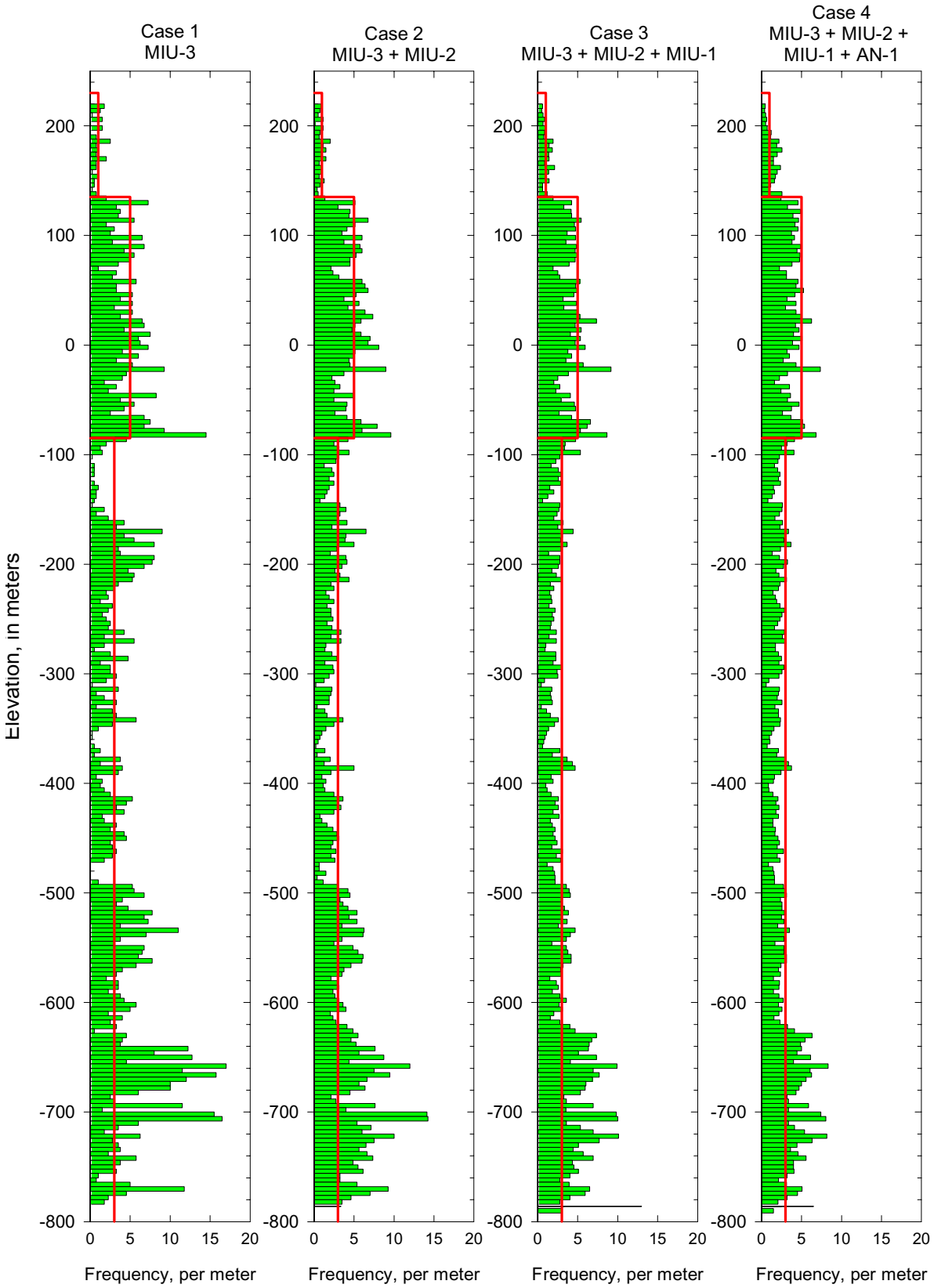

Figure 9. Drill hole plots showing the composite, prior vertical distribution of fracture frequencies on four-meter intervals for Cases 1–4. The zones of prior-fracture-frequency expected values are shown in red.

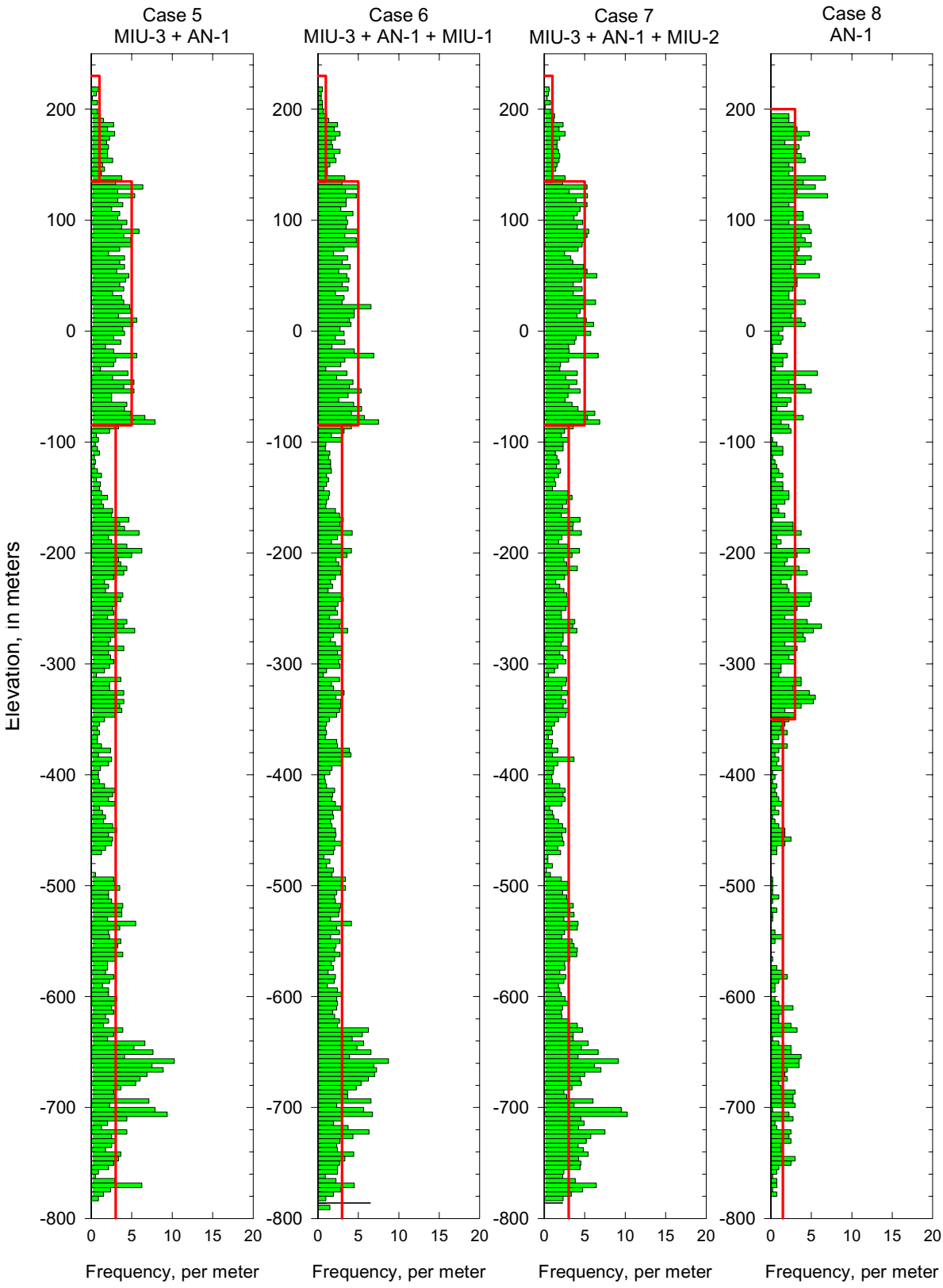

Figure 10. Drill hole plots showing the composite, prior vertical distribution of fracture frequencies on four-meter intervals for Cases 5–8. The zones of prior-fracture-frequency expected values are shown in red.

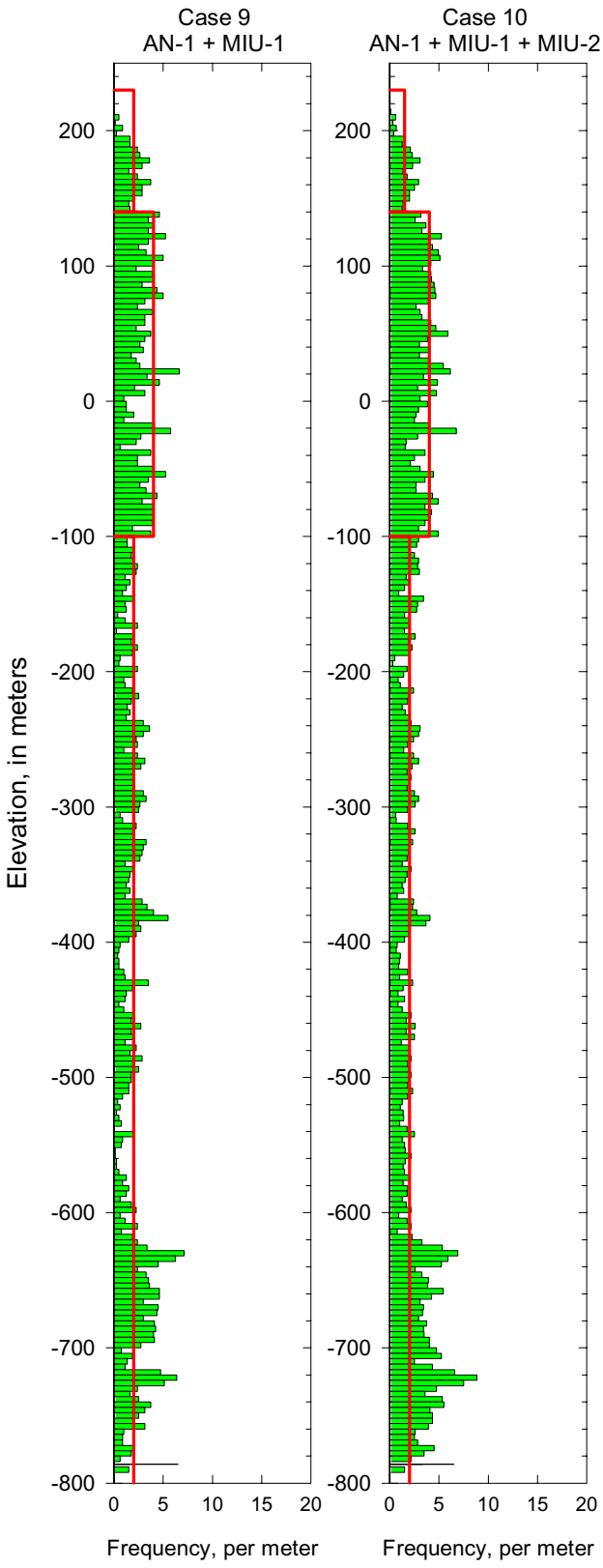

Figure 11. Drill hole plots showing the composite, prior vertical distribution of fracture frequencies on four-meter intervals for Cases 9 and 10. The zones of prior-fracture-frequency expected values are shown in re

expected fracture frequencies below the level of the 1000-ft deep boreholes. Zone 3 is less intensely fractured on the whole, and it is presumed to represent relatively unaltered and/or unweathered materials.

Note also that some intervals of apparently elevated fracturing at depth in some of the composite data sets have been neglected in assigning the prior fracture-frequency values. This is because these intervals of more intense fracturing are believed related to penetration of the Tsukiyoshi Fault in drilling cases involving drill holes MIU-3 and/or MIU-2. As fault-related, these elevated frequencies are not relevant to the prior estimate of *background* fracture frequency across the entire model domain, and are thus discounted. That this treatment is appropriate is generally confirmed by examining the fracture frequency plot for drill hole AN-1 (figure 8), which is located far to the south of the fault (figure 2), did not penetrate the fault, and presumably is unaffected by associated breakage of the rock mass.

The prior frequency estimates shown in figures 9 to 11 are also summarized by zone in tabular form in table 6. Note that the prior frequencies estimated for Cases 1 through 7 are identical. Also indicated in the final column of table 6 is the *maximum observed frequency value*, defined here as the maximum frequency *above* the background frequency of the same interval. Note in table 6 (and in figures 9–11) that in general, the vertical zonations of fracture frequency across the various cases are fairly consistent. The exception is for Case 8, which contains data from only drill hole AN-1. This borehole is located at a greater distance from the outcrop of the fault trace, and consequently does not particularly resemble the fracture profiles of the other drill holes or composite data sets. Effectively, Case 8 exhibits only two prior zones for differing fracture frequency. In fact, for drill hole AN-1, the uppermost fracture zone in the other holes is "missing" because the surface elevation of this borehole is lower than for the other three drill holes. The background frequency for zone 1 in Case 8 has therefore been set to zero. Histograms of the fracture frequencies for each composite data set without regard for vertical position are shown by case in figures 12 and 13.

Table 6: Prior Expectations of Fracture Frequency from the Combined Drill Hole Data Sets
[Fracture frequencies are 4-m averaged counts, aligned on even 4-m increments; maximum observed value is frequency *above* relevant background. The top of the model is at +232 m]

Case ID(s)	Base of Zone 1 (m)	Background Frequency (m^{-1})	Base of Zone 2 (m)	Background Frequency (m^{-1})	Base of Zone 3 (m)	Background Frequency (m^{-1})	Maximum Observed Frequency (m^{-1})
Cases 1–7	+135	1.0	– 85	5.0	–2000	3.0	14
Case 8	+200	0.0	–350	3.0	–2000	1.5	18
Case 9	+140	2.0	–100	4.0	–2000	2.0	18
Case 10	+140	1.5	–100	4.0	–2000	2.0	15

We have previously remarked upon the differences in the average or expected fracture frequencies observed in outcrop (see discussion of Cases 0 and 0a on page 37) and the background frequencies observed in the several drill holes. It is a fairly well known phenomenon that fracture

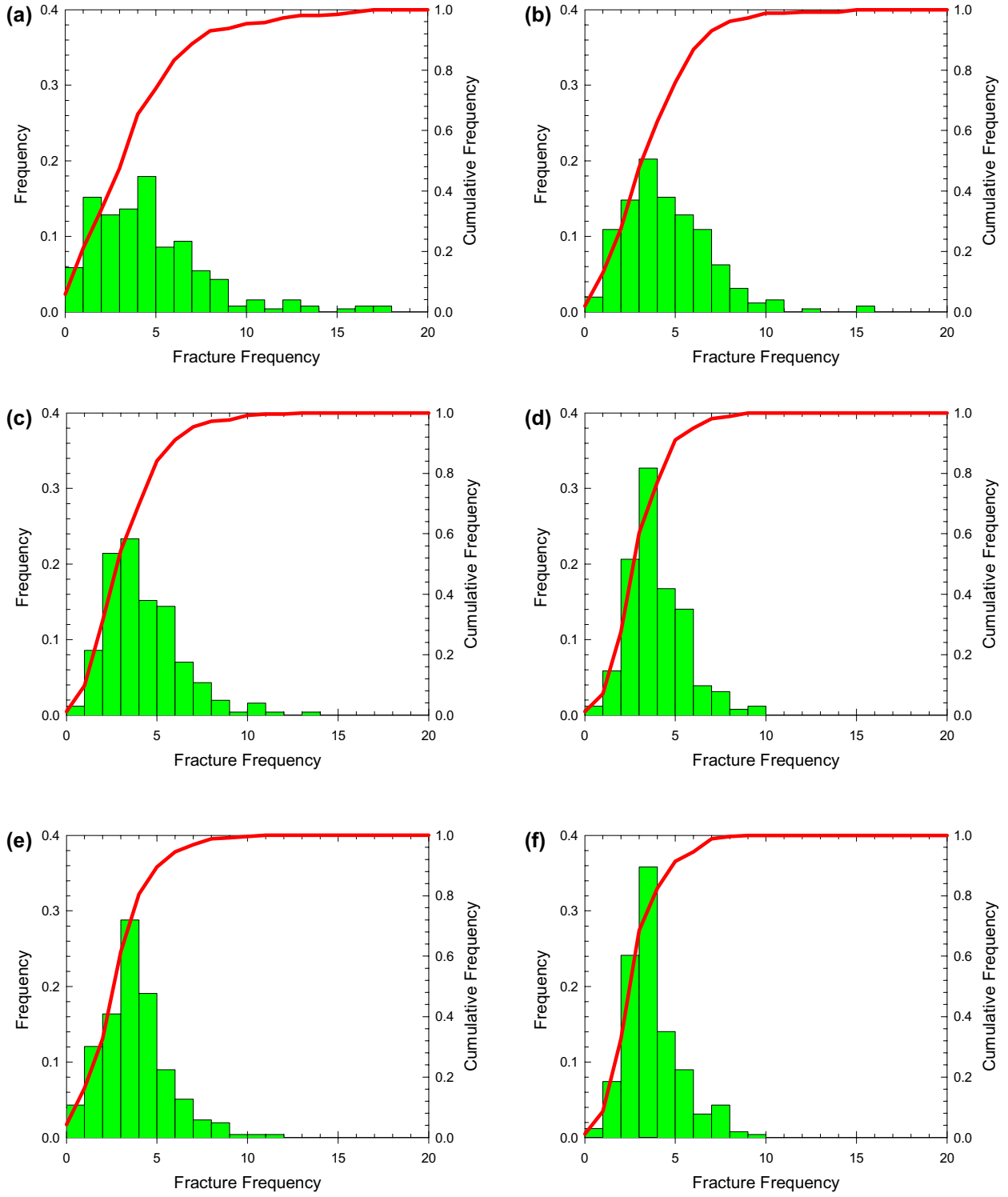

Figure 12. Histograms of composite data sets for (a) Case 1, (b) Case 2, (c) Case 3, (d) Case 4, (e) Case 5, and (f) Case 6.

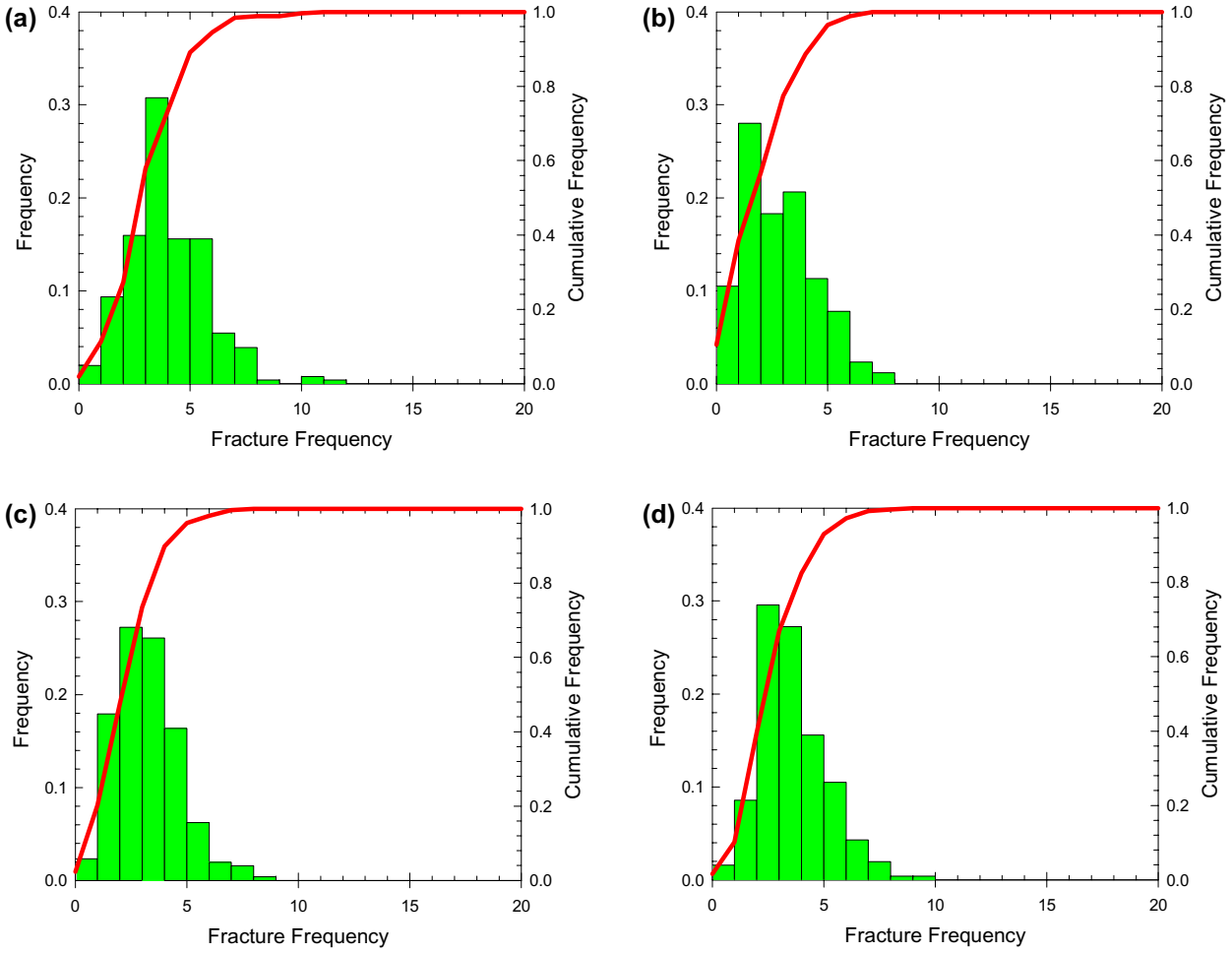

Figure 13. Histograms of composite data sets for (a) Case 7, (b) Case 8, (c) Case 9, and (d) Case 10.

counts along a linear traverse, such as those represented by the data in figures 8 to 11, can be biased by the orientation of line of traverse relative to the orientation(s) of the fracture planes in three dimensions. A similar type of bias may be encountered when counting fractures on a two-dimensional plane as well (e.g., horizontal fractures may be under-represented if the outcrop exposures are dominantly horizontal). No information regarding fracture orientation was available for this modeling effort, and we have not examined the influence of these types of biases on the apparent fracture frequencies involved.

Information Regarding the Tsukiyoshi Fault

Before the drilling of any boreholes at the MIU site, information regarding the Tsukiyoshi Fault is limited to that available from outcrop mapping. This information, presented graphically in figure 2, consists of the outcrop position and any measured dip information. The dip of the Tsukiyoshi Fault is given as approximately 75 degrees at the surface. We have accepted this value as the prior expected dip of the fault, neglecting the fact that the apparent dip in the plane of the

cross section would actually be somewhat less than 75 degrees because of the slight angle between the dip direction of the fault and the plane of the cross section at their mutual intersection. Our interpretation is that this arbitrary decision is of little meaningful consequence, as the difference between apparent and true dip is a function of the sine of the angle between the two directions (very small for small angles). It is also not known precisely where along the trace of the Tsukiyoshi Fault the reported dip of 75 degrees was obtained.

The information available to constrain our modeling of the prior estimates of the fault location and dip vary with the various drilling sequences and cases under consideration (table 3). The geometry of the fault and the specific drill holes involved in the modeled case impose constraints on the fault prior, as does the actual geology encountered in the boreholes involved. A summary of information related to the geometric constraints on the dip of the Tsukiyoshi Fault, as described in the paragraphs that follow, is presented in table 7.

Table 7: Fault Information Based on Information "Available" for Each Case
[All dips in degrees below horizontal; --: entry not applicable; TD: total depth (of drill hole); constraints are elevations]

Case No.	Parameters of Triangular Distribution			Geometric constraint(s) on Fault Dip
	Expected Fault Dip	Dip Lower Bound	Dip Upper Bound	
Case 0	75.0	55	90	none
Case 1–7	64.8	--	--	intersection at –480 m in drill hole MIU-3
Case 8	75.0	55	90	below TD of hole AN-1 at –794.62 m implies a dip > 53.2°
Case 9	75.0	63	90	below TD of hole MIU-1 at –790.93 m
Case 10	64.8	--	--	intersection at –480 m in drill hole MIU-3
Case 10a	64.3	63.3	64.8	poorly defined intersection at about –672 m in MIU-2[1]; below –790.93 m in hole MIU-1

[1] Fault intersections in MIU-2 and MIU-3 not precisely consistent and imply a possible dog-leg bend in the fault plane. This alternate case intended to capture a degree of uncertainty related to imprecise intersection in MIU-2.

Prior to any drilling, the geometry of the fault is essentially unconstrained, although geological reasoning argues that the dip of the fault cannot be greater than 90 degrees (i.e., the direction of dip is known: southward, and that the fault never reverses dip) and that the dip of the fault is most likely to be greater than 55 degrees, based on pre-drilling interpretation of seismic-refractions surveys conducted across the fault trace (Matuoska, personal communication, 2000). This geometry and uncertainty regarding the dip of the fault is presented graphically in figure 14. As described below in the section below on *Generation of Prior Spatial Distributions of Fracture*

Frequency, beginning on page 51, fault dips within this interval of [55°, 90°] are sampled stochastically from a triangular distribution with a modal value of 75 degrees.

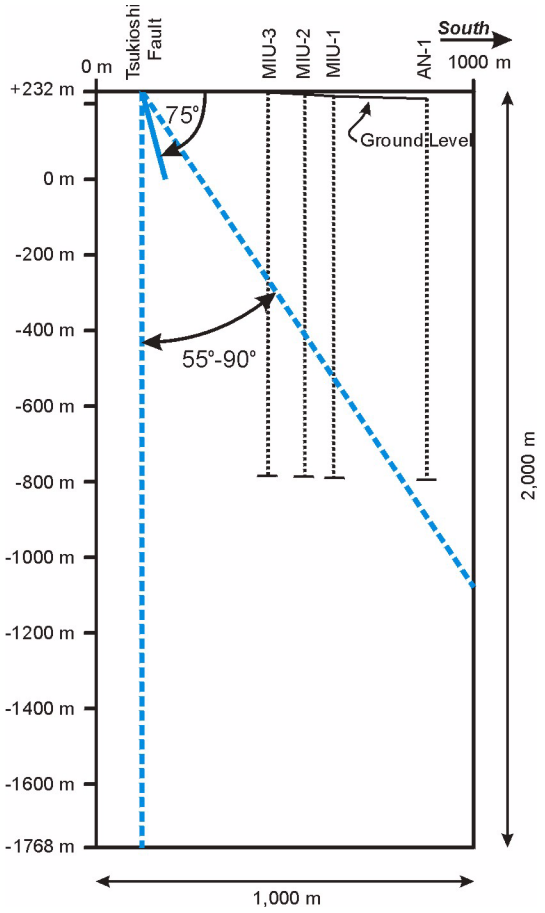

Figure 14. Geometry of the model domain and constraints on the dip of the Tsukiyoshi Fault for the pre-drilling modeling case, Case 0. The dip of the fault at the surface (75 degrees) is indicated, as is the uncertainty envelope imposed by the 55–90 degree geologic constraint. The "future" locations of the four drill holes are provided (dotted lines) simply for reference.

The geometry of the Tsukiyoshi Fault associated with Cases 1–7 derived from Drilling Sequences 1, 2, and 3 (tables 2 and 3) is uniquely constrained by intersection of the fault in the first borehole drilled: MIU-3, which intersected the fault zone at an elevation of –480 m (see the fracture frequency distribution in figure 8). The geometry implied by this fault intersection is presented in figure 15, and implies that the dip of the fault at the surface (75 degrees) overestimates the dip of the fault projected deeper into the earth (68.4 degrees). As a consequence of this clear interception of the Tsukiyoshi Fault in the initial drill hole MIU-3, the fault for drilling Cases 1 through 7 is modeled deterministically with a dip of 68.4 degrees and no uncertainty.

The geometry of the Tsukiyoshi Fault associated with drilling Sequence 4 (table 2) is more complex. Each case corresponding to a step in this sequence (Cases 8, 9, 10, and 4) imposes

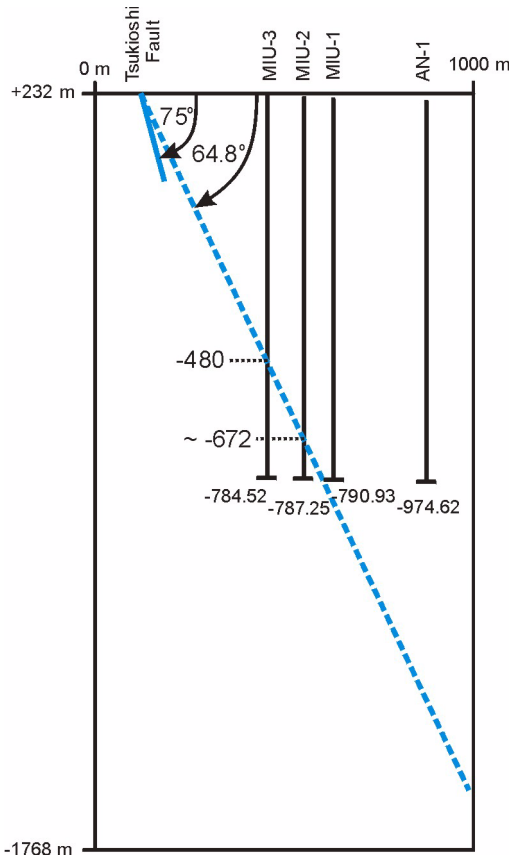

Figure 15. Geometry of the model domain and constraints on the dip of the Tsukiyoshi Fault for modeling case, Case 4 (and, by implication, for Cases 1 to 7). The dip of the fault at the surface (75 degrees) is indicated, as is the actual overall dip implied by the intersection of the fault at an elevation of –480 m in drill hole MIU-3, which is common to all Cases, 1 through 7.

unique constraints that change with the addition of each drill hole. The uncertainty associated with the dip of the fault decreases with the addition of each borehole of the sequence.

The geometry of the first case of Sequence 4, Case 8, is presented graphically in figure 16(a). The first drill hole in Case 8 actually imposes a constraint that the dip of the fault simply must be below the total depth of the hole; this translates to a dip of greater than 53.2 degrees by geometry. However, the geologic reasoning and information from surface geophysics applied to the modeling exercise as a whole suggests that the fault must dip at greater than 55 degrees, with the result that the geometric constraints on the fault for Case 8 are essentially those of Case 0.

Figure 16(b) presents the geometry of Case 9, which involves the addition of drill hole MIU-1 to the control induced by drill hole AN-1. Because the Tsukiyoshi Fault was not intersected in the former borehole, the dip of the fault is constrained to be greater than 63.3 degrees, here taken as 63 degrees for simplicity, as indicated on the figure.

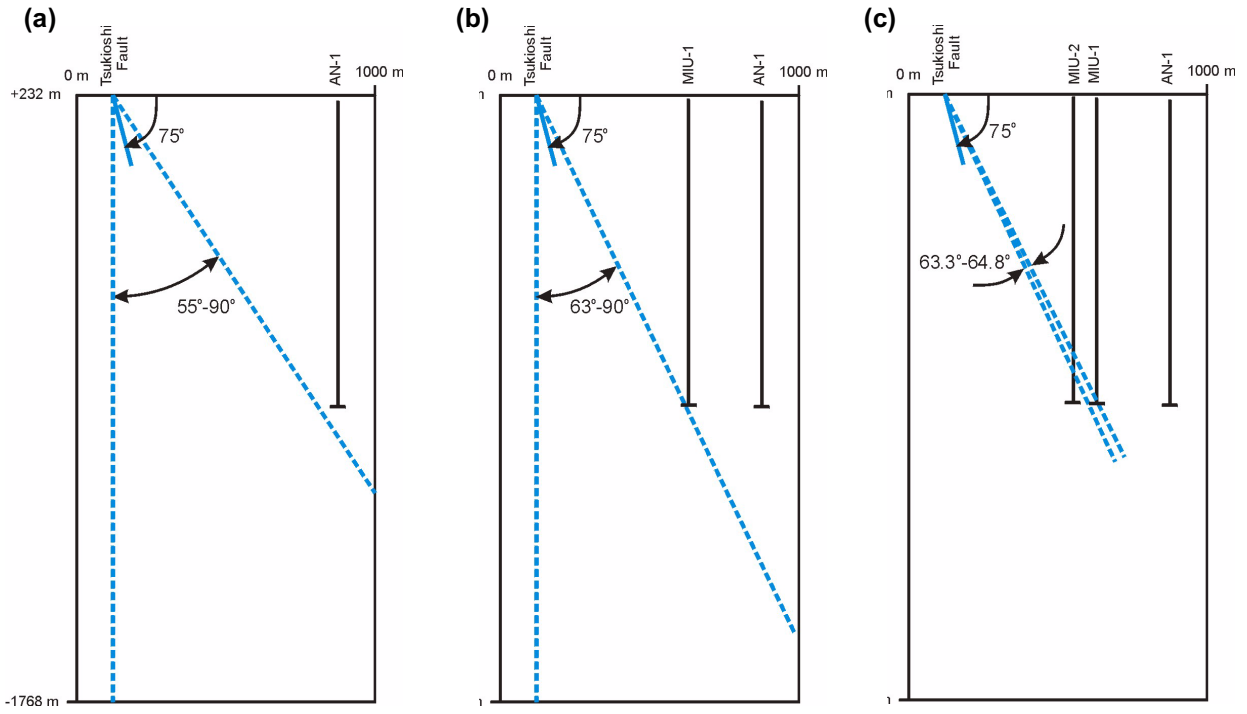

Figure 16. Geometry of the model domain and constraints on the dip of the Tsukiyoshi Fault for (a) Case 8, involving only drill hole AN-1; (b) Case 9, involving drill holes AN-1 and MIU-1; and (c) Case 10, involving drill holes AN-1, MIU-1, and MIU-2. The final case in Sequence 4 is identical to Case 4 (fig. 15).

Case 10, the third step in drilling Sequence 4, involves the addition of borehole MIU-2, as shown geometrically in figure 16(c). MIU-2 intersects the Tsukiyoshi Fault at an elevation of roughly –672 m (see fracture frequency plot of figure 11), which is almost, but not precisely, consistent with the dip of the fault implied by (the as-yet undrilled) hole, MIU-3. As the base case for Case 10, we have simply assumed that the uncertainty with respect to the location of the fault in drill hole MIU-2 is permissive of a fault dip of 64.8 degrees, and have modeled the fault deterministically. In this situation, the fault in Case 10 is identical the fault in Cases 1 through 7 (and to Case 4, which is the final step in Drilling Sequence 4). As a more realistic alternative (given that borehole MIU-3 has not "yet" been drilled), however, we have defined a Case 10a, in which the fault is modeled stochastically, but with the rather tight constraints imposed by the following logic:

1. The fault must dip more steeply than a dip implied by the total depth of borehole MIU-1, since the fault was not intersected in that hole.

2. The fault may not dip more steeply than the 64.8-degree dip implied by (undrilled) hole MIU-3, and which is also essentially compatible with a fault plane passing through the deepest part of the ill-defined low-frequency zone present in drill hole MIU-2 at roughly elevation –685 m (see figure 8).

3. The "expected value of the fault-dip distribution (mode) is compatible with the nominal intersection of the fault with the MIU-2 borehole at an elevation of –672 m, derived through geometry as 64.3 degrees. These geometric constraints are summarized in figure 16(c).

Generation of Prior Spatial Distributions of Fracture Frequency

Recall that under *Accounting for Prior Information Regarding Fracture Frequency* on page 24, we decided to introduce information regarding both (a) the more intense fracturing related to the Tsukiyoshi Fault and (b) the apparent horizontal zonation of background fracture frequency using the geostatistical concept of locally varying mean values [equation (1)]. This approach requires that we construct numerical fields, one for each simulation, describing this prior information at all grid nodes. To generate these fields, which we term ***fault-prior models***, we use the information constraining the dip (and subsurface location) of the fault from table 7, together with information on fracture frequency from table 5 (for Case 0) and from the data sets (drill hole profiles) associated with each individual drilling case (Cases 1 through 10; table 6).

The process is mathematically fairly simple, and the geometry involved is represented graphically in figure 17. The steps in the process may be summarized as follows:

1. Generate a stochastic fault dip, α, from the appropriate triangular distribution described by the constraints (expected dip, upper and lower bounds on that dip) in table 7. If the case in question is constrained by an intercept of the fault itself, the fault dip is deterministic (single valued).

2. At each grid node, $P(i,j)$, of the modeling mesh (4-m by 4-m nodes), compute the coordinates, $P(x,z)$, of intersection of the fault line with a normal to that line passing through $P(i,j)$. Note that $P(x,z)$ will fall precisely on a grid node only fortuitously.

3. Compute the perpendicular distance, d, (figure 17) of the relevant grid node, $P(i,j)$, from the center of the fault zone, $P(x,z)$, the fault trace.

4. The "contribution" of the elevated fracturing associated with the fault at this grid node (*above* the background frequency modeled at this same node) is computed as proportional to the maximum observed fracture frequency in the data set as weighted by a Gaussian-decay function and determined by the distance computed in step 3. Figure 18 illustrates the concept of this decay function. The 2-sigma width of the fault zone is assumed to be 40 m.

5. If the current grid node, $P(i,j)$, is located less than 5 m from the trace of the fault, the node is determined to be within the "core" of the fault, and the fracture frequency contribution of the fault is assumed to be zero, and thus the assigned fracture frequency in the core is set to the background frequency; see figure 18. This approachis compatible with a geologic interpretation of the presence of fault gouge or other alteration that effectively obliterates discrete fractures; see the low-frequency zone at approximately

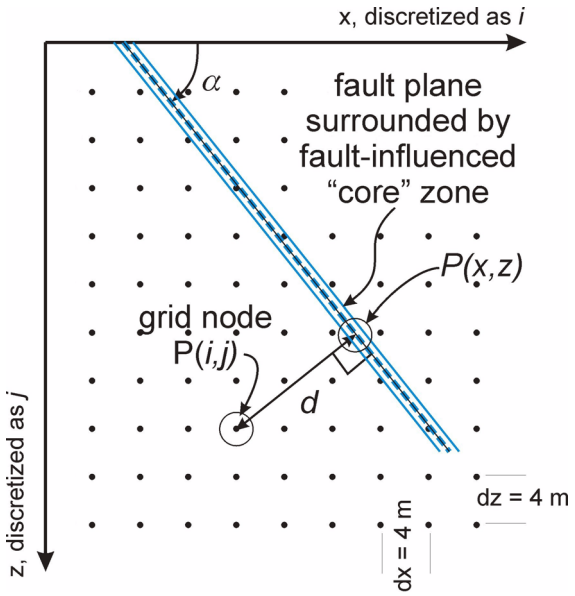

Figure 17. Conceptual representation of geometry involved in computing the intensity of fracturing associated with the Tsukiyoshi Fault for the prior model of fracture frequency. Fault-related fracturing is assumed to decrease with increasing distance, *d*, from the fault following the Gaussian-decay model shown in figure 18. Not to scale.

–480 m elevation in drill hole MIU-3 (figures 7 and 8). This type of fault model is consistent with one proposed by Caine and others (1996).

6. The background fracture frequency and the fault-related fracture frequencies are combined and used as the prior-estimate locally varying mean value in the simulation process, and used as such as required by equation (1).

Figure 19 presents color-coded pixel maps of the prior fields of fracture frequency related to each modeling case described in table 3. These images represent the locally varying mean values that provide the estimate of *m* in equation (1) during the kriging portion of the simulation algorithm. Note that the values represented by the various parts of figure 19 are presented *in log space* for visualization purposes only. In some instances, there is not a great deal of actual variability among the three different geologic zones identifiable in the composite drill hole data sets, and use of a logarithmic scale for color coding simply accentuates these minor differences.

Part (a) of figure 19 shows the prior estimate for Case 0, the pre-drilling case. As there are no subsurface data, the entire field exhibits a uniform prior expectation, modified only by fault-related fracturing. Note, however, that this expectation, which is derived from the outcrop measurements presented in table 5 and the associated discussion, is markedly higher at ~8 fractures per meter than is the expectation for any of the cases that involve "completed" drill holes. *Apparently the expectation based on surface information is significantly in conflict with respect to the subsurface.* Additionally, the fracture frequencies associated with the fault, which is modeled stochastically, are not that markedly greater than the background frequency. The result is that the

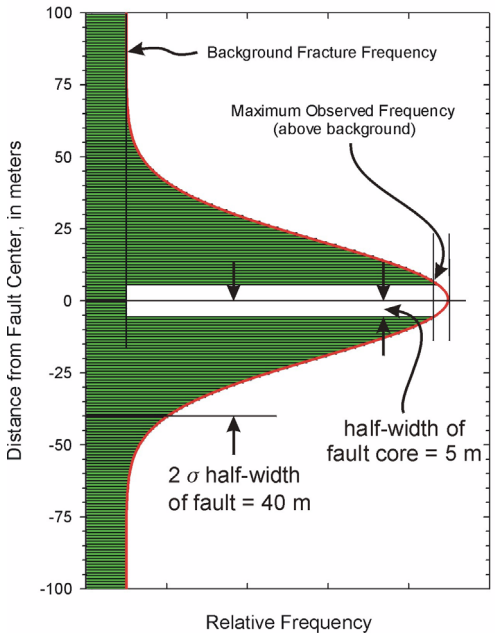

Figure 18. Conceptual representation of the Gaussian-decay function for fracture frequency with increasing distance from the fault plane. The two-sigma width of the fault zone is 40 m, and the corresponding (one-sided) width of the fault core is 5 m. Note that the "maximum observed frequency" is not the same as the "peak" fracture frequency implied by the Gaussian model.

multiple realizations of the fault plane are not readily visible in the color-scaled plot. Note that the color scale for part (a) runs from 0.1 m^{-1} to 100 m^{-1}, in contrast to the color scale for all other parts of figure 19.

Part (b) of figure 19 shows the deterministic fault prior that is common across Cases 1 through 7, and which is also used in Case 10. The fault dips at 75 degrees, and the three geologic zones of differing fracture intensity are defined by the down-hole plots of the composite data sets (figures 9 and 10). This deterministic prior is defined essentially by drill hole MIU-3, which is the first hole to be "drilled" under Sequences 1, 2, and 3.

Figure 19, parts (c) and (d), are associated with Drilling Sequence 4, which starts out (Case 8) with drill hole AN-1, and continues with the addition of holes MIU-1 (Case 9) and MIU-2 (Case 10). Drill hole AN-1 scarcely constrains the stochastic nature of the fault dip at all, as the shallowest possible dip of the fault, which was not intersected in the borehole) is flatter [figure 16(a)] than the minimum dip value deemed likely (55 degrees) based on the pre-drilling geophysical interpretation (Matsuoka, personal communication, 2000). In effect, the fault prior for Case 8 is identical to that for Case 0 [figure 19(a)] — and more visible in the images because of the difference in magnitude of fracture frequencies between the fault-related fracturing and the background frequency. Also, the down-hole spatial distribution of frequencies identified in drill hole AN-1 has been used to define a layered, spatially varying prior distribution of background frac-

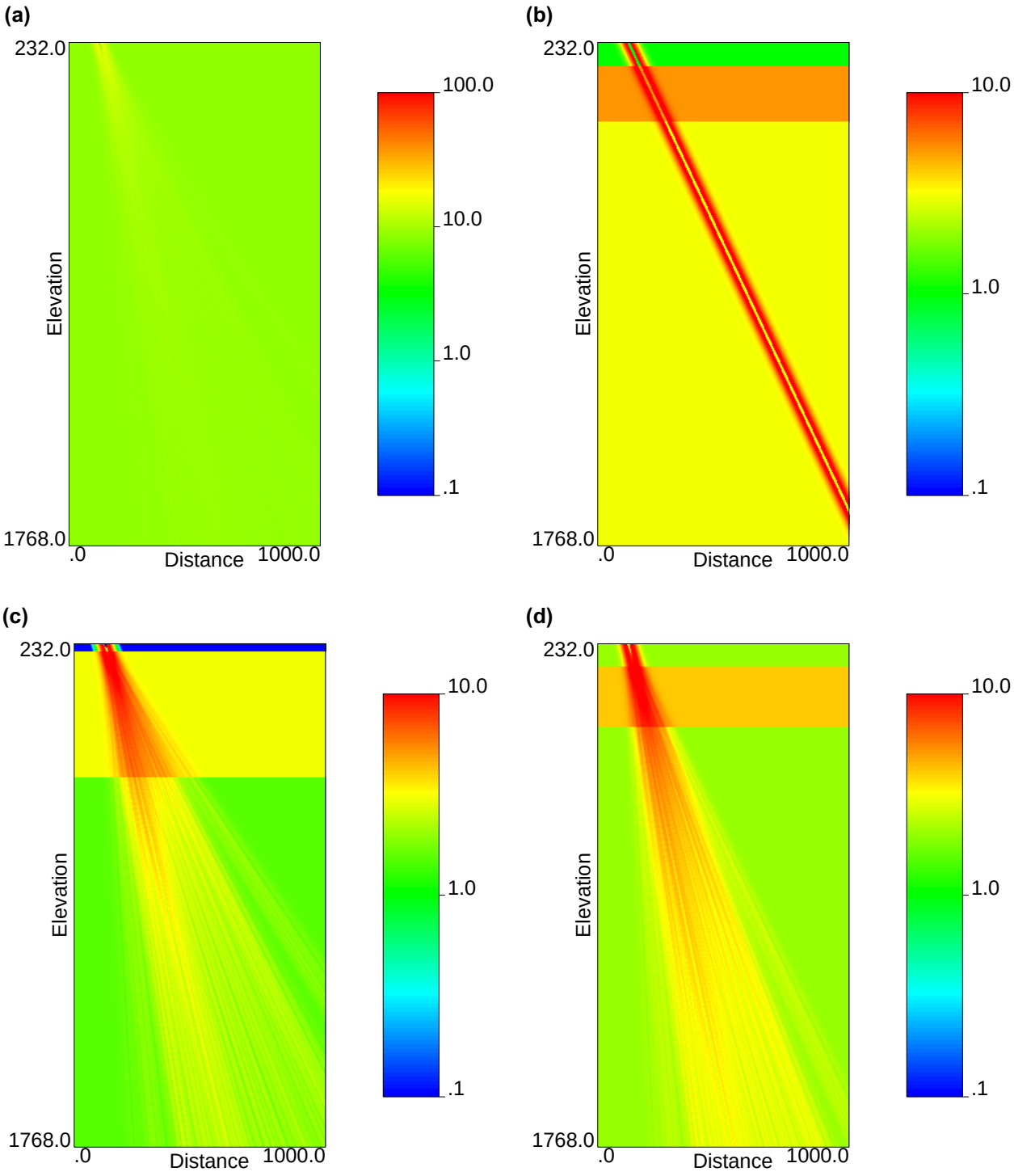

Figure 19. Color-scaled images of prior fracture-frequency E-type models for (a) Case 0, (b) Cases 1–7 *and* Case 10 (deterministic prior), (c) Case 8, and (d) Case 9. Note the expanded logarithmic scale in part (a). The *logarithmic* color scale in these (and all subsequent figures) shows fracture frequency in units of m^{-1}.

ture frequency in figure 19(c). This lower collar elevation of this single-hole data set (see figure 10) allowed the inference of only a two-zone prior-frequency model (the prior estimate of fracture frequency in the top "zone" was set equal to zero).

Figure 19(d) continues Drilling Sequence 4 with the addition of drill hole MIU-2. The dip of the fault for this case must be steeper than indicated for the base of the borehole, as indicated in figure 16(b). Comparison of figures 19(c) and (d) confirms that the region of greater fault-related fracturing in part (d) is, in fact, more tightly constrained than that of part (c).

Figure 20 presents the fault priors for the alternate modeling cases of table 4. Figure 20(a) shows the pre-drilling Case 0a, for which the estimate of the background fracture frequency has been lowered to a value (2.23 per meter) more consistent with the frequencies observed (later in the drilling sequences) in the subsurface. The value used is the area-weighted average of the two outcrops located north of the Tsukiyoshi Fault (in the footwall block; table 5) and the background fracture frequency expectation is uniform across the entire modeled domain.

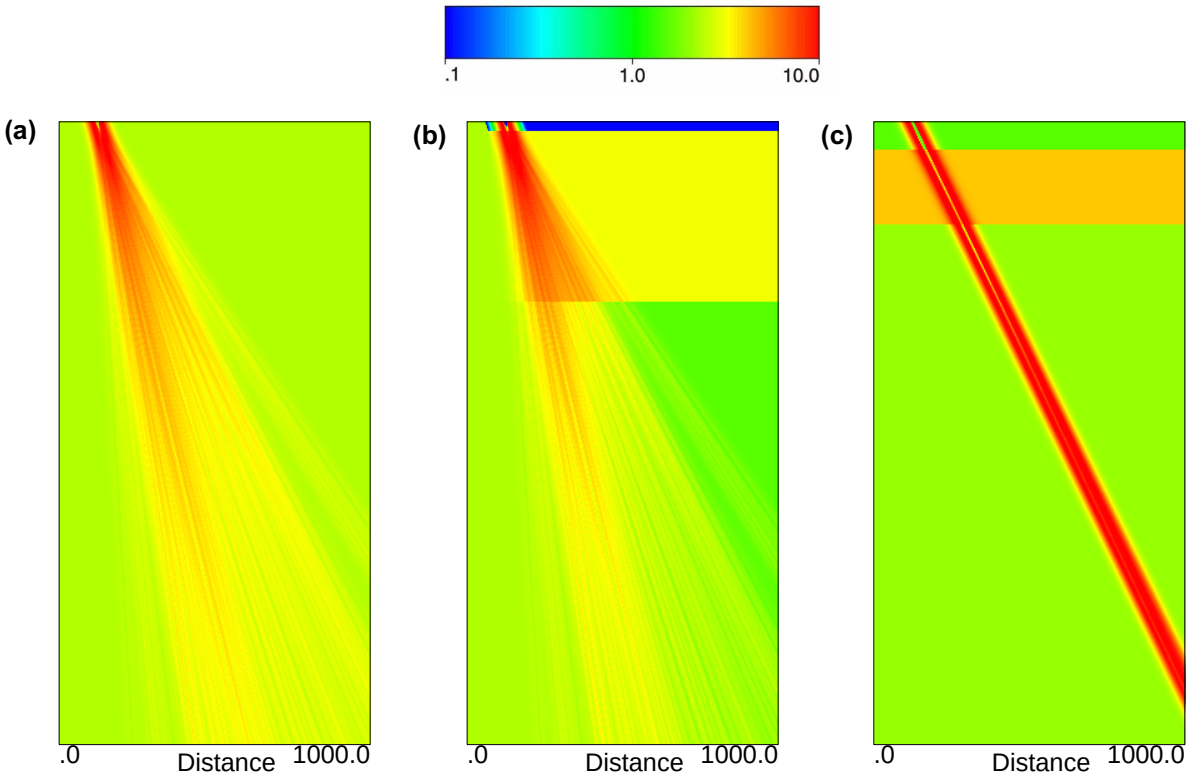

Figure 20. Color-scaled images of prior fracture-frequency E-type models for (a) Case 0a, (b) Case 8a, and (c) Case 10a. Color scale is logarithmic between 0.1 and 10 fractures per meter.

Figure 20(b) represents Case 8a. Case 8a attempts to continue the distinction between footwall and hanging wall structural domains, introduced briefly on page 37 with respect to the measured outcrop fracture frequencies. For this alternative modeling case, all grid nodes below

the plane of the Tsukiyoshi Fault, which is modeled stochastically according to table 7, are assigned a geological prior expectation derived from the footwall outcrop frequencies (table 5), and nodes above the fault are assigned prior values based on the geology of drill hole AN-1. Note that because of the hanging wall-footwall distinction, the layering of fracture frequency is present only on the southern (right-hand) side of the Tsukiyoshi Fault.

Figure 20(c) presents the fault prior for Case 10a, the stochastic equivalent of Case 10, in which the geometry of the fault at depth is allowed to vary within the relatively restrictive constraints imposed by boreholes MIU-1 and MIU-2 [figure 16(d)]. Direct comparison of figures 19(b) and 20(c) for Case 10 and 10a, respectively, indicates that the differences between these two cases is very minor (the fault-influenced zone is only slightly thicker in Case 10a and, on average, lacks a clearly defined core across the 100 realizations). Note that the differences are greater at depth than near the surface.

Observed Spatial Correlation Patterns

A tabular summary of the variogram parameters used to model the experimental variograms computed for the several modeling cases of the four drilling sequences are presented in table 8. The variograms themselves, both experimental and modeled, are presented in figures 21 through 23, one for each case. In general, three nested structures were used to model the experimental data.

Modeling of the experimental variograms is driven largely by the detailed variograms that can be computed in the vertical (down-hole) direction. Fitting of horizontal models is largely arbitrary, because of the very sparse number of horizontal separations computable from a maximum of four drill holes. However, some of this arbitrariness is reduced because the form of the fitted model must be the same in all directions: if two spherical models and a Gaussian are nested in the vertical dimension, those same three types of models must apply in the horizontal direction as well. Additionally, the ***anisotropy ratio*** between the range of correlation evident in the vertical dimension and in the horizontal dimension has typically been held as a constant for the different structures, unless the horizontal experimental variogram plot appears to contain definite evidence to the contrary. Notes on fitting variograms for each of the different cases are included in the paragraphs that follow.

Table 8: Variogram Parameters for Fracture Frequency Simulations

Case ID	Nugget	Sill	Model	Horizontal Range (m)	Vertical Range (m)
Case 0	0.1	0.90	Spherical	500	100
Case 1	0.1	0.40	Spherical	75	15
		0.40	Gaussian	300	60
		0.40	Gaussian	750	150
Case 2	0.1	0.30	Spherical	30	15
		0.35	Spherical	150	60
		0.25	Gaussian	500	250

Table 8: Variogram Parameters for Fracture Frequency Simulations (Continued)

Case ID	Nugget	Sill	Model	Horizontal Range (m)	Vertical Range (m)
Case 3	0.1	0.35	Spherical	30	15
		0.30	Spherical	200	75
		0.25	Spherical	400	275
Case 4	0.1	0.35	Spherical	60	15
		0.20	Spherical	90	90
		0.35	Spherical	400	250
Case 5	0.1	0.30	Spherical	75	15
		0.30	Spherical	350	70
		0.30	Gaussian	1000	250
Case 6	0.1	0.40	Spherical	40	20
		0.20	Spherical	160	80
		0.30	Spherical	500	250
Case 7	0.1	0.30	Spherical	30	15
		0.25	Spherical	100	75
		0.35	Gaussian	400	250
Case 8	0.1	0.40	Spherical	40	20
		0.10	Spherical	270	135
		0.40	Gaussian	300	150
Case 9	0.1	0.50	Spherical	40	20
		0.10	Spherical	220	110
		0.30	Gaussian	250	125
Case 10	0.1	0.40	Spherical	30	15
		0.20	Spherical	100	110
		0.30	Gaussian	350	200

Variograms for Case 0 — There is no experimental variogram for the pre-drilling case, Case 0, as there are no subsurface data from which to compute such an experimental plot using equation (2). Potentially, one might have been able to compute an analogue variogram using data from other (pre-existing) drill holes or from outcrop measurements. However, such data were not available to us, with the result that the variogram model for Case 0 (and for Case 0a) is wholly an assumption. This assumed variogram model is presented in figure 21. The variogram parameters are presented in table 8, and the horizontal-to-vertical anisotropy ratio of 5:1 is based loosely on discussions with JNC Tono Geoscience Center staff (personal communication, 2000).

Variograms for Case 1 — Figure 22(a) presents variograms for Case 1. The modeling is based solely on the down-hole experimental variogram, shown in the red dots. The modeled variogram for the horizontal dimension was generated by arbitrarily assuming a horizontal-to-vertical anisotropy ratio of 5:1 from Case 0. The experimental variogram has been fitted by a three-part nested structure that includes two Gaussian-type models and a short-range spherical model (table 8). Although the experimental variogram exhibits definite hole-effect-type (sine-wave-like) oscil-

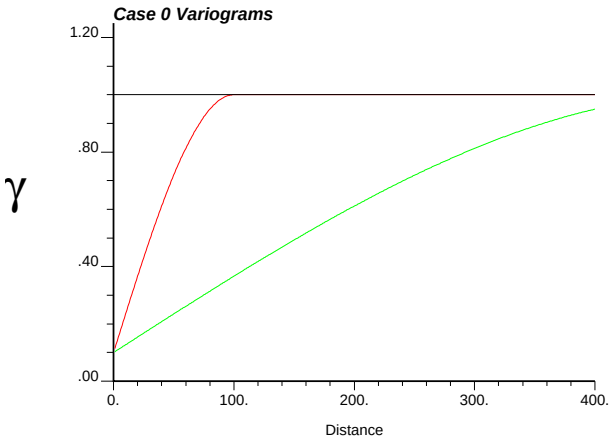

Figure 21. Variogram model for pre-drilling Cases 0 and 0a. Model variogram in the vertical direction is the shorter-range (upper) curve; lower curve is the variogram in the horizontal direction.There is no experimental variogram plots for this case, as there are no subsurface data prior to drilling.

lations, hole-effect variograms are notoriously difficult to model, and we have elected to fit the overall change in variability with the nested model as shown.

Variograms for Case 2 — Figure 22(b) presents variograms for Case 2, which contains two drill holes. Note that the hole-effect oscillations are much damped, in comparison with figure 22(a), or Case 1. For Case 2, the horizontal variogram has been constrained by the two experimental data points shown on the figure. Although there is functionally only a single variogram value (the two separations represented in the horizontal dimension are essentially identical), the impression conveyed by these two nearly coincident points is that the anisotropy ratio may be closer to 2:1 than to 5:1. Accordingly, each of the range parameters of the fitted model (table 8) has been adjusted to reflect this increase in information.

Variograms for Case 3 — Figure 22(c) presents variograms for Case 3, the three-drill-hole continuation of Drilling Sequence 1. In fact, the variogram for Case 3 appears very similar to that for Case 2 [figure 22(c)], and the impression of a horizontal-to-vertical anisotropy ratio closer to 2:1 than to 5:1 is confirmed by the additional experimental points for the horizontal variogram. The fitting parameters of the variogram model are presented in table 8.

Variograms for Case 4 — Figure 22(d) presents variograms for Case 4, the four-hole completion of Drilling Sequence 1 and, indeed, this case represents maximal data set available for and the culmination of all four drilling scenarios. With the additional pairs of variogram values that can be computed in the horizontal dimension with all four drill holes present, the horizontal variogram is actually fairly well defined. Interestingly, the horizontal-to-vertical anisotropy ratio for this maximal-data case is indicated as being markedly closer to 1:1, than had been suspected for the "earlier" cases of this drilling scenario. In fact, an isotropic distribution of fracture frequency is not unexpected in a massive, plutonic environment. Although our initial assumption of some degree of layering, based to some extent on the presence of the layered sediments overlying the post-granite unconformity, appears to be in error, the change in prior geologic model is consistent

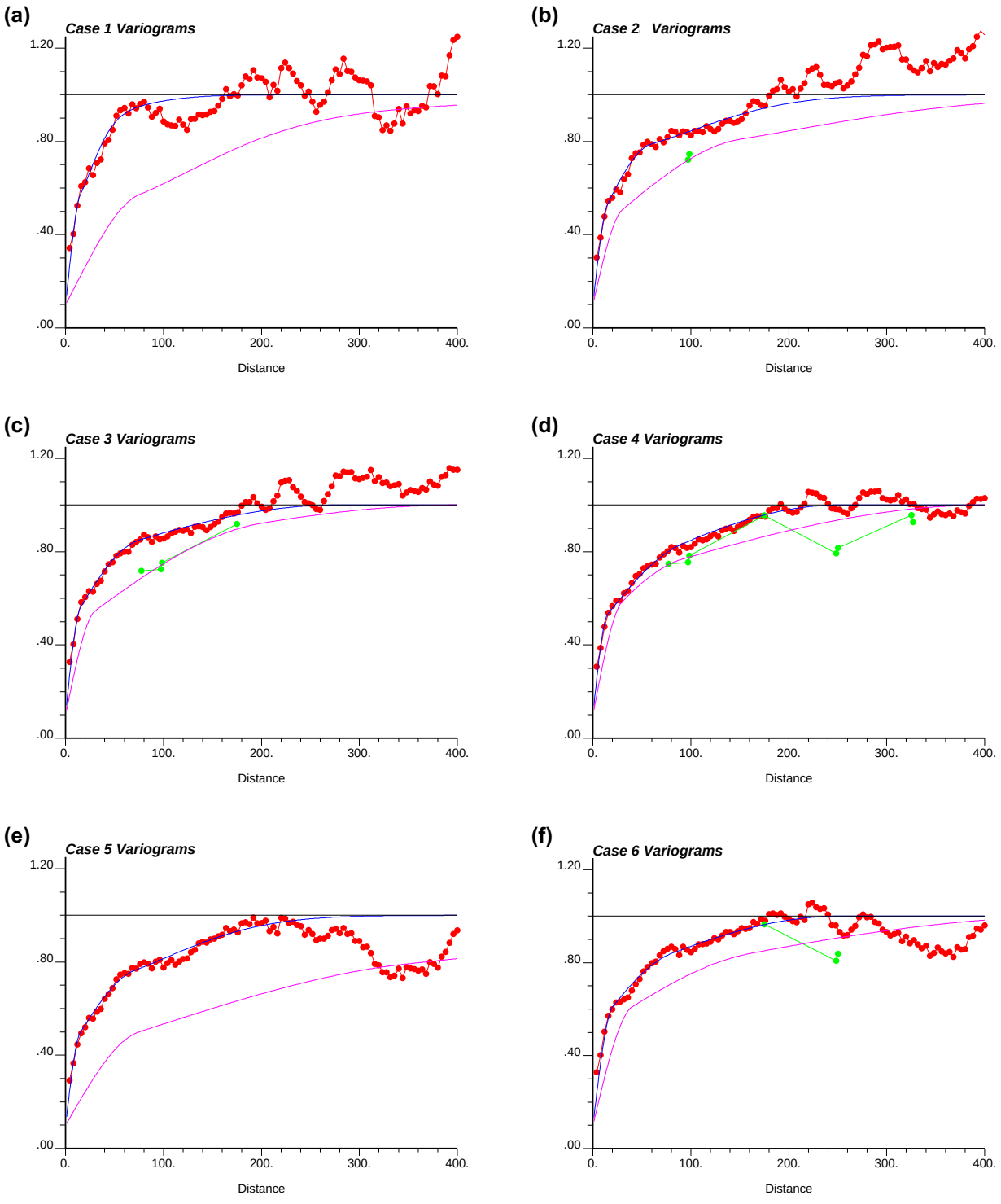

Figure 22. Variograms with fitted models for (a) Case 1, (b) Case 2, (c) Case 3, (d) Case 4, (e) Case 5, and (f) Case 6). Experimental (data) variograms are shown as curves with symbols; fitted models are smooth curves without symbols. Variograms in the vertical direction are the shorter-range (upper) pair of curves (model in blue); lower two curves are variograms in the horizontal direction (model in magenta).

with the progressive addition of information to the knowledge base. The variogram model parameters are tabulated in table 8.

Variograms for Case 5 — Figure 22(e) presents variograms for Case 5, the two-drill-hole successor to Case 1 that is common to Drilling Sequences 2 and 3. The spatial arrangement of these two drill holes does not provide any information on spatial correlation patterns in the horizontal dimension, and our choice of an anisotropy ratio has reverted to the original, pre-drilling instance of 5 to 1. Note that in common with the two-hole case for Drilling Sequence 1 (Case 2), the apparent hole-effect oscillations are much reduced over those of Case 1, and the effect is only apparent at distances close to the longest range structure. Fitting parameters for the variogram model for Case 5 are presented in table 8 also.

Variograms for Case 6 — Figure 22(f) presents variograms for Case 6, which represents the three-hole incremental step of Drilling Sequence 2. This case provides the first objective evidence for a horizontal range in Sequence 2 that is different from the default assumption of 5:1, although the two experimental data points are somewhat ambiguous. The shorter of the two separation values could be interpreted to imply a ratio of 1:1 (presumably the "correct" interpretation, as determined from the as-yet undrilled Case 4, described previously for Drilling Sequence 1). However, in keeping with the postulated sequence of drill holes and our prior assumption of some layering effects, we have "split the difference" between the two experimental variogram points in the horizontal dimension and fitted a variogram model consistent with an approximate 2:1 horizontal to vertical difference in the range of the correlation structures. The parameters of this final model are give in table 8. Note that the progression of drilling sequence 2 is completed as Case 4, for which the variogram modeling has already been described above.

Variograms for Case 7 — Figure 23(a) presents variograms for Case 7, which represents the three-hole incremental step of Drilling Sequence 3. The two "earlier" members of this sequence are Cases 1 and 5, described above. Note that the addition of drill hole MIU-2, instead of MIU-1 as the third drill hole following the unguided modeling of horizontal spatial structure in Case 5, has provided significant information via the two short-separation-distance data points that bring our interpretation of short-range correlation structure close to the data-rich estimate of 1:1 for the final Case 4. Indeed, in "retrospect" of Case 4, the final drilling step in Sequence 3, one would be tempted to have fitted an isotropic variogram model to the horizontal data points in figure 23(a). However, following the incremental approach of a progressive drilling sequence, we have been guided by our prior assumption of some horizontal-to-vertical anisotropy, and fitted parameters (table 8) that reflect an anisotropy ratio of somewhat less than 2:1, as permitted by the experimental data.

Variograms for Case 8 — Figure 23(b) presents variograms for Case 8. Recall that Case 8 represents addition of the first borehole in Drilling Sequence 4 after the pre-drilling Case 0 (table 2). As might be suggested by the differences between drill hole AN-1 and the other drill holes (see figure 8 for the raw data sets), including the lack of obvious fault-related fracturing and an obscure relationship between fracturing and the upper sedimentary horizons, the experimental variogram shown in figure 23(b) is quite different from any of the experimental variograms considered thus far for the other drilling sequences. There is a marked difference in range between the shortest correlation structure and the other two components of the nested model. The down-hole

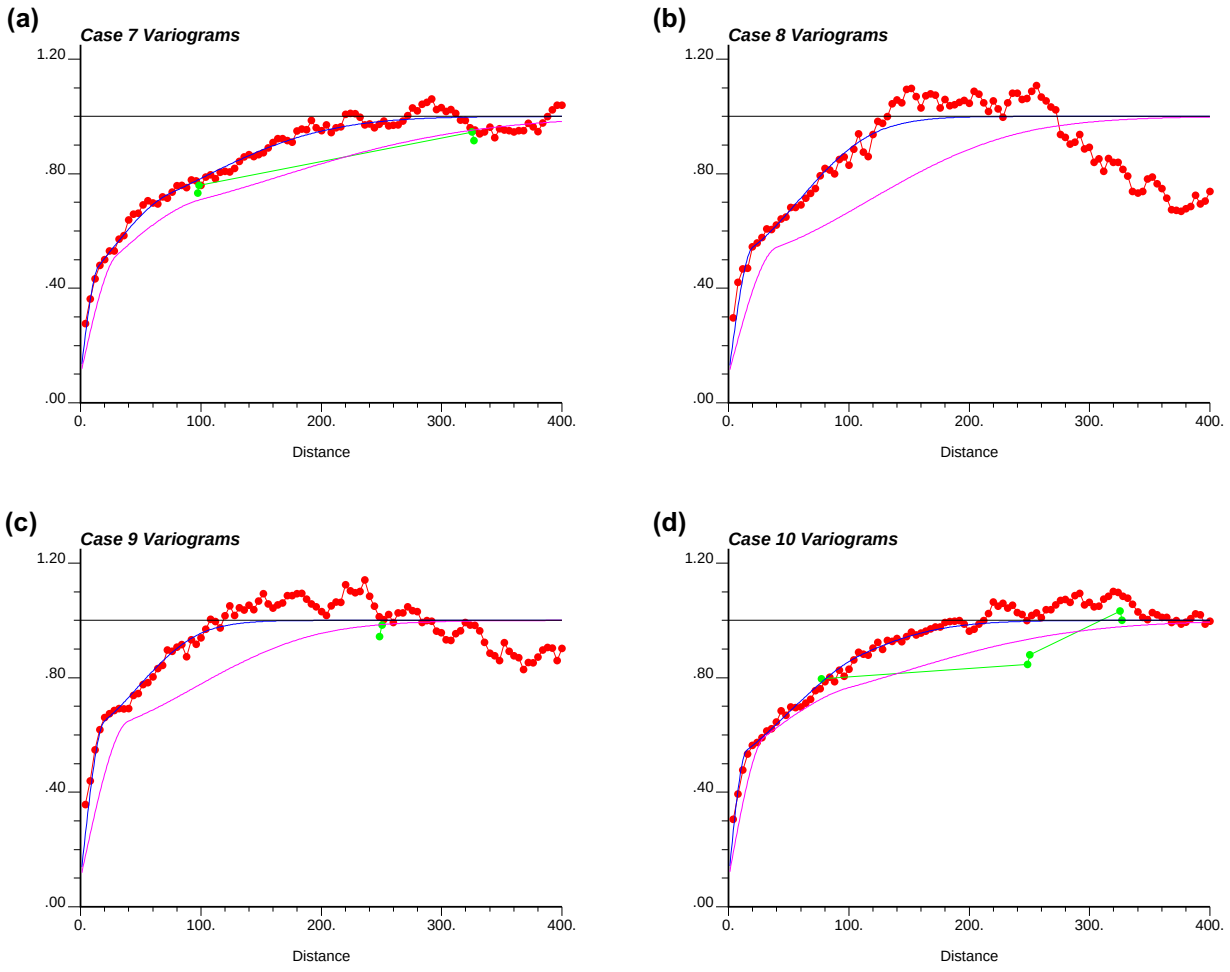

Figure 23. Variograms with fitted models for (a) Case 7, (b) Case 8, (c) Case 9, and (d) Case 10. Experimental (data) variograms are shown as curves with symbols; fitted models are smooth curves with out symbols. Variograms in the vertical direction are the shorter-range (upper) pair of curves (model in blue); lower two curves are variograms in the horizontal direction (model in magenta).

experimental variogram has been fitted with a three-part nested structure, the parameters of which are presented in table 8.

Variograms for Case 9 — Figure 23(c) presents variograms for Case 9, the next step in Drilling Sequence 4, and this case provides the first objective evidence for a horizontal range of correlation. Although this single experimental data point is consistent, in "retrospect," with to the ultimate, presumably correct spatial correlation model from Case 4 of isotropic correlation, we have fitted the horizontal experimental variogram as reflecting a 2:1 anisotropy ratio. The parameters of this slightly modified three-nest structure are given in table 8.

Variograms for Case 10 — Figure 23(d) presents variograms for Case 10, the three-hole progression of Drilling Sequence 4. There is something about this spatial configuration of drill holes that much reduces the sharp knick-point at separation distances of approximately 20 m in the down-hole experimental variogram, and which changes the entire character of the spatial

model. Indeed, figure 23(d) resembles the several variograms of figure 22 more closely than do figures 23(b) and (c). Also evident in this variogram for Case 10 are indications that there is some horizontal-to-vertical anisotropy, as suggested by the two experimental data points at separations of approximately 250 m. However, the shorter-range correlation structure appears to have an anisotropy ratio much closer to the ultimate 1:1 that is provided by the final step in Sequence 4, which is Case 4, a previously described. Parameters of the three-part nested structure fitted to the variograms of figure 23(d) are given in table 8.

Variograms for Alternative Modeling Cases — Note that the input variogram models used for the alternative modeling cases, Case 0a, Case 8a, and Case 10a, are precisely identical to those used in the corresponding baseline cases. The drill-hole data contents of the alternative modeling cases are unchanged from those of the baseline cases, and it is other aspects of the conceptual modeling framework that form the distinctions.

MODELING RESULTS

General

Simulation as a modeling technique produces a great deal of material that must be evaluated in order to provide meaningful results. The evaluation that must be undertaken is dependent upon the objectives of the study itself. For example, if the objective of this study had been to examine the flow consequences of uncertainty in the fracture frequency distribution, individual simulations from the various modeling cases would need to have been post-processed through a suitable simulator of ground-water flow and contaminant transport. Although there is some interest in the further implications of uncertainty in fracture intensity at the MIU site, the scope and objectives of this study were specifically somewhat more limited:

1. to describe the uncertainty associated with our understanding of the spatial distribution of fracture frequency throughout the model domain, and

2. to assess how that uncertainty changes from the pre-drilling case as information from up to four deep drill holes is added, one hole at a time, and in different sequences.

These objectives make the task of sifting through the simulation results for the many cases defined in tables 3 and 4 somewhat more straightforward.

We present the results of this study of fracture frequency at the MIU site in two principal sections. First, we focus on comparing the overall ***expectation*** of spatially variable fracture frequency, as represented by the E-type models of Deutsch and Journel [1998; also equation (3)] among the various modeling cases. We also examine the overall ***uncertainty*** in those expectations, as reflected in graphical plots of the spatially varying conditional standard deviation [equation (4)] associated with the E-type models. It is also instructive to consider how the uncertainty in the final E-type models is related to both the prior frequency models and to uncertainty in those prior frequency models. These first types of results will be presented by case and also graphically in the context of the hypothetical drilling sequences defined in table 2.

Second, we present overall summary measures that attempt to capture, in a single quantity [although two variants are given by equations (6) and (7)], some representation of the uncertainty associated with the progressive addition of objective information (frequency data) through the course of a drilling campaign. These summary uncertainty measures will also be presented by case and by drilling sequence.

Comparison of Summary E-Type Models with Prior Models

The Pre-Drilling Case

Figures 24 and 25 present graphical, pixel maps showing the prior fracture-frequency model and the average of the final simulated models for both of the two alternative pre-drilling cases, Case 0 and Case 0a. As will be the situation for most of the figures in this section, the top half of the figure presents the fault-prior information (including uncertainty in the prior informa-

tion for stochastic prior models), and the lower half of each figure presents the E-type model and conditional standard deviations for each modeling case.

Figure 24 shows these summary images for Case 0 whereas figure 25 shows the identical images for Case 0a. Recall that the only real difference between Case 0 and Case 0a is the background fracture frequency inferred from the outcrop data. Specifically, Case 0 used the overall, area-weighted fracture frequency from all six outcrop regions described in table 5. This expected frequency value of 8.41 fractures per meter represents the most logical prior expectation, knowing nothing else regarding the geology of the site. In contrast, Case 0a used the area-weighted fracture frequency associated with the footwall outcrops (two locations only; table 5). The choice of this value, 2.23 fractures per meter, was selected in a non-objective manner as more similar to the background fracture frequencies encountered at depth in the holes that would be drilled "later" in each hypothetical drilling sequence. However, selection of such a lower expected value for the pre-drilling case might have been justified by geologic evidence (unavailable to us) regarding known weathering or alteration of fractures on outcrop, particularly for exposures within the hanging-wall structural domain, knowledge of the relationship between the studied outcrops and proximity to the Tsukiyoshi Fault, or other factors.

Figure 24 demonstrates that overall there is relatively little contrast between the overall prior expectation of fracture frequency (~8.4 m^{-1}) and the expectation of fault-related fracture frequency (~7 m^{-1} above the background). This lack of marked contrast is evident both in the E-type models of the 100 stochastic priors [part (a) of the figure] and in the E-type uncertainty model of the 100 unconditional simulations [part (c)]. Lacking any constraints on the fault location (other than the range of realistic dips and the observed surface "expectation" of dip), the replicate simulated models vary greatly from one another, with the result of relatively large and essentially homogeneous uncertainty, as indicated by the conditional standard deviations in part (d) of the figure. Note that there is some horizontal layering of fracture frequency present in the E-type model. This type of layering is much more strongly expressed in the individual simulations for this modeling case. However, as there is no subsurface conditioning data to constrain high values (or low values) to the same spatial position in different simulations, the layering should progressively disappear as the number of simulations used in computing the E-type model increases. That layering persists at all in the E-type model of figure 24(c) is a consequence of the 5:1 horizontal-to-vertical anisotropy ratio *assumed* for the spatial correlation structure (variogram).

In comparison to figure 24, figure 25 exhibits some visual contrast, both in terms of the expected fracture frequency related to faulting and in the uncertainty associated with this expectation, simply because of the contrast between background fracture intensity (~2.2 per meter) and that fracturing believed associated with the fault itself (~13 per meter above background). The uncertainty associated with the stochastic positioning of the fault is clearly indicated in the various parts of figure 25, and that this type of uncertainty is related solely to the prior models input as fields of locally varying mean values to the simulator. Notice also that the magnitude of the uncertainty values is directly proportional to the magnitude of the expected frequencies. Higher fracture frequencies associated with the fault are associated with greater uncertainty.

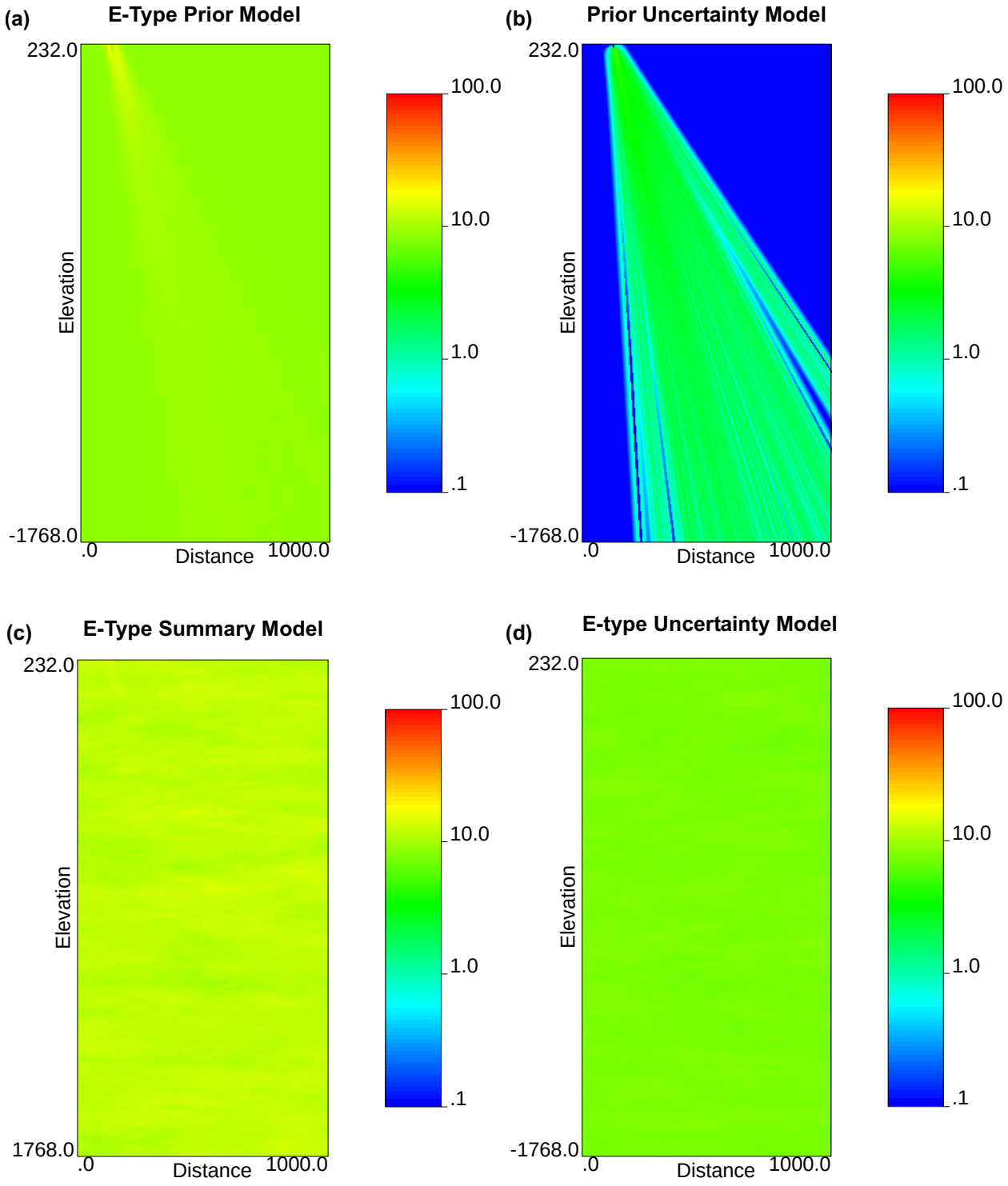

Figure 24. Comparison of prior fracture-frequency model with summary E-type model and conditional standard deviation model for pre-drilling Case 0. (a) E-type model of fault priors; (b) conditional standard deviations of E-type priors; (c) E-type summary of 100 simulation; (d) conditional standard deviations of 100 simulations. Note the *logarithmic color scale runs from 0.1 to **100*** for this case only.

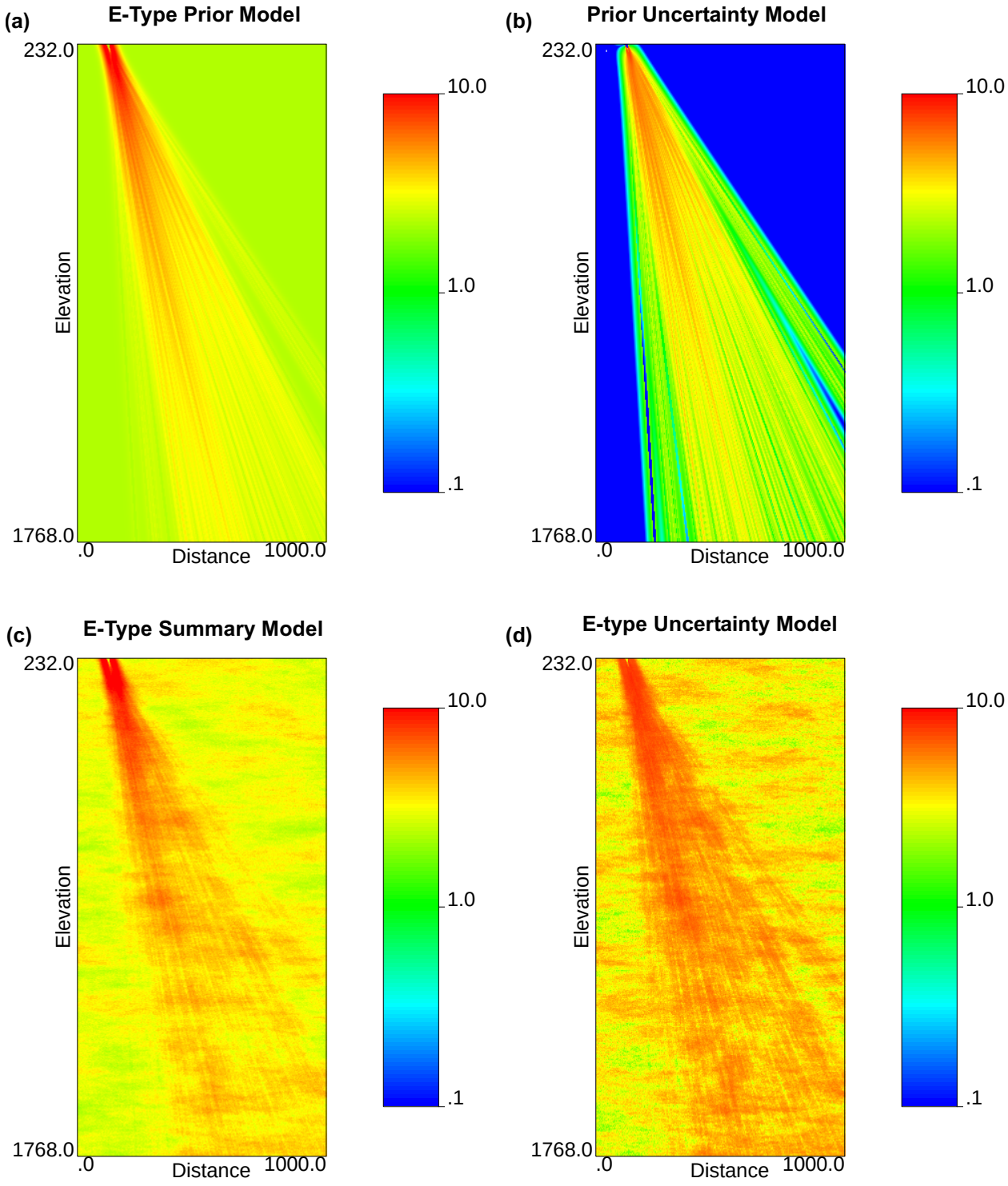

Figure 25. Comparison of prior fracture-frequency model with summary E-type model and conditional standard deviation model for pre-drilling Case No. 0a (with lower background fracture-frequency prior). (a) E-type model of fault priors; (b) conditional standard deviations of E-type priors; (c) E-type summary of 100 simulation; (d) conditional standard deviations of 100 simulations.Note that the *logarithmic* color scale runs only from 0.1 to 10 (compare with figure 24).

Case 1 (Drilling Sequences 1, 2, and 3)

Figure 26 stands in marked contrast to the pre-drilling situation of Cases 0 or 0a. Although Case 1 contains only one drill hole, MIU-3, this drill hole is strategically located and provides very precise control on the spatial location of the Tsukiyoshi Fault. Although the precise position of the center of the fault may be uncertain within a few meters, on the scale of the model domain (2000 m vertically), the position of the fault is deterministic. This deterministic prior model is presented in part (a) of figure 26. The low-fracture-intensity core of the fault zone is clearly indicated and of constant width throughout the vertical extent of the fault. The high-frequency margin of the fault where fracture intensity is high is clearly delineated, and although it is visually evident in detail on the figure only against the low-background fracture frequency of layered zone 1 (the upper zone), the progressive decay of fracture intensity with distance from the fault trace is preserved following the conceptual model of figure 18. As the prior frequency model is deterministic for Case 1 (and for Cases 2 through 7 that follow), there is no uncertainty model associated with the fault prior.

The two images in the lower half of figure 26 present the post-simulation model of both expected fracture frequency in the subsurface and of the uncertainty in that expected model. The position of the drill hole, MIU-3, is clearly indicated, particularly in the uncertainty model [part (c)], as the uncertainty in fracture frequency decreases to exactly zero at the location of the conditioning data (recall step 3 of the sequential Gaussian simulation process on page 23).

The specific fracture frequencies associated with the Tsukiyoshi Fault have been modified in part (b) somewhat by the conditioning data from borehole MIU-3, as expected. The prior model of the fault in part (a) represents a *conceptual* model only, and it appears desirable, when hard data are available to modify that conceptual model in a specific location, that those hard data would receive precedence.

Note, however, that whereas the very low fracture-frequency interval at a depth of approximately –480 m in drill hole MIU-3 (see down-hole data plot in figure 9) is presumably associated with the "dead" zone of the fault core, the geostatistical modeling algorithm, combined with the anisotropy ratio specified for the variogram model, has extended that low fracture intensity interval horizontally on both sides of the fault. If our understanding of the origin of the observed low fracture zone in drill hole MIU-3 is correct, this modeling is potentially in error, and the large subhorizontal blue-to-greenish region in figure 26(b) misrepresents the actual in-situ conditions (which are, of course, unknown in fact).

A portion of this potential modeling inaccuracy may be attributable to the specific geostatistical algorithm selected for this modeling exercise. We used sequential Gaussian simulation, in which the spatial continuity patterns of the entire range of fracture frequency values, low, medium, and high, is specified through use of a single variogram model. Had we chosen to model using, say, sequential ***indicator*** simulation, and had developed a separate indicator variogram model for high, medium, and low fracture intensities, our variogram model *might* have specified that the intense fracture frequencies exhibit a short range of correlation (compared to, say, low frequencies), or that the range of greatest spatial correlation of the high frequency values was oriented vertically in contrast to a horizontal orientation for the lower values. Indicator simulation is

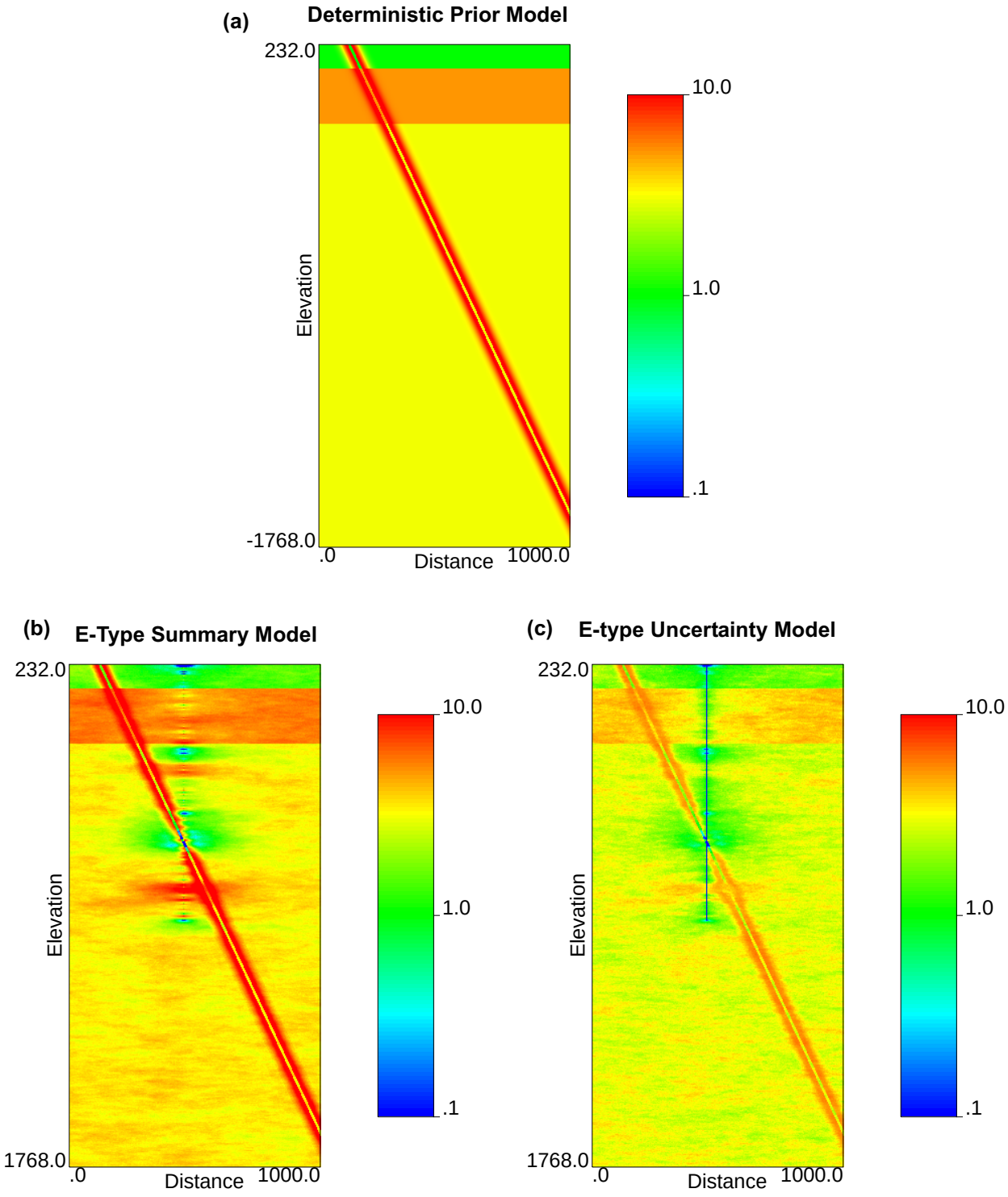

Figure 26. Comparison of prior fracture-frequency model with summary E-type model and conditional standard deviation model for Case No. 1. (a) Deterministic fault-prior model; (b) E-type summary of 100 simulations; (c) conditional standard deviations of 100 simulations. Color scale is logarithmic between 0.1 and 10 fractures per meter.

very powerful for capturing geologic features that may be expressed in differing magnitudes of the data values under consideration. However, inference of the required indicator variograms requires correspondingly more actual data. In the current instance, we were severely limited in our modeling of the range of spatial correlation in the horizontal dimension by the existence of only a single drill hole for Case 1. Developing a set of indicator variograms based on other than pure assumption in the present case would have been virtually impossible.

Also of note in part (c) of figure 26 is the spatial heterogeneity of uncertainty associated with the various fracture zones that were defined in the prior model. We note that the magnitude of the conditional standard deviations is somewhat proportional to the magnitude of the prior frequency estimates; this condition is known as ***heteroscedasticity*** (literally, unequal variances). For example, compare the magnitudes of the standard deviations in part (c) with the vertically zoned expected frequency values in part (b), particularly for zone 2. Note also that some horizontal layering is preserved even in the deepest parts of the model where there are no conditioning data to induce such layering. Presumably this relict layering would diminish in intensity with the addition of more simulations to the computation of the E-type model.

Case 2 (Drilling Sequence 1)

Figure 27 presents the summary modeling images for Case 2, which includes drill holes MIU-3 and MIU-2. The prior fracture-frequency model for this case is deterministic, as the position of the fault is precisely constrained by borehole MIU-3.

The E-type fracture frequency model of part (b) of figure 27 exhibits some marked differences from the expectation model shown in figure 26. Specifically, the apparent horizontal correlation, or extent of the intervals with lower fracture frequencies than the general background frequency, is noticeably shorter. There are two reasons for this change. First, the horizontal-to-vertical anisotropy ratio was decreased for Case 2 from 5:1 to 2:1 (table 8). Second, there appears to be somewhat of a lateral conflict between the conditioning data for the two drill holes.

This latter cause is most evident in the portions of the two drill holes, which are identifiable as the vertical strings of essentially zero uncertainty values in part (c) of the figure, immediately below the lower contact of prior-fracture-frequency zone 2. On part (b) of figure 27, the leftmost drill hole (MIU-3) contains a downward sequence of low values underlain by high values: green over red. In contrast, the rightmost drill hole (MIU-2) contains a sequence of observed fracture frequencies that are almost exactly inverted: orange-red (high) over green (low). This close (horizontal) juxtapositioning of different values affects the model both in a statistical sense through our inference of smaller anisotropy ratio for the variogram and directly through the influence of the conditioning data values.

Otherwise, the model of Case 2 resembles that of Case 1 fairly closely. The fault at positions away from the locations of the two drill holes is essentially identical, as should be the case for a single-valued (deterministic) fault prior. Heteroscedasticity of the conditional standard deviations is still evident, although the sphere of influence of the two drill holes is larger in Case 2 than in Case 1 [parts (c) of the two figures].

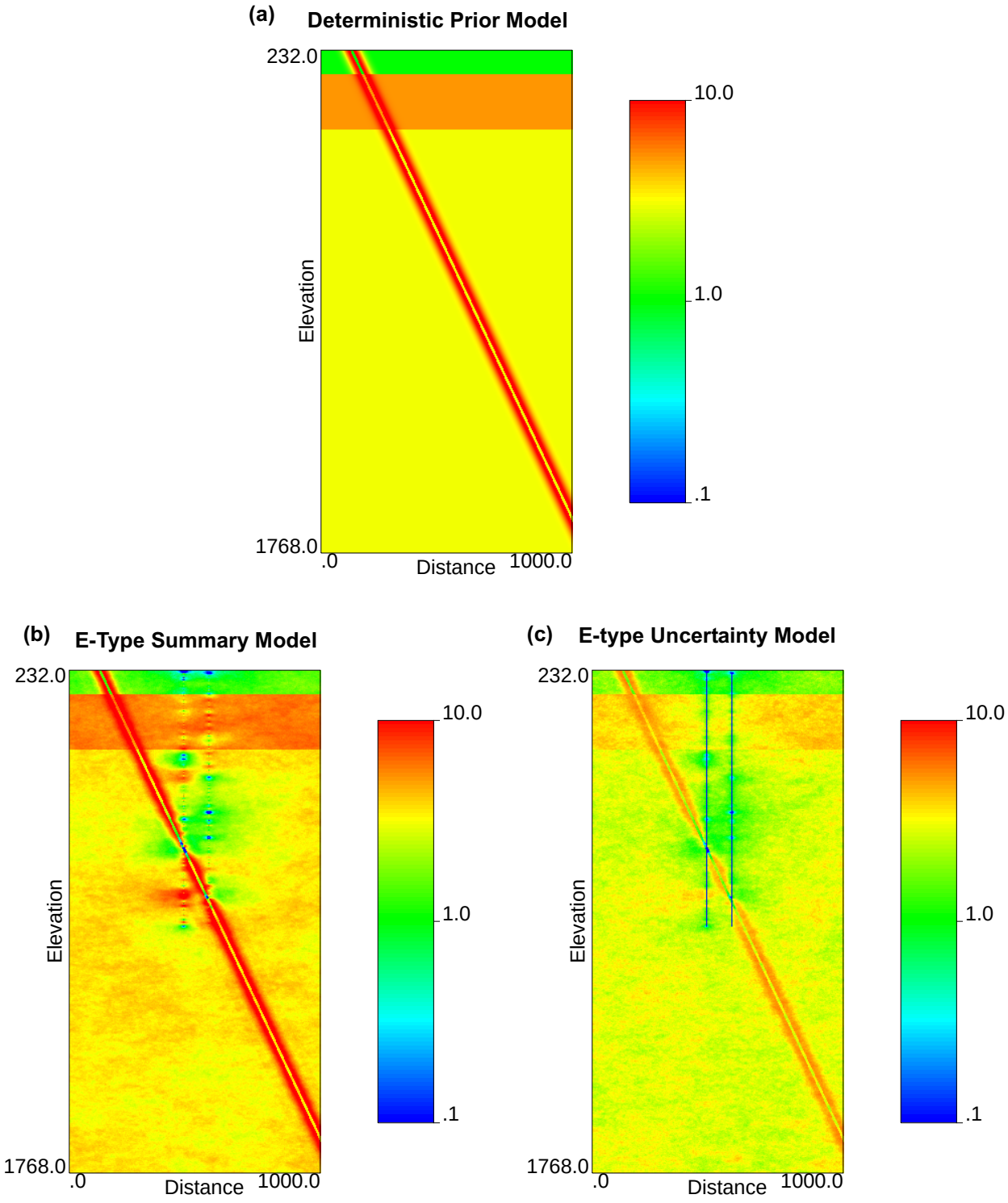

Figure 27. Comparison of prior fracture-frequency model with summary E-type model and conditional standard deviation model for Case No. 2. (a) Deterministic fault-prior model; (b) E-type summary of 100 simulations; (c) conditional standard deviations of 100 simulations. Color scale is logarithmic between 0.1 and 10 fractures per meter.

Case 3 (Drilling Sequence 1)

Figure 28 continues the progressive addition of information to Drilling Sequence 1 via the "drilling" of borehole MIU-1. Although the prior model of fracture frequency is still deterministic, set by the first drill hole of the sequence, MIU-3, the addition of the new drill hole to the right (south) of the first two changes both the E-type model of fracture frequency [part (b)] and the uncertainty model, as reflected in the conditional standard deviations of part (c).

The impact of the conditioning data from the third drill holes is evident in the E-type model. Interestingly, examples of both consistency of fracture intensity (at a given elevation) with the earlier drilled holes and inconsistency can be identified (compare the vertical distributions of red- vs. green-colored pixels between pairs of drill holes). That the information underlying this observation is present was suggested by the shortening of the modeled variogram ranges discussed previously (table 8). The impact of the conditioning data from the third drill hole is also evident in the larger region of green-toned pixels, representing smaller conditional standard deviations over a broader region, in figure 28(c), compared with parts (c) of the figures associated with earlier case of this drilling sequence.

Case 4 (Drilling Sequences 1, 2, 3, and 4)

Case 4 represents the culmination of all four hypothetical drilling sequences. The summary images for this case are presented in figure 29. As constrained by the presence of drill hole MIU-3 in this case (in all sequences), the fault prior is deterministic and not subject to uncertainty. Although this is not a change for Drilling Sequences 1, 2, or 3, it is a marked change for Drilling Sequence 4, for which, prior to drilling of borehole MIU-3, all fault priors were stochastic, although with decreasing uncertainty on the dip of the Tsukiyoshi Fault as drilling "progressed."

The summary E-type model and its associated uncertainty representation for Case 4 are presented in parts (b) and (c) of figure 29. Perhaps the most critical thing to observe in both of these images, is that the impact of the conditioning data has propagated essentially throughout the upper right quadrant of the model. Although there is evidence that the prior fracture-frequency model still influences the center of the region between drill holes AN-1 (rightmost drill hole) and MIU-1 (second from the right), the prior expectation throughout most of the upper right portion of the model domain has been significantly modified by location-specific information.

In distinct contrast to the upper-right-hand portion of the model, the lower half of the model domain, below the level of the roughly 1000-m boreholes, is essentially identical in all the cases in all drilling sequences. The upper-left-hand side of the model, generally but not exclusively below the (now deterministic) fault trace, is also essentially unmodified from the prior. This lack of change from the relevant prior models is completely understandable, from an information perspective. No data with a sufficient range of spatial influence have been added to these portions of the modeled domain. Having no information to the contrary, it is not surprising that our prior estimate of the fracture frequency in these regions is essentially unmodified.

Changes in the conditional standard deviations, as shown in the image of part (c) of figure 29, are consistent with this principal of relevant information addition or lack thereof. Much of the

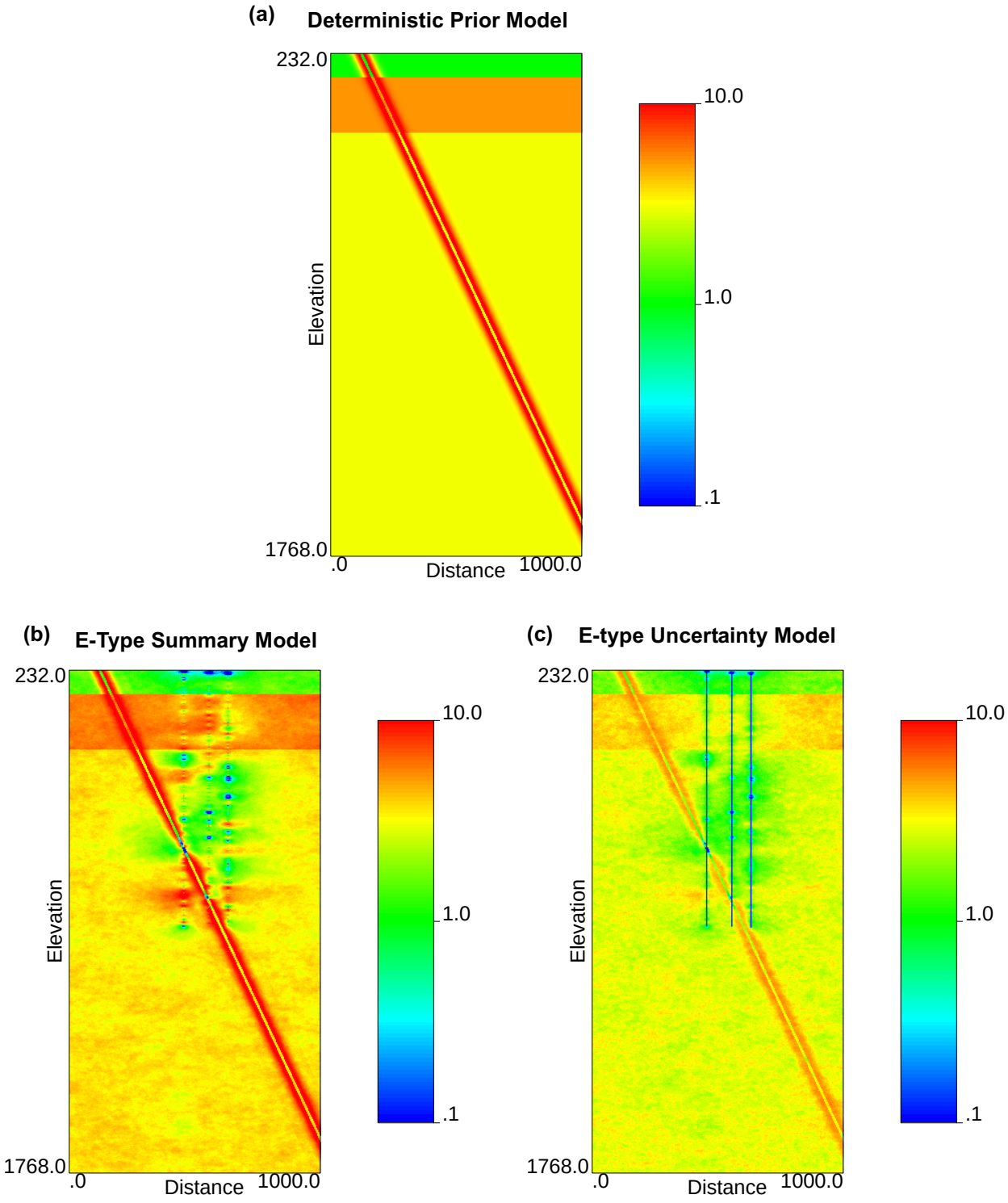

Figure 28. Comparison of prior fracture-frequency model with summary E-type model and conditional standard deviation model for Case No. 3. (a) Deterministic fault-prior model; (b) E-type summary of 100 simulations; (c) conditional standard deviations of 100 simulations. Color scale is logarithmic between 0.1 and 10 fractures per meter.

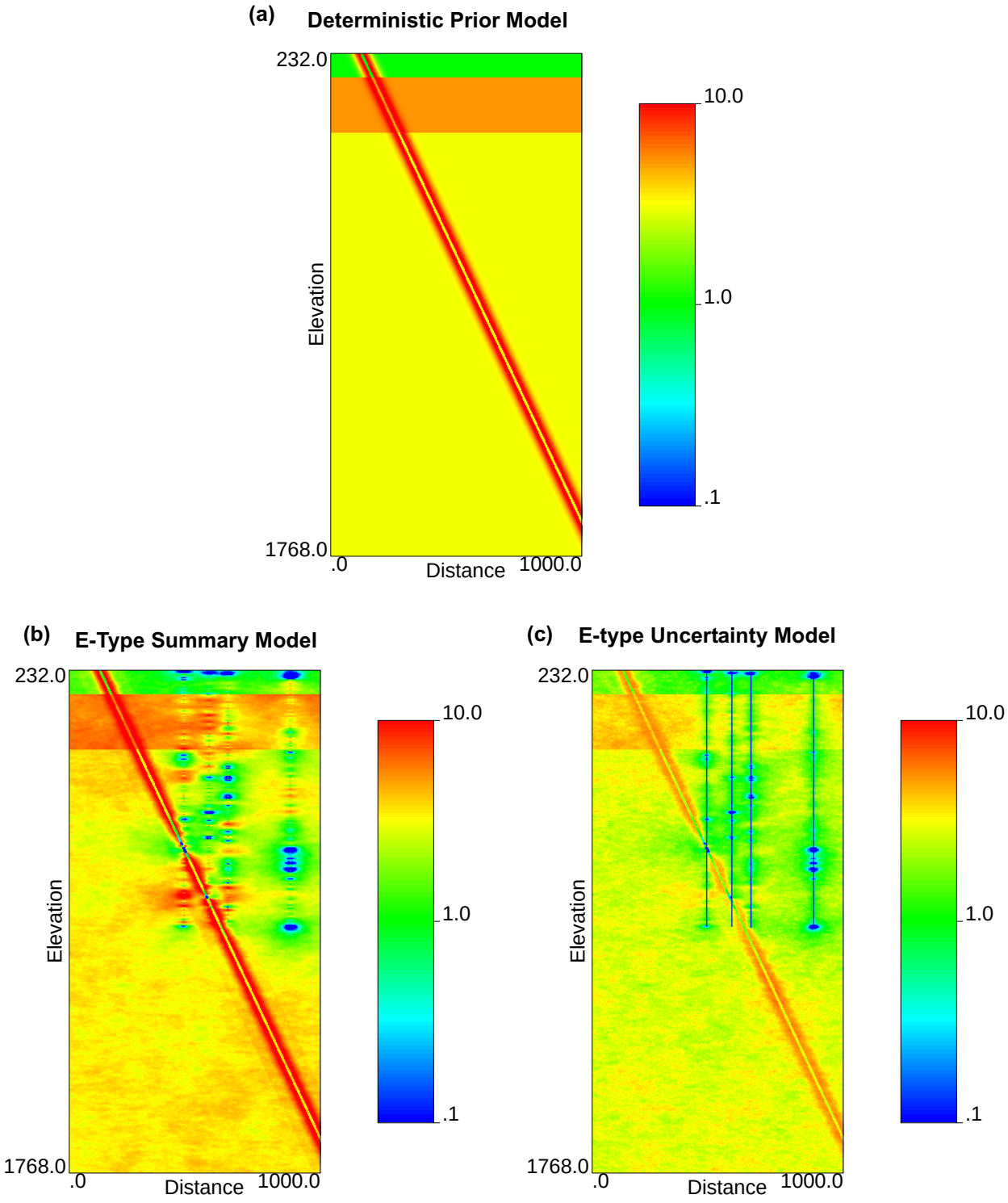

Figure 29. Comparison of prior fracture-frequency model with summary E-type model and conditional standard deviation model for Case No. 4. (a) Deterministic fault-prior model; (b) E-type summary of 100 simulations; (c) conditional standard deviations of 100 simulations. Color scale is logarithmic between 0.1 and 10 fractures per meter.

upper-right portion of the model domain in the vicinity of the four drill holes is indicated has having markedly lower uncertainty values than elsewhere in the domain.

Case 5 (Drilling Sequences 2 and 3)

Drilling Sequences 2 and 3 both commence with the pre-drilling Case 0 (figure 24; or Case 0a, figure 25), and continue with the drilling of borehole MIU-3, presented as Case 1, above (figure 26). Case 5 represents addition of a second drill hole to both sequences, and the summary images for fault-prior model, E-type model, and conditional uncertainty model are presented in figure 30. The fault-prior fracture-frequency model for this case is deterministic.

Figure 30 and Case 5 provide a good example of "a little something going a long way." Only one additional drill hole (AN-1) has been added to the modeling information set of Case 1. However, the impact of this additional data is relatively profound — at least within the portion of the model containing the two drill holes, and given the pre-drilling assumption of a 5:1 horizontal-to-vertical anisotropy ratio. The impact of the second drill hole in producing such pronounced layering would probably have been somewhat less, had the initial (Case 0) assumption of significant anisotropy been absent.

As indicated by the E-type summary model of figure 30(b), the existence of horizontal layering inferred from the first drill hole in this sequence in Case 1, is confirmed, and the prior model of part (a) is extensively modified throughout the upper-right-hand portion of the model domain. In addition to the very pronounced change in the spatially variable expected fracture frequency in part (b) of the figure, the uncertainty associated with that expected fracture frequency distribution appears relatively low as well. Much of the upper right hand portion of figure 30(c) is colored with green pixels, indicating low uncertainty compared with the unconditioned portions of the model domain, exemplified by the portion below drill hole depth. The uncertainty associated with the part of the model occupied by prior fracture-frequency zone 2 in the upper part of the model domain is also much reduced over the unconditioned portion of that same horizon on the extreme left-hand side.

This reduction of uncertainty throughout the portion of the model containing the two drill holes is consistent with (a) the wide drill hole spacing and (b) the variogram model that was inferred for Case 5, as illustrated in figure 22(e) and tabulated in table 8. The range of spatial correlation identified in the variogram is quite long; indeed, the maximum range of correlation for this case as given in table 8 is the longest range of any of the many variograms used in this modeling study. Thus, we have a situation of widely spaced boreholes and a model of strong spatial correlation, particularly in the horizontal dimension, and the propagation of the existing data throughout a large portion of the model domain is entirely expected.

However, recall that the variogram inferred for Case 5 relied upon only the down-hole experimental variogram, and that the horizontal variogram range(s) were specified only through the assumption that there was a fairly significant horizontal-to-vertical anisotropy ratio. A suggestion of difficulties to come in this drilling sequence is present in figure 30(b), specifically near the bottom portion of both drill holes. In this region, a broad horizon of high fracture frequencies present in the footwall block and conditioned by the first borehole of the sequence (MIU-3), is

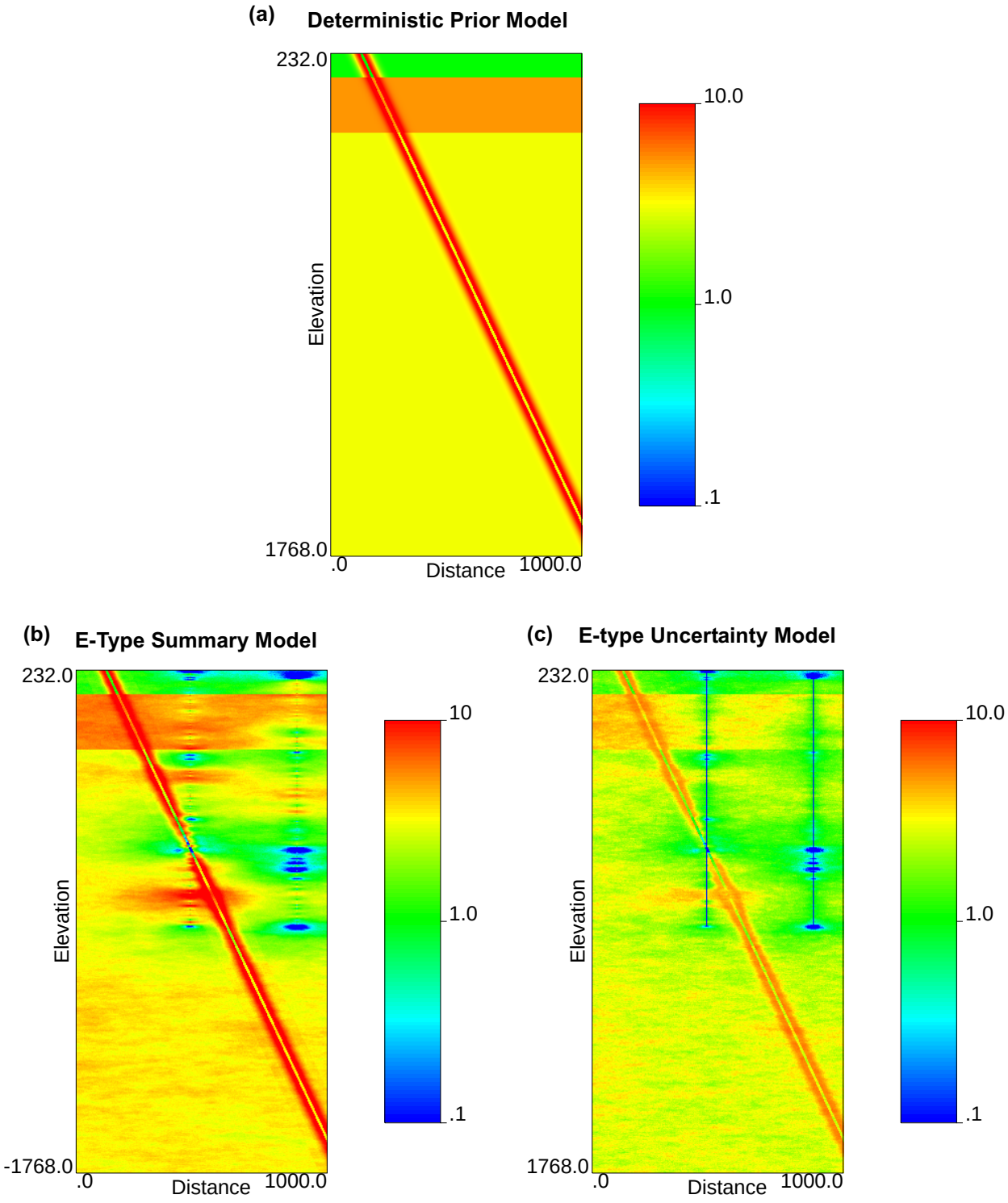

Figure 30. Comparison of prior fracture-frequency model with summary E-type model and conditional standard deviation model for Case No. 5. (a) Deterministic fault-prior model; (b) E-type summary of 100 simulations; (c) conditional standard deviations of 100 simulations. Color scale is logarithmic between 0.1 and 10 fractures per meter.

replaced laterally by a equally strong interval of only moderate fracture frequencies, conditioned by observed data in borehole AN-1. That this juxtaposition of differing fracture styles over a horizontal distance of some several hundred meters (figure 2) might represent a real feature could easily be discounted — at this stage in a real drilling campaign — by the fact that (a) the two portions of the discordant drill holes are in different structural blocks, and (b) that even if the relative displacements across the Tsukiyoshi Fault are not major, there is a suggestion of a more-or-less continuous low-frequency fractured interval below the discordant interval separated only by the high-frequency zone of the fault itself.

Case 6 (Drilling Sequence 2)

Case 6, and the summary images of figure 31, may be taken as the converse of the saying quoted in the first paragraph of the text describing Case 5, and as proof of the saying that "a little information may be a dangerous thing." Although the fault-prior model of fracture frequency is still deterministic and constrained by the first hole drilled as part of Drilling Sequence 2 (borehole MIU-3), the visual impression of the post-simulation E-type summary models portrayed in figures 30 and 31, parts (b), is quite different. The change is caused by the addition of drill hole MIU-1 to the composite data set, and more specifically by the change in the spatial correlation model represented by the presence of experimental points belonging to the horizontal variogram.

In contrast to figure 30(b), figure 31(b) indicates that the broad horizontal continuity of fracture frequency layering in Case 5 was incorrect. The color coding of pixels in close proximity to the three drill holes in Case 6 (figure 31) indicates significantly more juxtaposition of high and low frequency data than had been apparent earlier in this drilling sequence. This juxtaposition is the principal cause of the shorter-range variogram model fitted to the experimental variograms plots and recorded in table 8.

Interestingly enough, the visual impression derived from comparing figure 30(c) and figure 31(c) is that although the spatial location of the uncertain portions of the model may have moved around, it is not clear that the *overall* uncertainty associated with the data-constrained portion of the model (excluding the lower half and the far left-hand side) has changed all that much. The visual impression is that roughly the same quantity of green- to blue-colored pixels are present, and that those pixels have been relegated to positions intermediate between the two pairs of drill holes. We attempt to quantify this, and similar, impressions in a following section of this report dealing with *Summary Measures of Global Uncertainty*.

Case 7 (Drilling Sequence 3)

Case 7 represents the third increment of drilling for Drilling Sequence 3. Starting with the pre-drilling case (Case 0 or 0a), this sequence comprises Case 1 and Case 5 thus far, and it eventually culminates in Case 4. In this particular case, widely spaced drill holes MIU-3, which constrains the fault prior to the deterministic case, and AN-1 are interposed by borehole MIU-2, which is located quite close to the initial drill hole of the sequence. This is in contrast to the three-drill-hole Case 6 of Drilling Sequence 2, for which the spacing of the boreholes was subequal. Figure 32 presents the three summary images for Case 7.

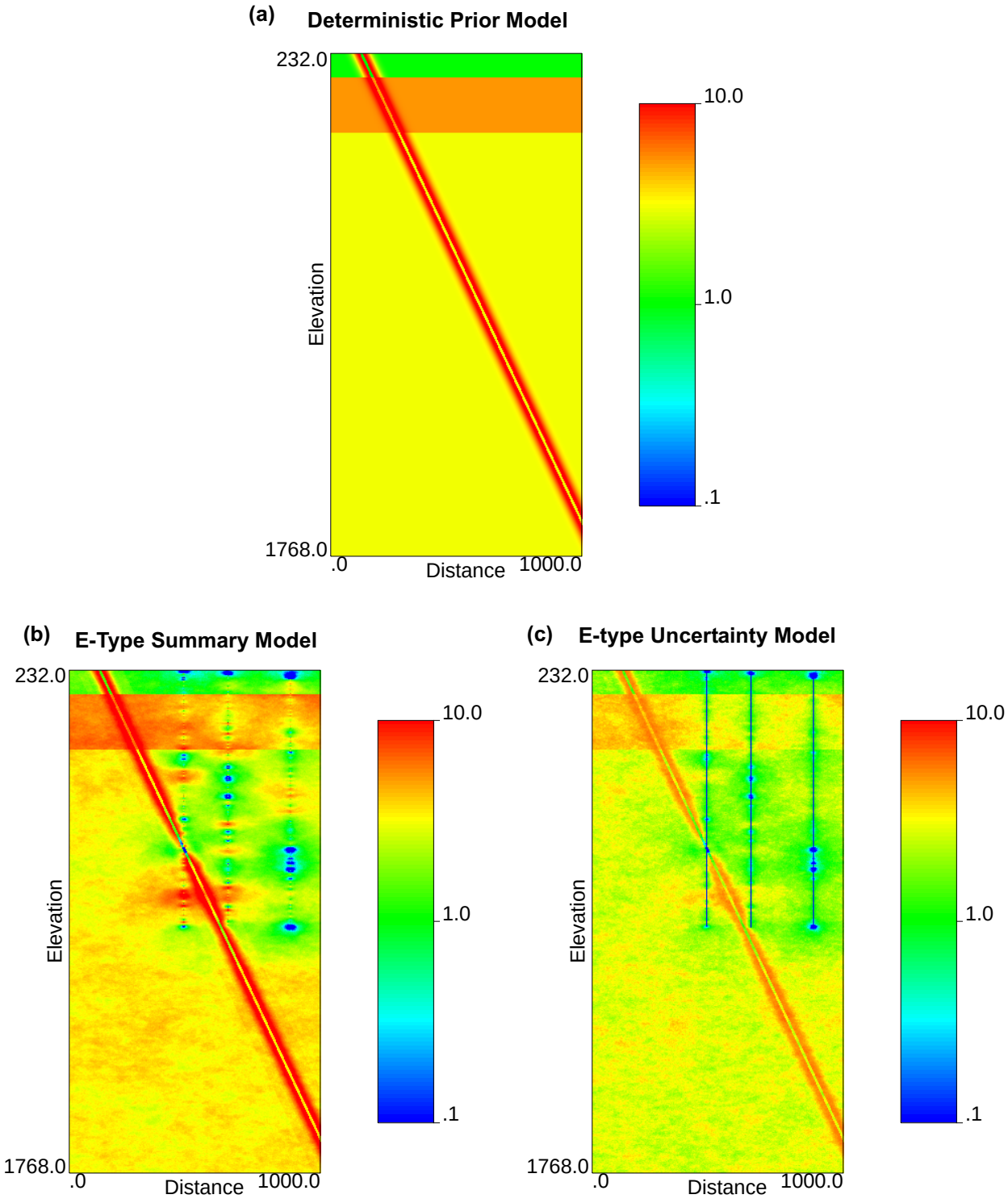

Figure 31. Comparison of prior fracture-frequency model with summary E-type model and conditional standard deviation model for Case No. 6. (a) Deterministic fault-prior model; (b) E-type summary of 100 simulations; (c) conditional standard deviations of 100 simulations. Color scale is logarithmic between 0.1 and 10 fractures per meter.

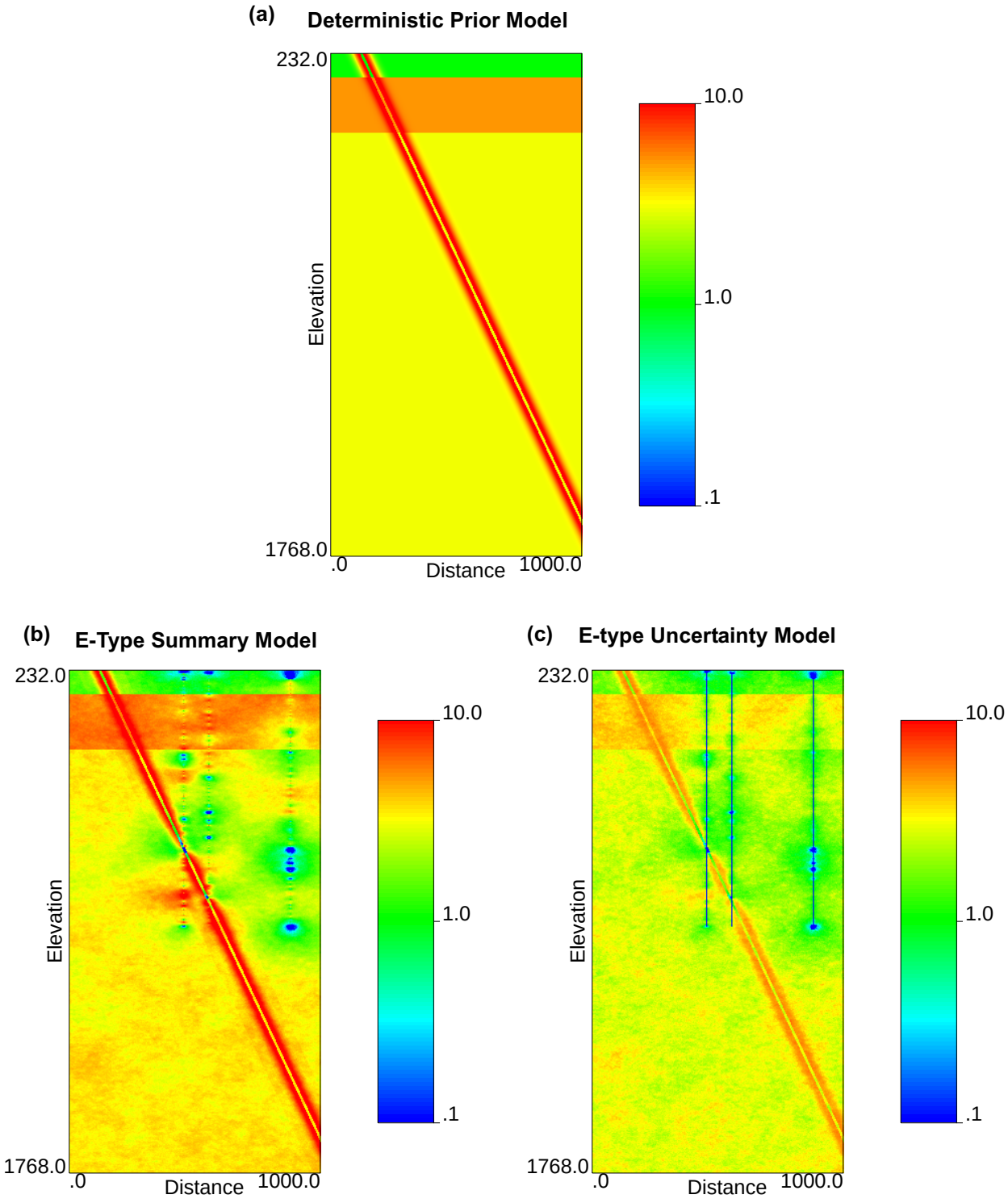

Figure 32. Comparison of prior fracture-frequency model with summary E-type model and conditional standard deviation model for Case No. 7. (a) Deterministic fault-prior model; (b) E-type summary of 100 simulations; (c) conditional standard deviations of 100 simulations. Color scale is logarithmic between 0.1 and 10 fractures per meter.

The net effect of adding borehole MIU-2 to the composite data set is similar to that of adding this drill hole to Drilling Sequence 1. The juxtaposition of high and low fracture frequency values in the data from drill holes MIU-3 and MIU-2 results in a pronounced reduction of the inferred range of spatial correlation; compare the variogram ranges given in table 8 for the two cases. As a consequence of both the decreased range of spatial continuity and of the conditioning data themselves, the horizontal layering of fracture frequency evident in the preceding case of both Drilling Sequences 1 and 3 is broken up and the spatial distribution of modeled fracture frequency becomes markedly more isotropic.

The difference is that for Drilling Sequence 1, it took only two boreholes to develop this (presumably) more accurate model of frequency (compared to Case 4 involving all four available drill holes), whereas for Drilling Sequence 3 (as well as for Sequence 2) it took three boreholes to acquire the same quantity of "information." In all three drilling sequences, however, the greatest problem is traceable directly to our pre-drilling assumption that there was horizontal-to-vertical anisotropy greater than 1 to 1. *This pre-drilling assumption turns out to be one of the most critical pieces of information in the entire modeling activity.*

Regardless of the geologic justification for this assumption in the pre-drilling case, it is propagation of the same assumption — with a lack of strong evidence to the contrary and a corresponding reluctance to abandon the assumption entirely — through successive cases involving more drill holes that led to the current situation. Only with effective refutation of the strong anisotropy assumption with addition of the third drill hole in Drilling Sequence 3 does the expected model of fracture frequency begin to converge on the "final" (albeit still uncertain) model of Case 4.

With respect to the uncertainty representation associated with the E-type model of Case 7 [part (c) of figure 32], it appears that overall uncertainty in the data-constrained upper-right-hand portion of the model domain may have increased in comparison to the corresponding image for Case 5 [figure 30(c)]. Note that this is in contrast to the visual impression of roughly subequal portions of high and low uncertainty obtained in the case of adding the third drill hole to Drilling Sequence 2 (Case 6). The difference between Case 6 and the present Case 7 is the spacing of the third hole relative to the two pre-existing drill holes. In the current case, drill hole MIU-2 is close enough to drill hole MIU-3 that the controlling influence of data from these two holes essentially merges, whereas the wide spacing between borehole AN-1 and MIU-2 is sufficiently large that the revised spatial continuity model does not sufficiently constrain the region located midway between this latter pair of holes.

Case 8 (Drilling Sequence 4)

Drilling Sequence 4 marks a significant departure from the patterns of modeling uncertainty identified in Sequences 1, 2 and 3. Rather than being in a deterministic situation with respect to the fault-prior model constrained by drill hole MIU-3, Drilling Sequence 4 involves stochastic fault-priors up until the concluding four-drill-hole Case 4. The *local* (in contrast to more global) uncertainty implications of this spatial uncertainty regarding the Tsukiyoshi Fault are profound.

Drilling Sequence 4 commences with the standard pre-drilling situation and the models of either Case 0 or Case 0a. Case 8 represents the addition of one drill hole, borehole AN-1, located at the far right-hand (south) side of the model domain. Figure 33 presents the summary images of the stochastic fault-prior models, the post-simulation E-type fracture frequency model, and the uncertainty model associated with the E-type model.

Because drill hole AN-1 is located sufficiently far from the outcrop of the Tsukiyoshi Fault that the fault was not intersected before drilling was terminated, the uncertainty associated with the dip of the fault is identical to that of the pre-drilling case. Even the total depth of the borehole imposes no new constraints on the dip of the fault. As described previously, simply insisting that the fault dip more steeply than implied by the total depth of the borehole provides for a greater variability than was determined to be geologically reasonable based on interpretation of the pre-drilling seismic refraction surveys.

The influence of the lack of constraints on the dip of the Tsukiyoshi Fault at depth in Case 8 is reflected throughout the four images of figure 33. However, for Case 8, in contrast to the pre-drilling case, there is direct evidence for the prior estimates of background fracture frequency in the subsurface. Regardless of the uncertainty regarding whether Case 0 or Case 0a is a better prior estimate of the state of fracturing at depth, the addition of drill hole AN-1 provides immediate and direct evidence of fracture frequencies in the subsurface. Note from figure 10 that the data set for Case 8 includes only two background fracturing zones in the prior fault models. The logic underlying this situation is that the surface elevation of drill hole AN-1 is lower than the surface elevations of the other drill holes. Background fracture zone 1 cannot be distinguished in this drill hole, and the background prior model is modified accordingly. The vertical extents of the remaining two background fracture frequency zones are markedly different for Case 8 than for any other case, regardless of drilling sequence.

As might be expected from the use of a stochastic fault prior, the spatial variations in both the E-type model of fracture frequency and the uncertainty model are substantial. Note that this spatial variability affects the entire vertical extent of the model domain, because — unlike the addition of only partially penetrating information via drill holes in Drilling Sequences 1, 2, and 3 — the uncertainty in the fault prior is pervasive throughout the domain as a consequence of the relatively steep dips (greater than 55 degrees), which “sweep” through virtually the entire extent of the model.

Note that the spatial distribution of uncertainty, as reflected in the conditional standard deviations associated with the E-type model, is distinctly bimodal. Higher uncertainty is associated with the uncertain positions of the stochastic fault across the 100 realizations modeled. Note also that the uncertainty values at locations *not* associated with the stochastic fault traces appear to be smaller than for the other drilling sequences considered. Also, the difference in uncertainty values between background fracture zones 2 and 3 is markedly reduced compared to the similar comparison for the other drilling sequences. Again, this decreased magnitude of uncertainty is related to the principle of heteroscedasticity, or of variances typically being proportional to the magnitude of the mean. The background fracture-frequency prior values implied by the data set from borehole AN-1 (table 6) are smaller than for other priors considered as part of this overall modeling exercise. Thus, the conditional standard deviations are smaller as well.

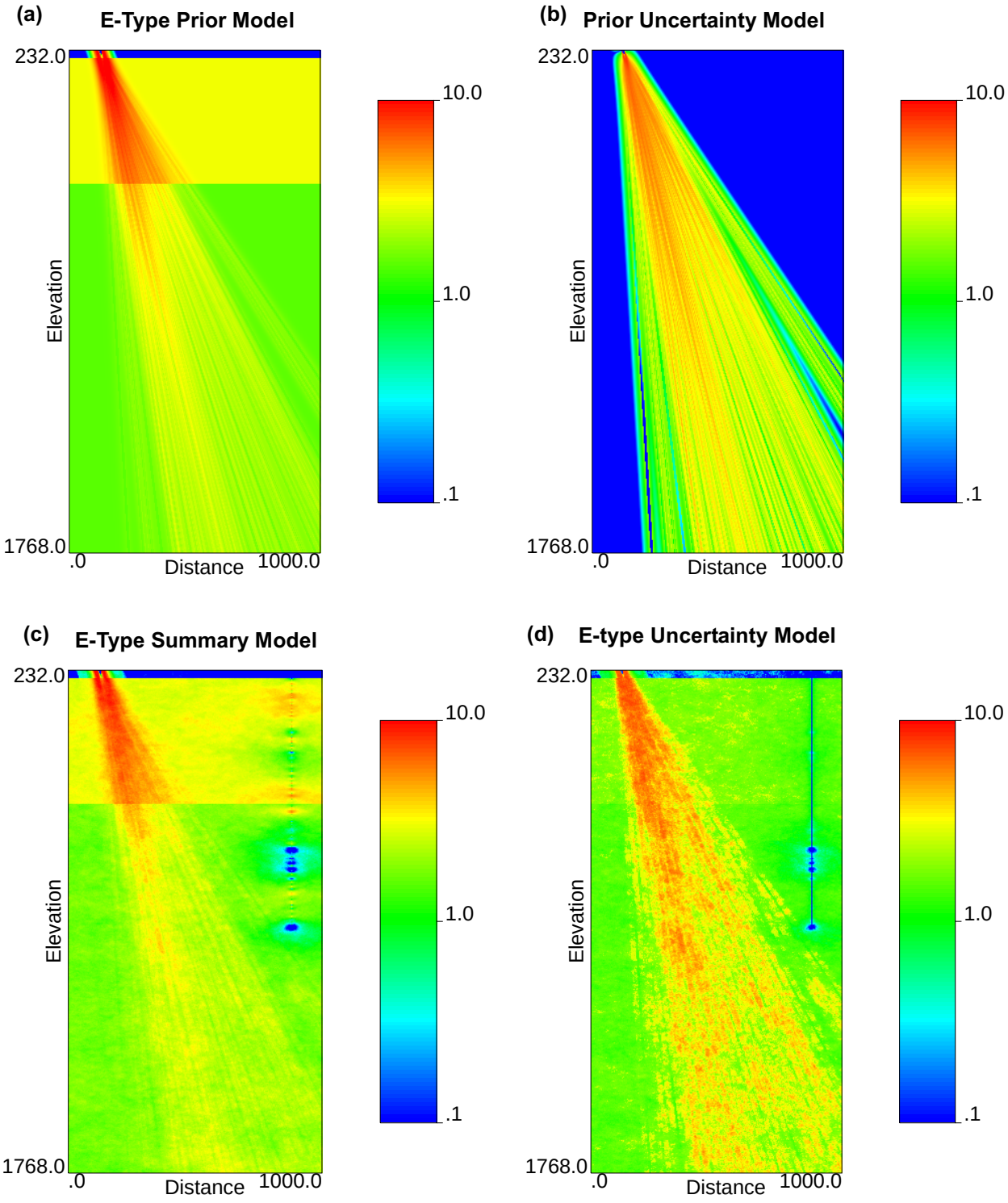

Figure 33. Comparison of prior fracture-frequency model with summary E-type model and conditional standard deviation model for Case No. 8. (a) E-type model of fault priors; (b) conditional standard deviations of E-type priors; (c) E-type summary of 100 simulation; (d) conditional standard deviations of 100 simulations. Color scale is logarithmic between 0.1 and 10 fractures per meter.

Case 9 (Drilling Sequence 4)

Case 9 represents the addition of a second drill hole to Drilling Sequence 4: borehole MIU-1. Drill hole MIU-1 also stopped short of intersecting the Tsukiyoshi Fault at depth, which results in the continued use of stochastic fault-prior models to capture this type of uncertainty. The standard summary images of the fault-prior model and the post-simulation E-type and uncertainty models are presented in figure 34.

However, the total depth of borehole MIU-1 *does* restrict the range of dips that may reasonably be associated with this stochastic modeling. As indicated in table 6, and as portrayed graphically in figure 16(b), the Tsukiyoshi Fault must dip more steeply than approximately 63 degrees (reduced from as shallow as 55 degrees). This constraint on both the fault prior and the E-type fracture frequency models is reflected in the various images of figure 34. Also note in figure 34 that the composite data set associated with the combination of drill holes AN-1 and MIU-1 supports a return to a three-zone background frequency model similar to that used in the other drilling sequences. The thicknesses of these three zones are also more consistent with those of the other drilling sequences (e.g., table 6).

Figure 34(c), the E-type model, clearly indicates the horizontal juxtaposition of high- and low-frequency intervals in the two drill holes, although the impact of this juxtaposition on the ranges of spatial correlation identified for the variograms [table 8; figures 23 (b) and (c)] is not all that significant because the modeled anisotropy ratios do not change very much in going from Case 8 to Case 9. In common with Case 8, the uncertainty induced by the stochastic fault pervades the entire model domain. The upward and rightward (southward) extent of that fault-related uncertainty is reduced, however, compared to Case 8, because of the constraint on the dip of the fault provided by drill hole MIU-1. Note that the heteroscedastic relationship between the background fracture-frequency prior values and the modeled uncertainty increases the average uncertainty levels throughout the portions of the model that are unconstrained by drill hole information or affected by the stochastic fault.

Cases 10 and 10a (Drilling Sequence 4)

Case 10 represents the addition of a third drill hole, MIU-2, to Drilling Sequence 4. In the baseline Case 10, the information provided by this third drill hole converts the fault prior to a deterministic situation identical to that involved in Cases 1 to 7. However, as described previously, the actual constraints on the subsurface location of the Tsukiyoshi Fault imposed by drill hole MIU-2 proper are permissive of a rather tightly constrained stochastic fault model, and we have constructed this alternate Case 10a as well. The constraints on the fault dip for Case 10a are summarized in table 7 and the same information is portrayed graphically in figure 16(c).

The modeling summary images associated with Cases 10 and 10a are presented in figures 35 and 36, respectively. Note that with the exception of the omission of a fault-prior conditional standard deviation image from figure 35, the differences between these two modeling cases are not particularly great. There is no uncertainty associated with the fault-prior model of Case 10. For stochastic Case 10a, the constraints imposed by the combination of drill holes MIU-2 and MIU-1 [figure 16(c)] induce a great deal of similarity between the two prior models. Notice, how-

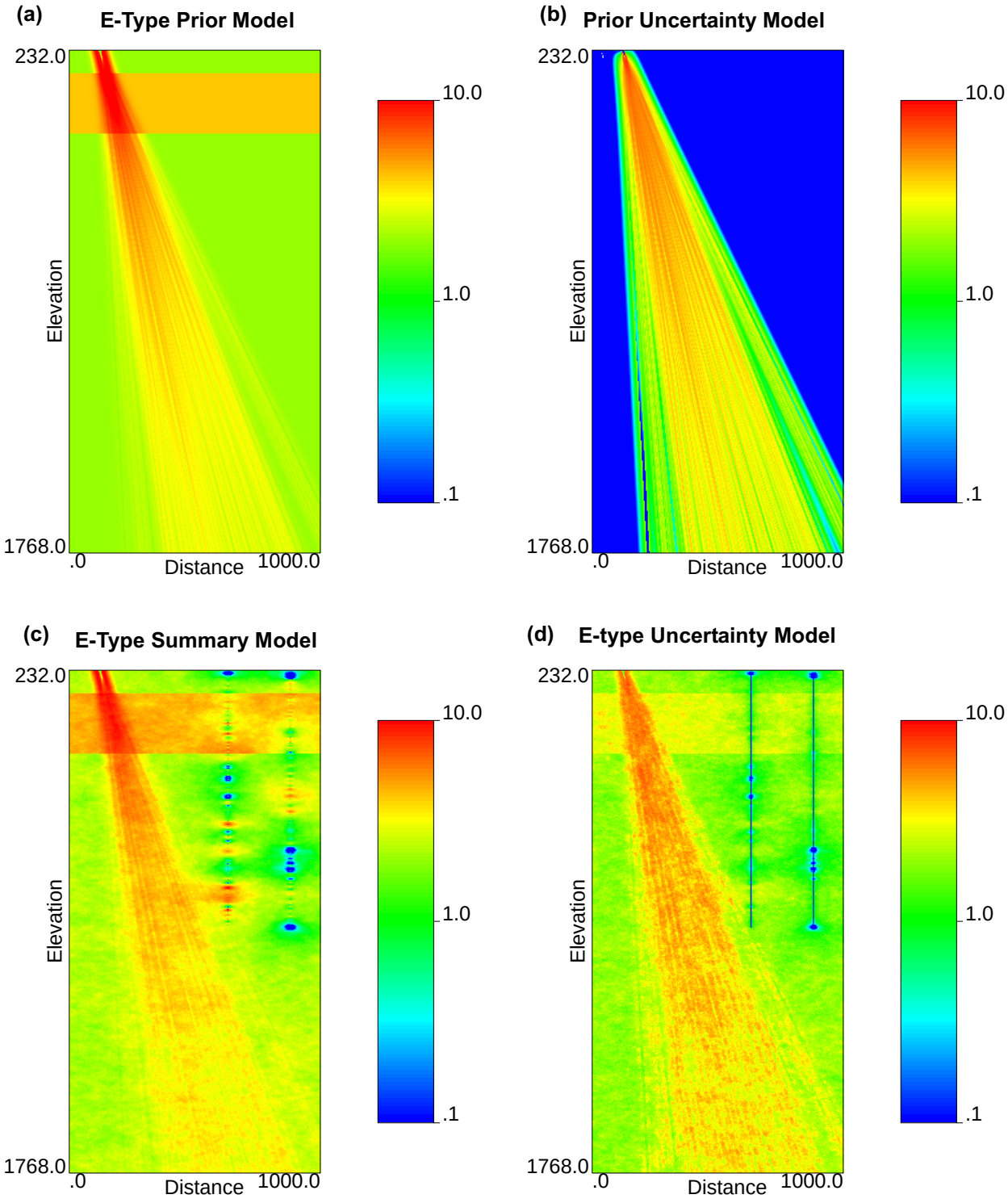

Figure 34. Comparison of prior fracture-frequency model with summary E-type model and conditional standard deviation model for Case No. 9. (a) E-type model of fault priors; (b) conditional standard deviations of E-type priors; (c) E-type summary of 100 simulation; (d) conditional standard deviations of 100 simulations. Color scale is logarithmic between 0.1 and 10 fractures per meter.

ever, that the low-fracture-frequency core of the Tsukiyoshi Fault is lost with increasing depth in E-type summary of the stochastic fault prior [figure 36(a)], whereas this low-frequency feature persists to depth in the single-valued (deterministic) model of the fault prior in figure 35(a).

With the exception of the fault-related fracturing, the post-simulation E-type models for Cases 10 and 10a are extremely similar. The horizontal juxtaposition of high- and low-frequency zones vertically in the different drill holes is identical, as it should be. The spatial distribution of uncertainty, as related to the specific three boreholes, is essentially identical as well, save for where drill hole MIU-2 (the left-hand-most borehole) penetrates the fault zone.

Alternate Case 8a (Drilling Sequence 4)

Development of alternate case 8a was almost an afterthought to the modeling that has been described previously. Unlike the other alternate cases originally described in table 4, Case 8a was not developed in response to some perceived inadequacy or uncertainty in the baseline case. Instead, the intent of Case 8a was simply to demonstrate the potential impact of geologically partitioning the model domain into two structural domains: hanging wall and footwall. As described in summary form in table 4, Case 8a was constructed using a uniform prior fracture frequency distribution below the fault in each of the individual, stochastically generated fault-prior models. The fracture frequency assigned to this footwall block was that of the area-weighted outcrop values located north of the outcrop of the Tsukiyoshi Fault summarized in table 5. The background fracture frequency assigned as a prior model for each individual hanging wall block was identical to that associated with Case 8 and is based on the single drill hole, borehole AN-1, that defines Case 8.

The four summary images for a stochastic fault-prior modeling case for Case 8a are presented in figure 37. Essentially, the four separate parts of figure 37 are a blend of figures 25 (Case 0a) and 33 (Case 8). Both of these models that are described above have individual fault models that are unconstrained by drill hole information and the general appearance of the two principal portions of the model are effectively identical. The differences are only subtly apparent upon close examination. Figure 37(a) suggests that the expected fault-prior fracture frequency in the lower portion of the regions affected by the “sweep” of the stochastic fault planes is different in detail from either Case 0 or the baseline Case 8. This subtle difference in the prior-estimated fracture frequency in this part of the image of figure 37(a) is propagated into the corresponding portion of figure 34(c), the post-simulation E-type model.

Although both the merging of the results for Cases 0a and the baseline Case 8, and the subtle blending of the two end-member cases in the regions of greatest uncertainty regarding the trace of the fault itself, are relatively intuitive, the desirability of modeling the hanging wall and the footwall structural blocks using separate prior information sets might make sense in certain instances were the fracture frequency models to be evaluated for their flow-and/or-transport consequences. That the styles of fracturing might differ in such different structural domains is not unexpected from a geological perspective.

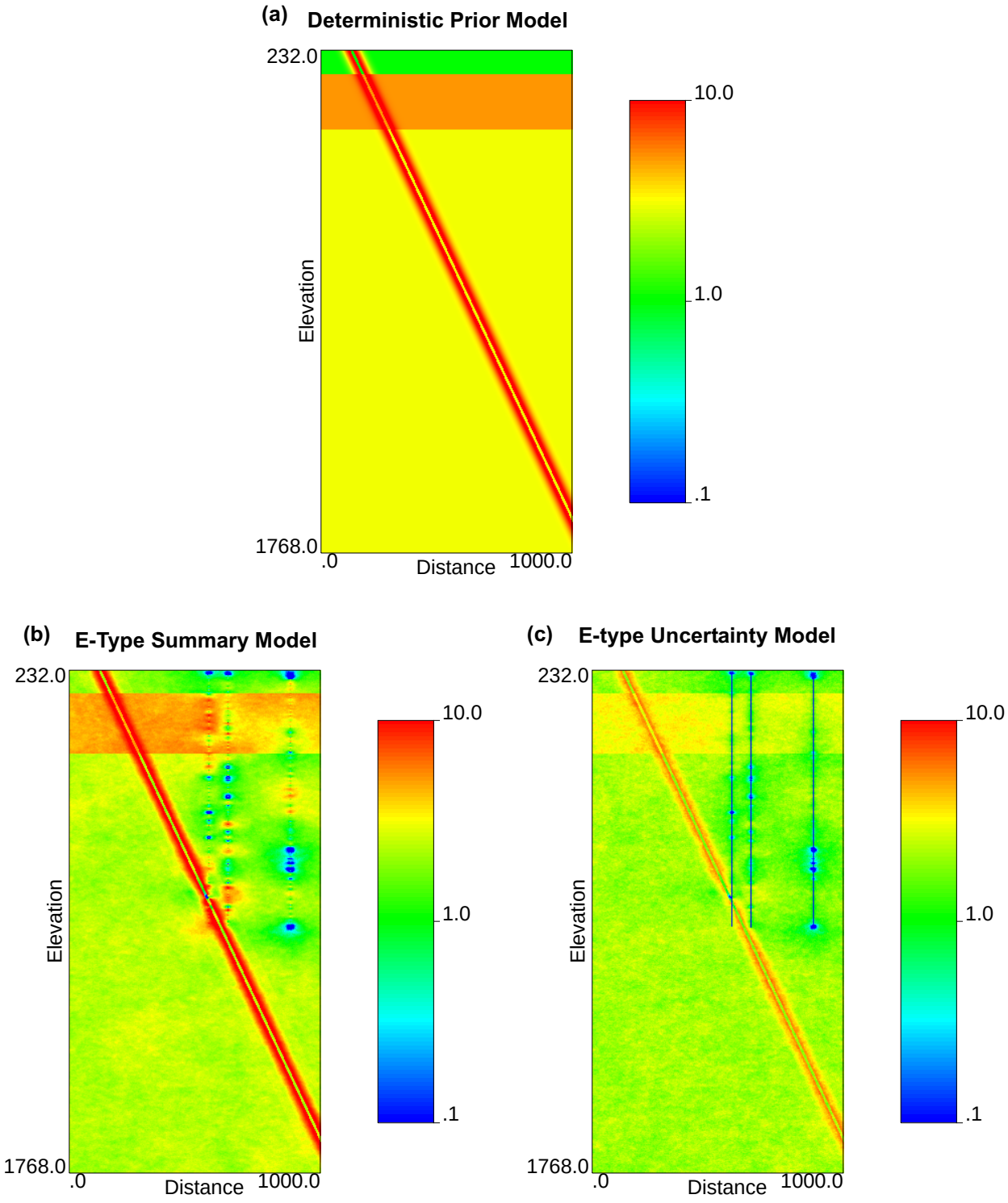

Figure 35. Comparison of prior fracture-frequency model with summary E-type model and conditional standard deviation model for Case No. 10. (a) Deterministic fault-prior model; (b) E-type summary of 100 simulations; (c) conditional standard deviations of 100 simulations. Color scale is logarithmic between 0.1 and 10 fractures per meter.

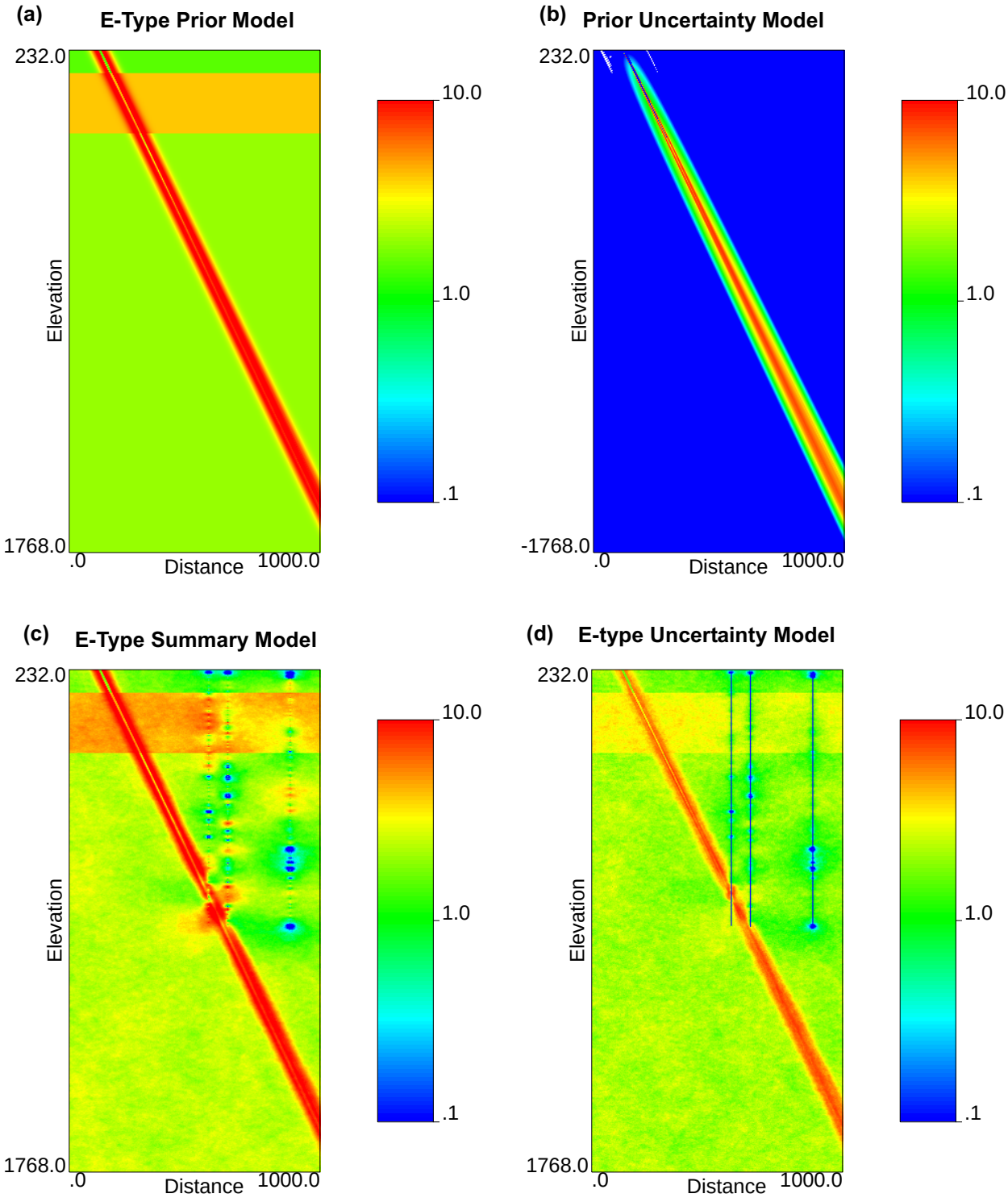

Figure 36. Comparison of prior fracture-frequency model with summary E-type model and conditional standard deviation model for Case No. 10a (with tightly constrained stochastic fault). (a) E-type model of fault priors; (b) conditional standard deviations of E-type priors; (c) E-type summary of 100 simulation; (d) conditional standard deviations of 100 simulations.Color scale is logarithmic between 0.1 and 10 fractures per meter.

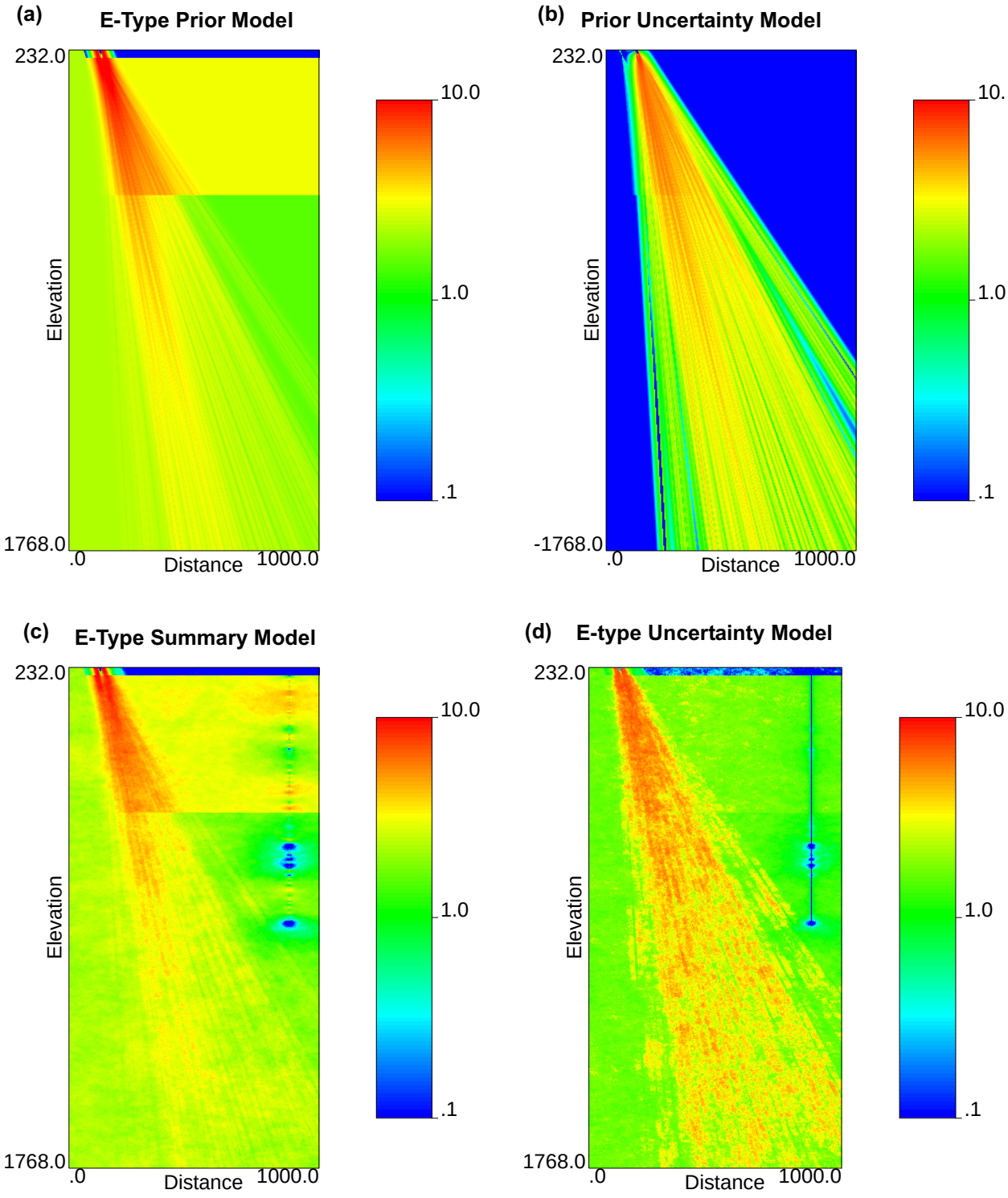

Figure 37. Comparison of prior fracture-frequency model with summary E-type model and conditional standard deviation model for Case No. 8a (with different fracture frequencies in the hanging wall and the footwall). (a) E-type model of fault priors; (b) conditional standard deviations of E-type priors; (c) E-type summary of 100 simulation; (d) conditional standard deviations of 100 simulations. Color scale is logarithmic between 0.1 and 10 fractures per meter.

Presentation of Modeling Results by Drilling Sequence

This section of the *Modeling Results* section takes the individual modeling cases that have been discussed in the immediately preceding section and presents both the post-simulation E-type models and their associated uncertainty portrayals as coherent drilling sequences. Two figures are given for each of the four drilling sequences defined in table 2. The first figure presents the E-type summary models showing the spatial variation in expected fracture frequency. The second figure presents the uncertainty models associated with each sequence. The drilling sequences begin with the pre-modeling situation (represented by Case 0a so that the color scales are uniform and scaled logarithmically between 0.1 and 10 fractures per meter), and proceed to add drill holes sequentially from left to right.

Summary of Drilling Sequence 1

Figure 38 presents the cases involved in Drilling Sequence 1: Case 0a, Case 1, Case 2, Case 3, and Case 4. The fault-prior model is deterministic, as indicated by intersection of the Tsukiyoshi Fault in the first drill hole of the sequence, MIU-3 in Case 1. The most evident change in the E-type frequency models of Drilling Sequence 1 are associated with the change from a stochastic fault-prior model with no fracture zonation in Case 0a to a deterministic fault-prior model in each of the data-based succeeding cases. Secondary changes in the expected fracture frequency models are related to the addition of the four drill holes in turn.

Figure 39 presents the same sequence of cases for Drilling Sequence 1, only the images are of the conditional standard deviations associated with the E-type models. Again, the most prominent change is the difference between the pre-drilling, stochastic-fault model of Case 0a and the deterministic fault-prior models of Cases 1 through 4. Spatial expansion of the lower-uncertainty regions directly associated with the borehole information is also evident.

Summary of Drilling Sequence 2

Figure 40 presents the expected fracture-frequency maps associated with Drilling Sequence 2. This sequence repeats Case 0a and Case 1, includes Cases 5 and 6, and culminates with Case 4. Again, the most prominent difference among the models is related to the unconstrained stochastic fault-prior model involved in the pre-drilling case and the deterministic fault model identified once the Tsukiyoshi Fault is penetrated at depth in borehole MIU-3 (Case 1). Other changes among Cases 1, 5, 6, and 4 are more incremental in nature, although the break-up of the extensive horizontal continuity of low frequencies between Cases 5 and 6 (as described on page 76) is fairly pronounced.

Figure 41 presents the uncertainty models that correspond to the images in figure 40. As expected, the major difference is between the fully stochastic pre-drilling case and the other, constrained deterministic cases. The marked visual increase and successive decrease in contiguous regions of low uncertainty between Case 5 and 6 is also apparent.

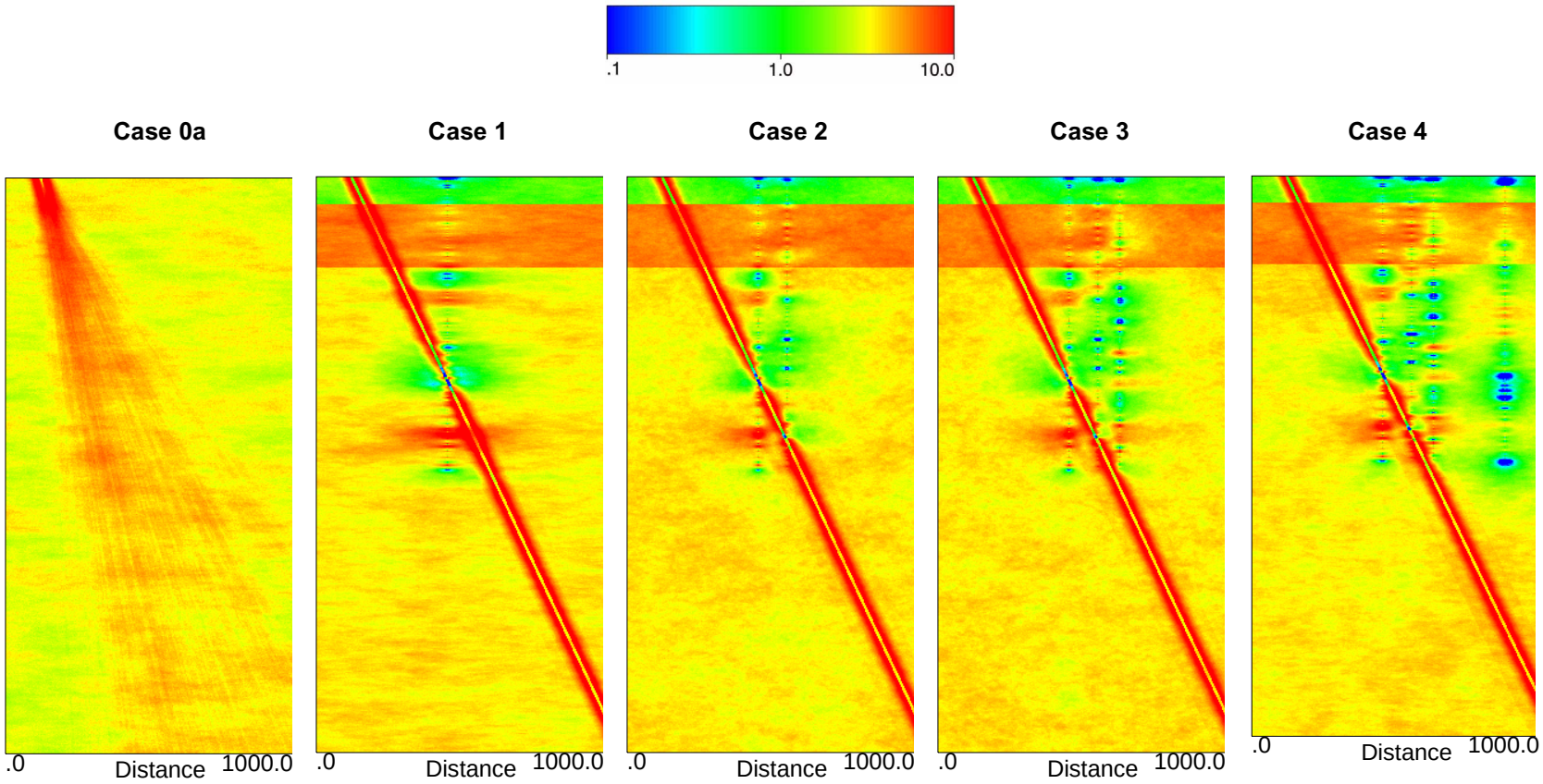

Figure 38. Comparison of E-type fracture-frequency models for Drilling Sequence No. 1 (Cases 0a, 1, 2, 3, and 4). Case 0 (pre-drilling) not shown. Color scale is logarithmic between 0.1 and 10 fractures per meter.

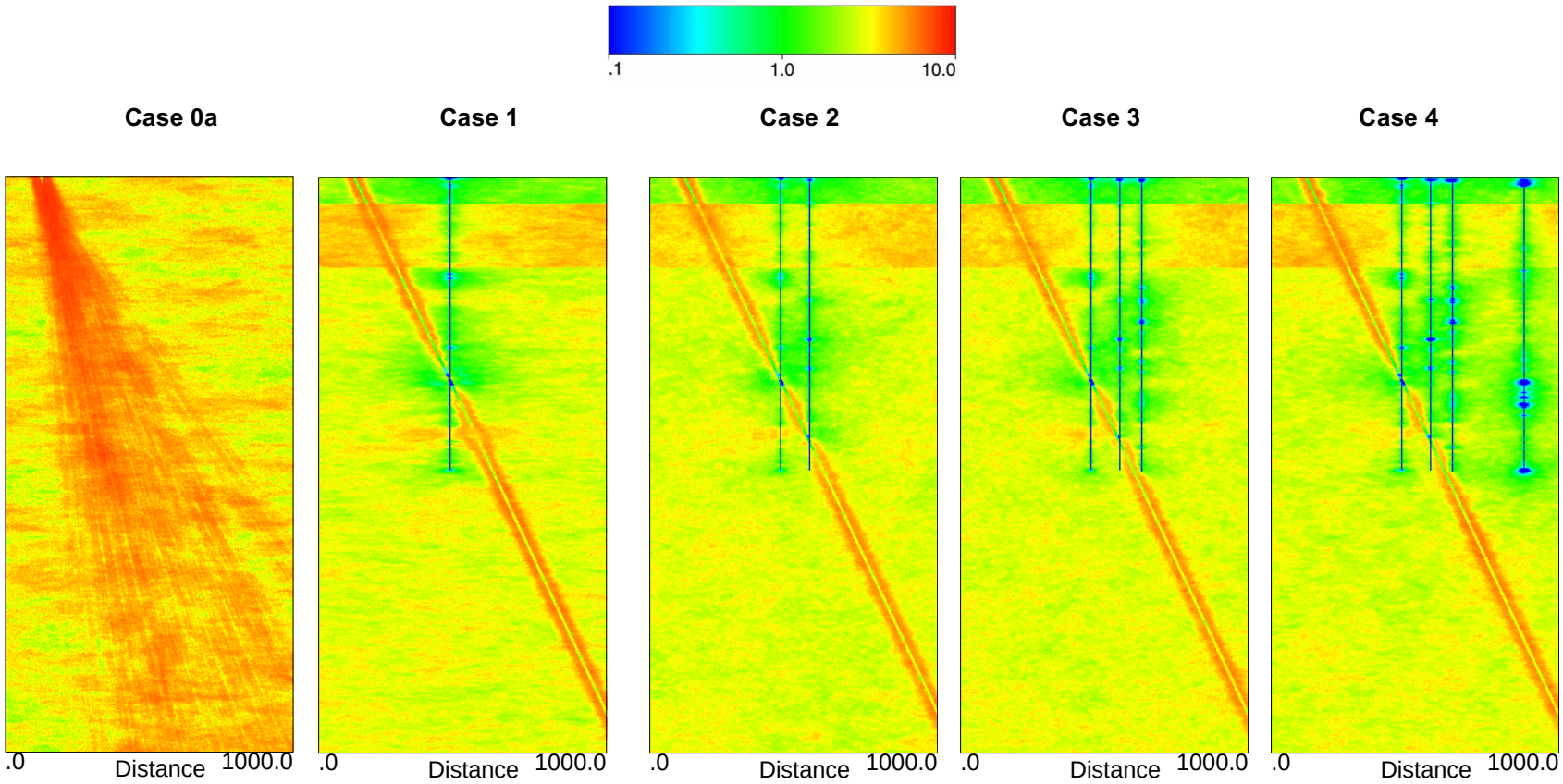

Figure 39. Comparison of fracture-frequency uncertainty models for Drilling Sequence No. 1 (Cases 0a, 1, 2, 3, and 4). Color scale is logarithmic between 0.1 and 10 fractures per meter.

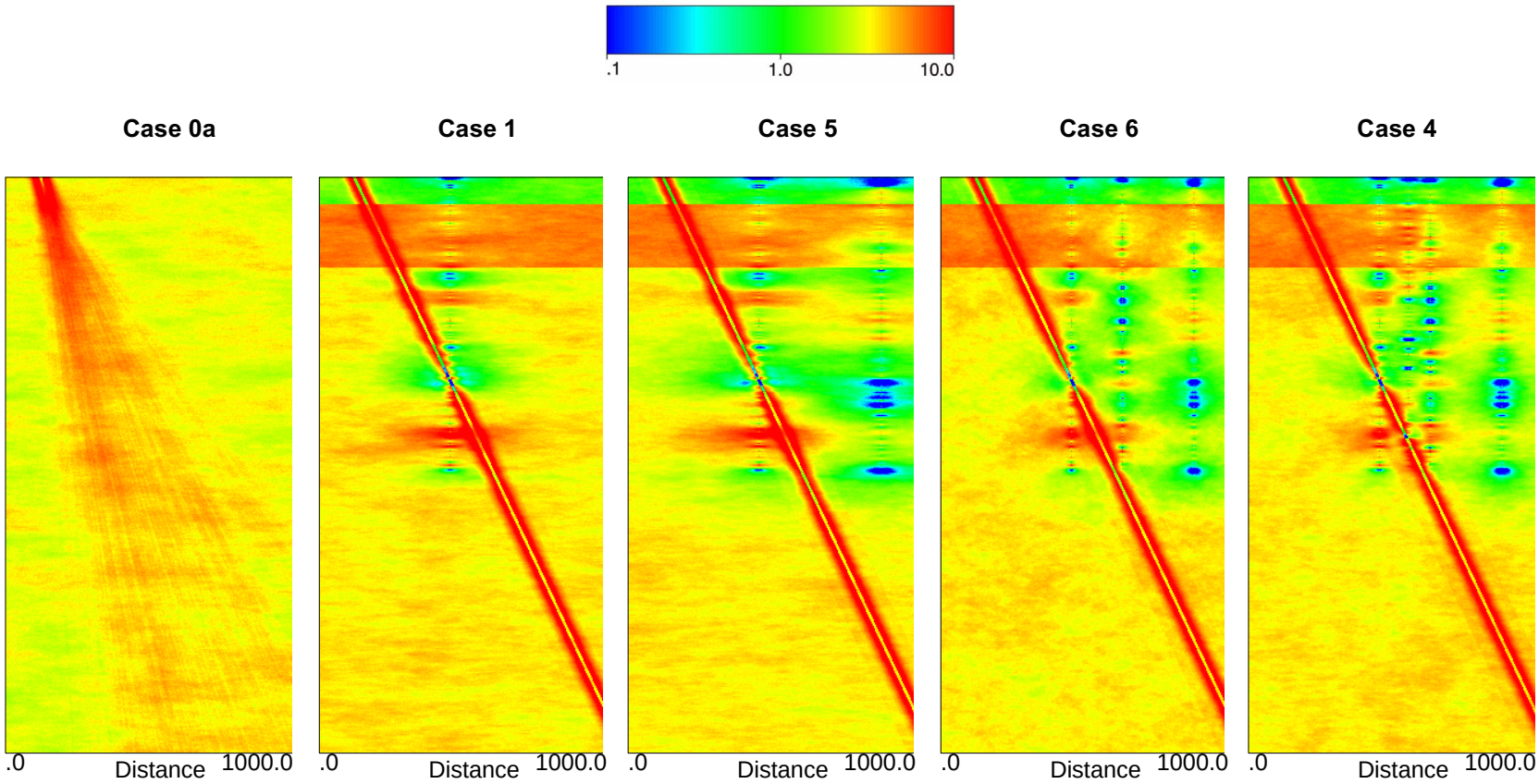

Figure 40. Comparison of E-type fracture-frequency models for Drilling Sequence No. 2 (Cases 0a, 1, 5, 6, and 4). Color scale is logarithmic between 0.1 and 10 fractures per meter.

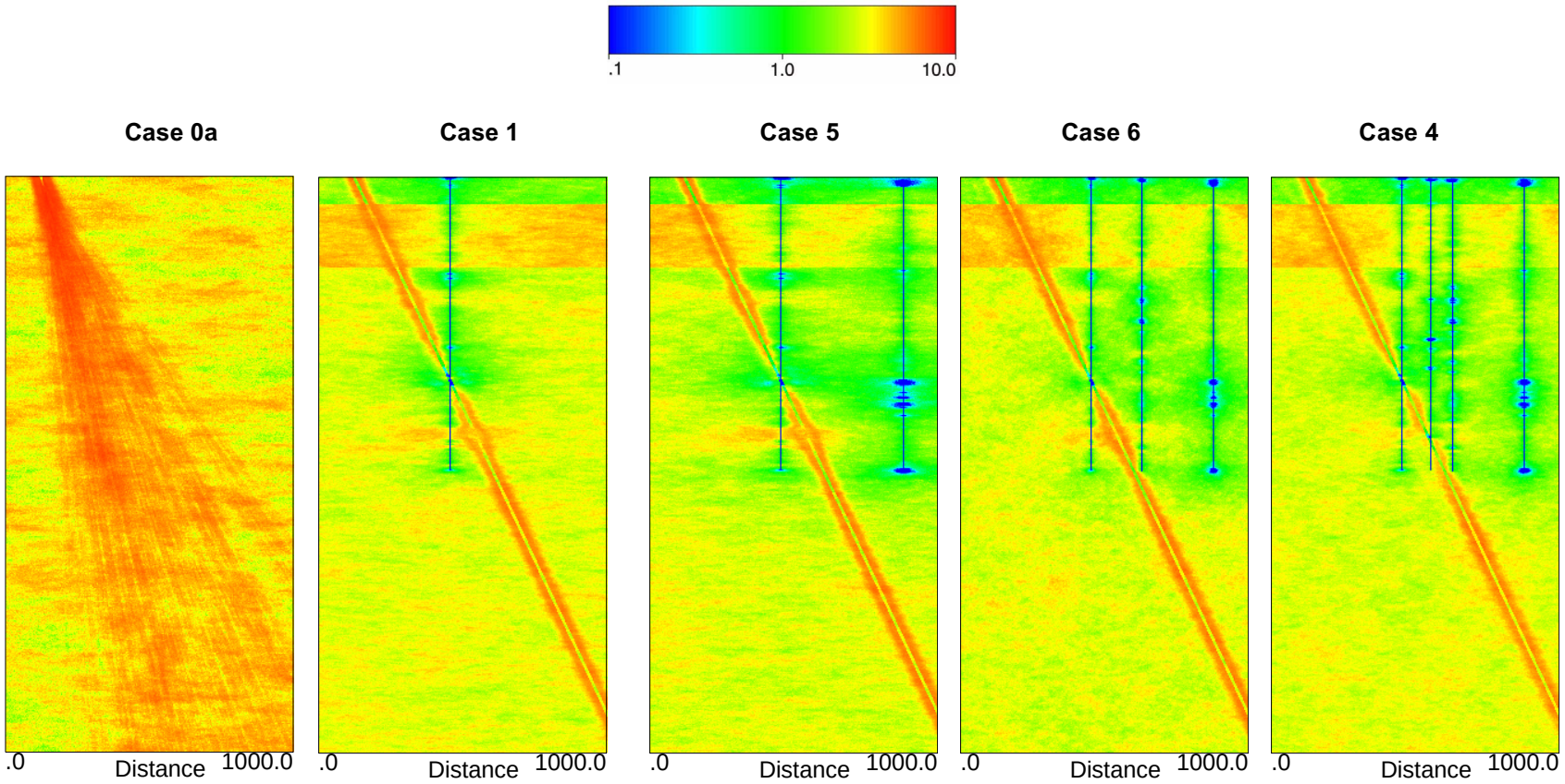

Figure 41. Comparison of E-type fracture-frequency uncertainty models for Drilling Sequence No. 2 (Cases 0a, 1, 5, 6, and 4). Color scale is logarithmic between 0.1 and 10 fractures per meter.

Summary of Drilling Sequence 3

Drilling Sequence 3 is represented by the successive images of figure 42, which portrays the summary E-type frequency models. The associated uncertainty models are presented in figure 43 which follows.

Because the first drill hole of Drilling Sequence 3 is borehole MIU-3, in common with Sequences 1 and 2, the overall visual impression of the changes in expected fracture frequency with additions of drill hole information is similar. The pre-drilling case, Case 0a with its stochastic fault-prior model and absence of vertical fracture zonation is markedly different from the succeeding cases, Case 1, Case 5, Case 7, and Case 4, each of which represents a deterministic fault-prior model. In a similar fashion to Drilling Sequence 2, there is a marked change in the lateral continuity of the low frequency zone present in the two-borehole model (Case 5) when the third drill hole is added (Case 7).

Summary of Drilling Sequence 4

The summary view of Drilling Sequence 4 is presented in figure 44, which shows the successive E-type images of fracture frequency for the pre-drilling case (Case 0a), Case 8, Case 9, Case 10, and Case 4. Notice that figure 44 indicates that the progressive addition of drill-hole-based information with respect to the location of the Tsukiyoshi Fault into Drilling Sequence 4 results in a very much different sequence of images than were obtained for the other hypothetical sequences of drill holes. Figure 45 is a similar sequence of images to that of figure 44, with the exception that the baseline (deterministic) case 10 has been substituted with the alternative stochastic Case 10a.

The principal difference involved in Drilling Sequence 4 is that the dip of the Tsukiyoshi Fault is not firmly identified until drilling of the last hole in the sequence, MIU-3. At each earlier step in this drilling campaign, the dip of the fault either is constrained solely by geologic knowledge (Case 0a and Case 8) or is very poorly (Case 9) to closely (Case 10a) constrained by the available borehole data. This progressive reduction of fault-related uncertainty is clearly indicated by the middle images of figure 45 in particular. Notice that the vertical zonation of background fracture frequency associated with the fault-prior models changes markedly from Case 8 to Case 9 (from two zones to three, and the elevations of the different zones change also).

Figure 46 presents the sequence of images showing the uncertainty associated with the expectation models of figure 44, which contains the baseline Case 10, rather than the alternative (slightly stochastic) Case 10a. The uncertainty models associated with Cases 10 and 10a, originally presented in figures 35 and 36 indicate that the uncertainties associated with this drill hole configuration are very similar.

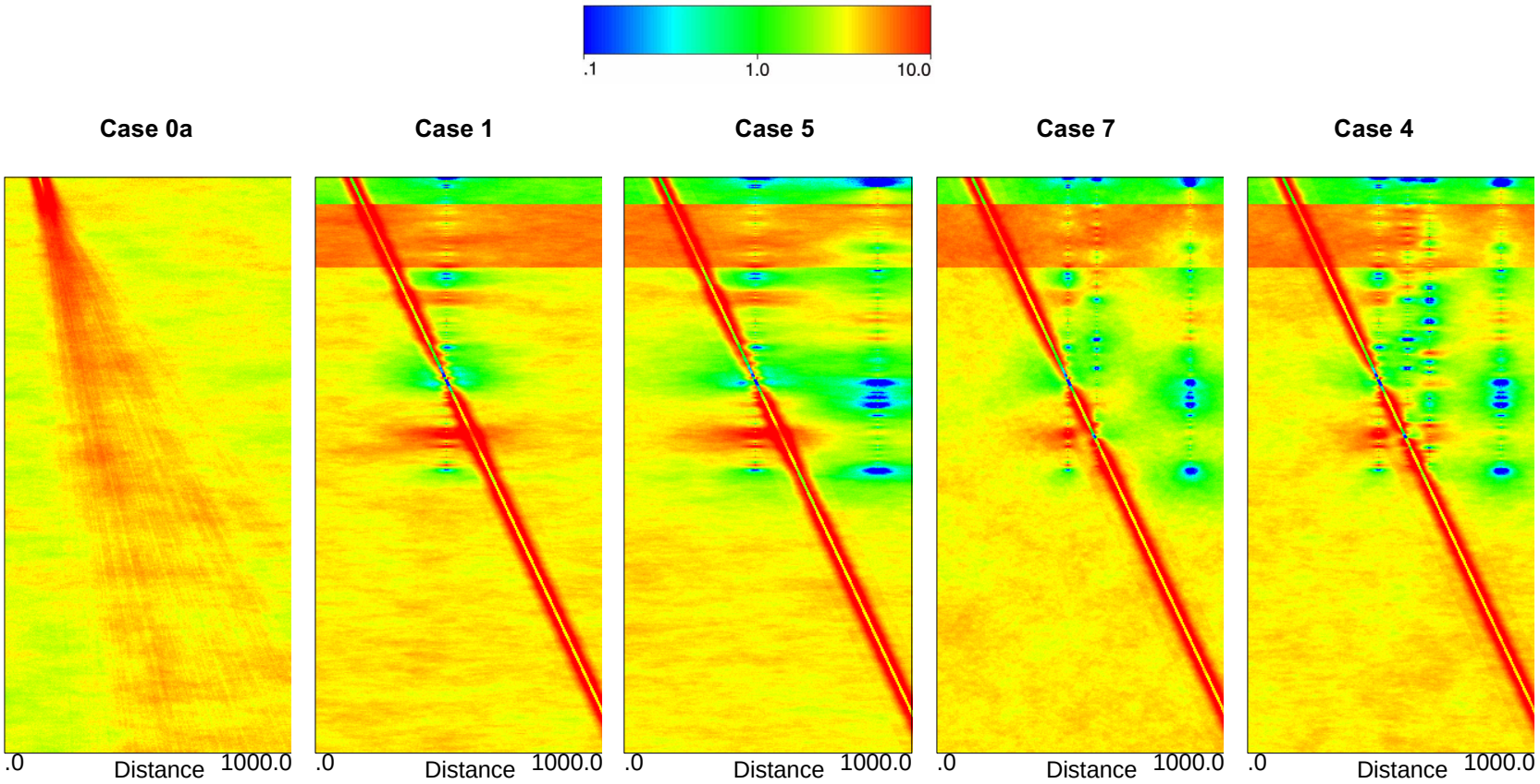

Figure 42. Comparison of E-type fracture-frequency models for Drilling Sequence No. 3 (Cases 0a, 1, 5, 7, and 4). Color scale is logarithmic between 0.1 and 10 fractures per meter.

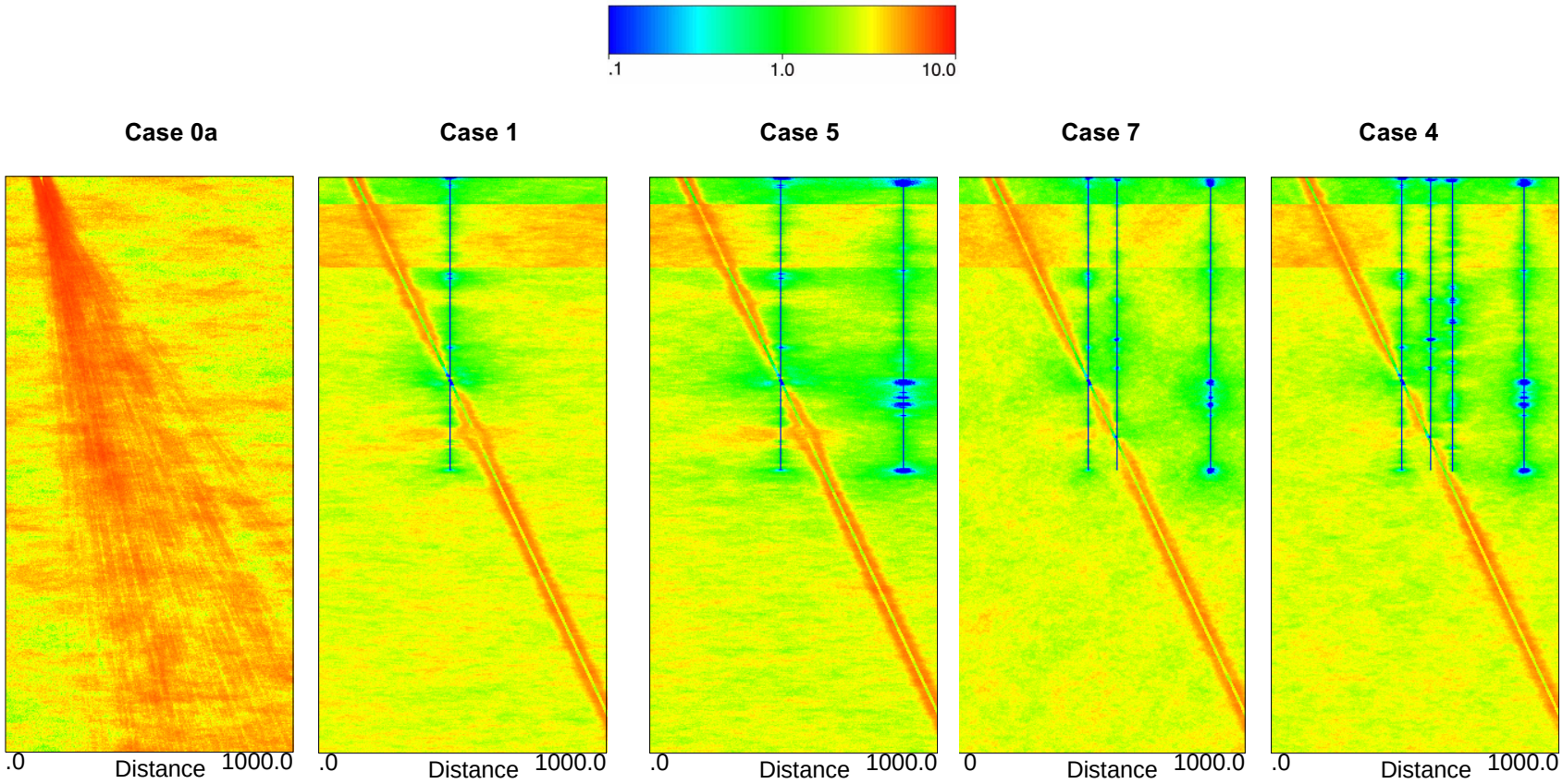

Figure 43. Comparison of E-type fracture-frequency uncertainty models for Drilling Sequence No. 3 (Cases 0a, 1, 5, 7, and 4). Color scale is logarithmic between 0.1 and 10 fractures per meter.

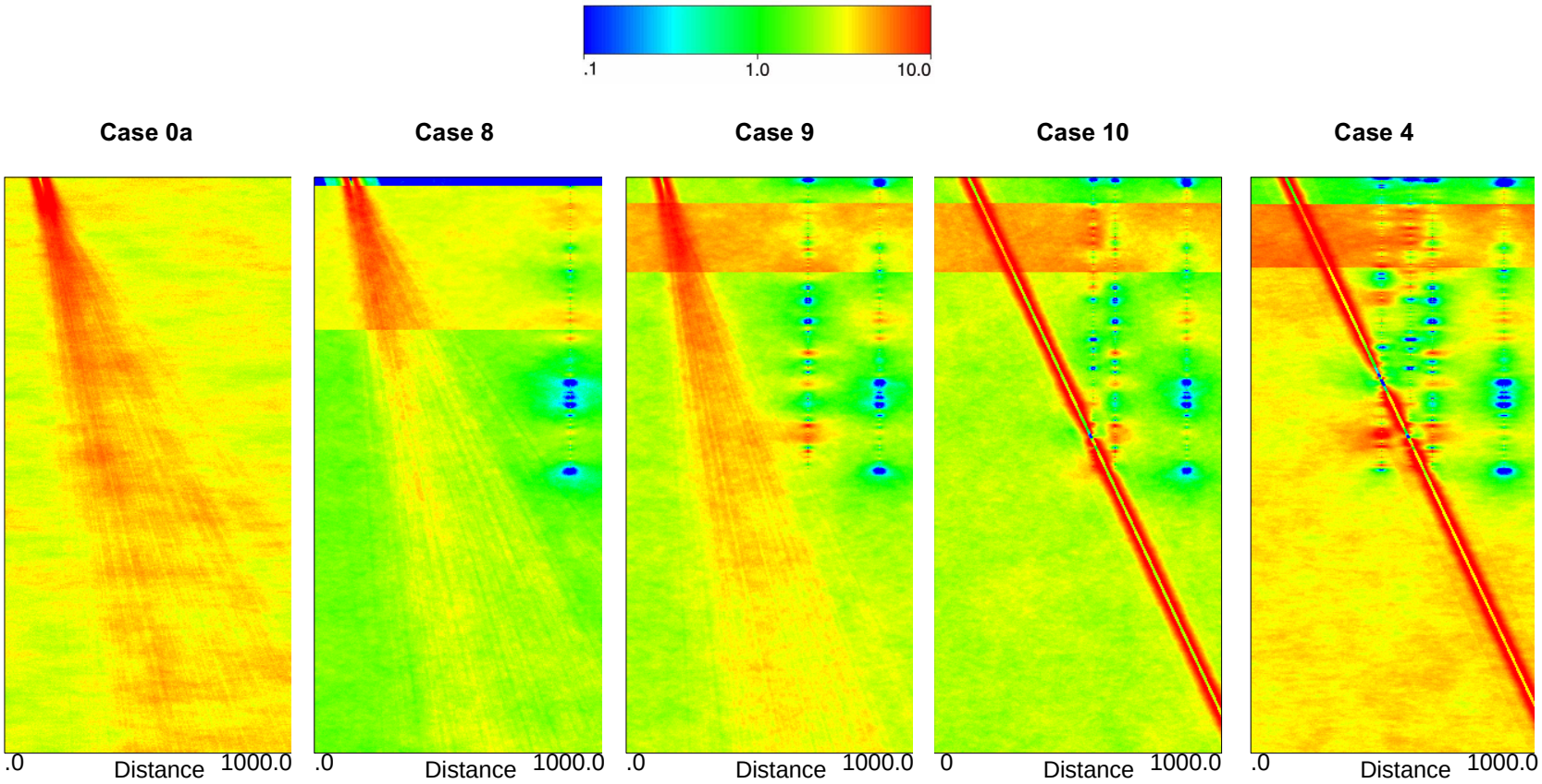

Figure 44. Comparison of E-type fracture-frequency models for Drilling Sequence No. 4 (Cases 0a, 8, 9, 10, and 4). Color scale is logarithmic between 0.1 and 10 fractures per meter.

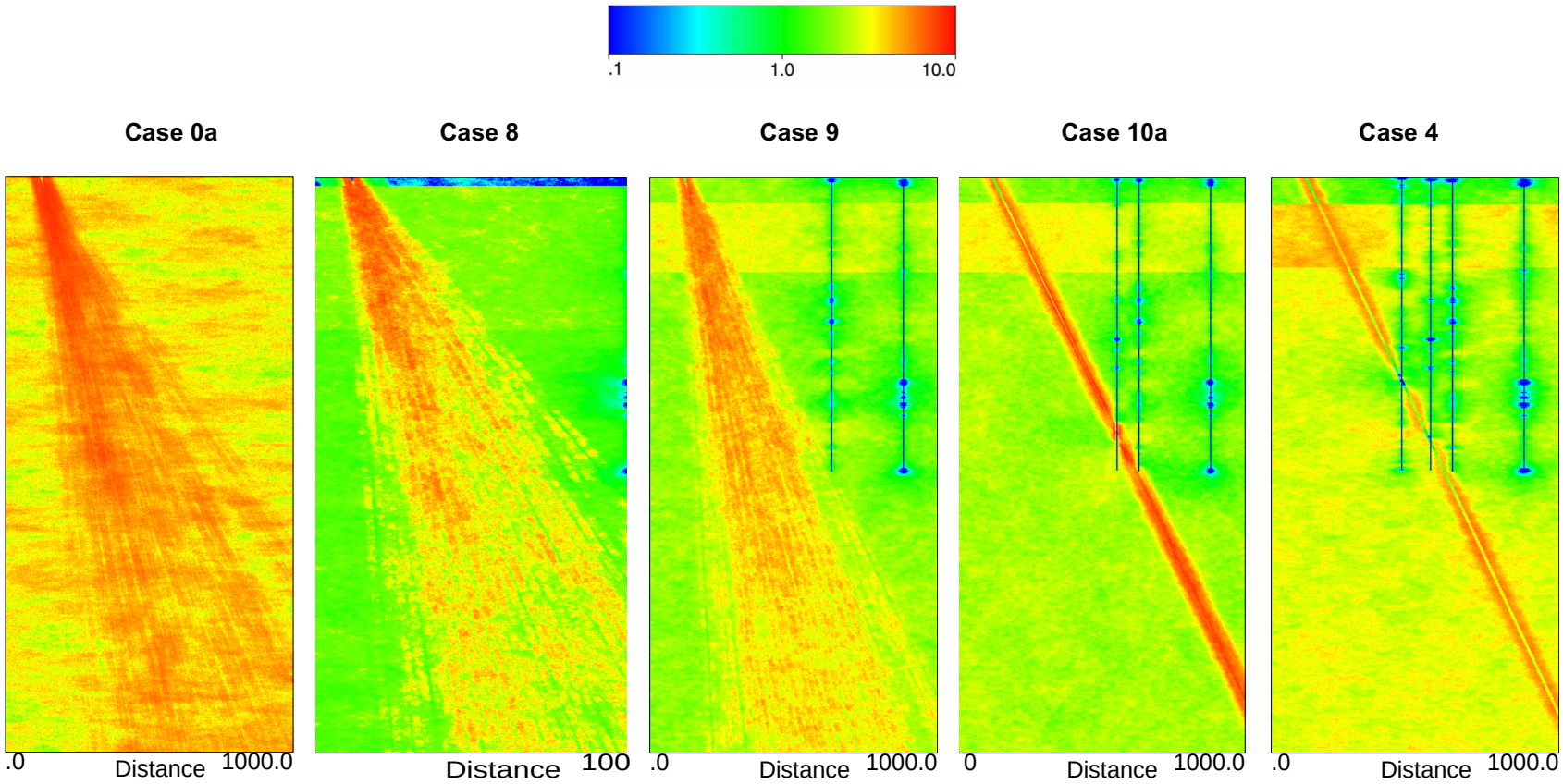

Figure 45. Comparison of E-type fracture-frequency uncertainty models for Drilling Sequence No. 4 (Cases 0a, 8, 9, 10a, and 4). Color scale is logarithmic between 0.1 and 10 fractures per meter.

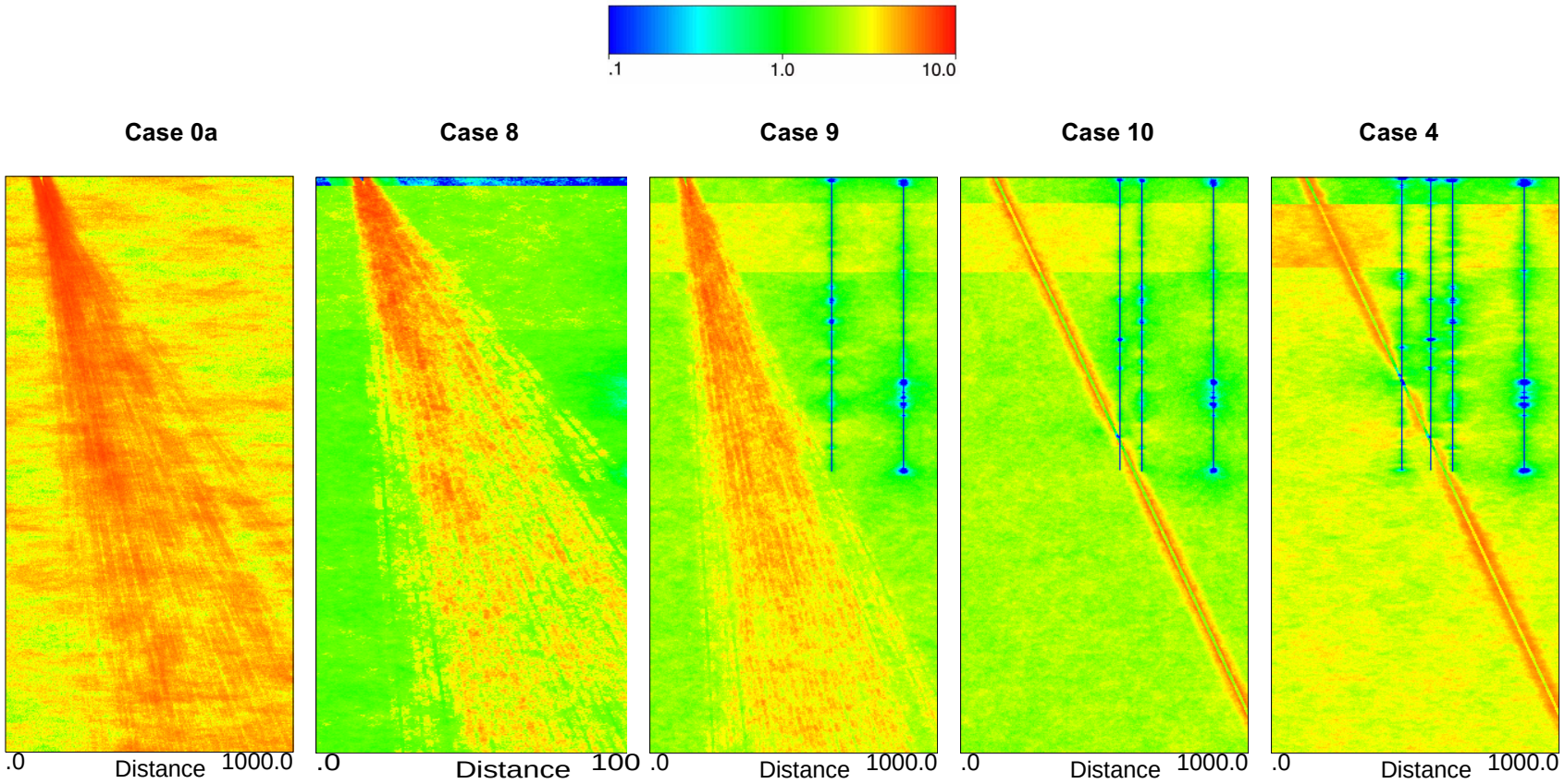

Figure 46. Comparison of E-type fracture-frequency uncertainty models for Drilling Sequence No. 4 (Cases 0a, 8, 9, 10, and 4). Color scale is logarithmic between 0.1 and 10 fractures per meter.

Summary Measures of Global Uncertainty

Whereas the preceding two sections of the *Modeling Results* section have focused on the detailed spatial differences in the uncertainty associated with the four different hypothetical drilling sequences defined in table 2 for the MIU site, we now turn to the presentation of efforts to summarize the uncertainty — and of changes in that uncertainty — with the progressive addition of information *with respect to the model domain as a whole*.

The mechanisms for computing the two global measures of uncertainty across the entire model domain have been presented in the section on *Computation of Global Uncertainty Measures* on page 30, and they involve the use of equations (6) and (7). We have computed the "global" uncertainty measures for the entire model domain (a true global uncertainty), and these results are presented and discussed below.

However, even within a consideration of "global" uncertainty, visual examination of the various figures in the preceding section on *Presentation of Modeling Results by Drilling Sequence*, beginning on page 88, shows significant differences in both the summary E-type models and the conditional standard deviation maps between (1) the region characterized by drilling (roughly the upper right-hand quadrant of the figures) and (2) the remainder of the model domain, which is undrilled. We have attempted to isolate this effect by computing the same "global" uncertainty measures described by equations (6) and (7) for *only* the quadrant of the model domain that contains the maximum four boreholes. The size of each "drilled quadrant" is more than a strict fourth of the model domain. In fact, where the x-dimension of the model is 250 grid nodes, the drilled quadrant extends from node 50 to node 250 (80 percent of the horizontal dimension), and where the y-dimension of the model is 500 grid nodes, the drilled quadrant extends from node 244 to 500 (51 percent of the vertical dimension). On both axes, the nodes are numbered from the lower left corner, as is specified by GSLIB convention (Deutsch and Journel, 1998). This works out such that the drilled quadrant represents approximately 41 percent of the total domain area.

Global Uncertainty Across the Entire Model Domain

Figure 47 presents a four-part graphic illustration comprising the basic uncertainty measures for the entire modeling domain for all four drilling sequences. As is evident in each component image of figure 47, both global uncertainty measures decrease progressively from predrilling Case 0a through the various different modeling cases that add drill holes successively to the composite conditioning data sets. This progressive decrease in global uncertainty is more pronounced for the standard-deviation-based measure than for the one based on the coefficient of variation. This difference is largely as anticipated, in that the coefficient of variation calculation explicitly adjusts for the mean value against which the standard deviation is calculated.

Note that figure 47 also tracks the number of grid nodes for which the computation of either uncertainty measure was impossible, as described originally on page 30. From the information presented in these summary plots, it is evident that the problems involve computation of the coefficient of variation, rather than of the standard deviation, which leads us to suspect that the computational problem is related to E-type modeled values of zero fractures per meter. The coef-

ficient of variation is undefined when the mean is zero [see equation (7)]. Also, note that the number of such computational problems, which originally caused the summary computer routine to crash, is quite modest (maximum number just over 120) when compared to the full model grid of 125,000 nodes. Accordingly, we conclude that there is no meaningful bias introduced into these numerical results.

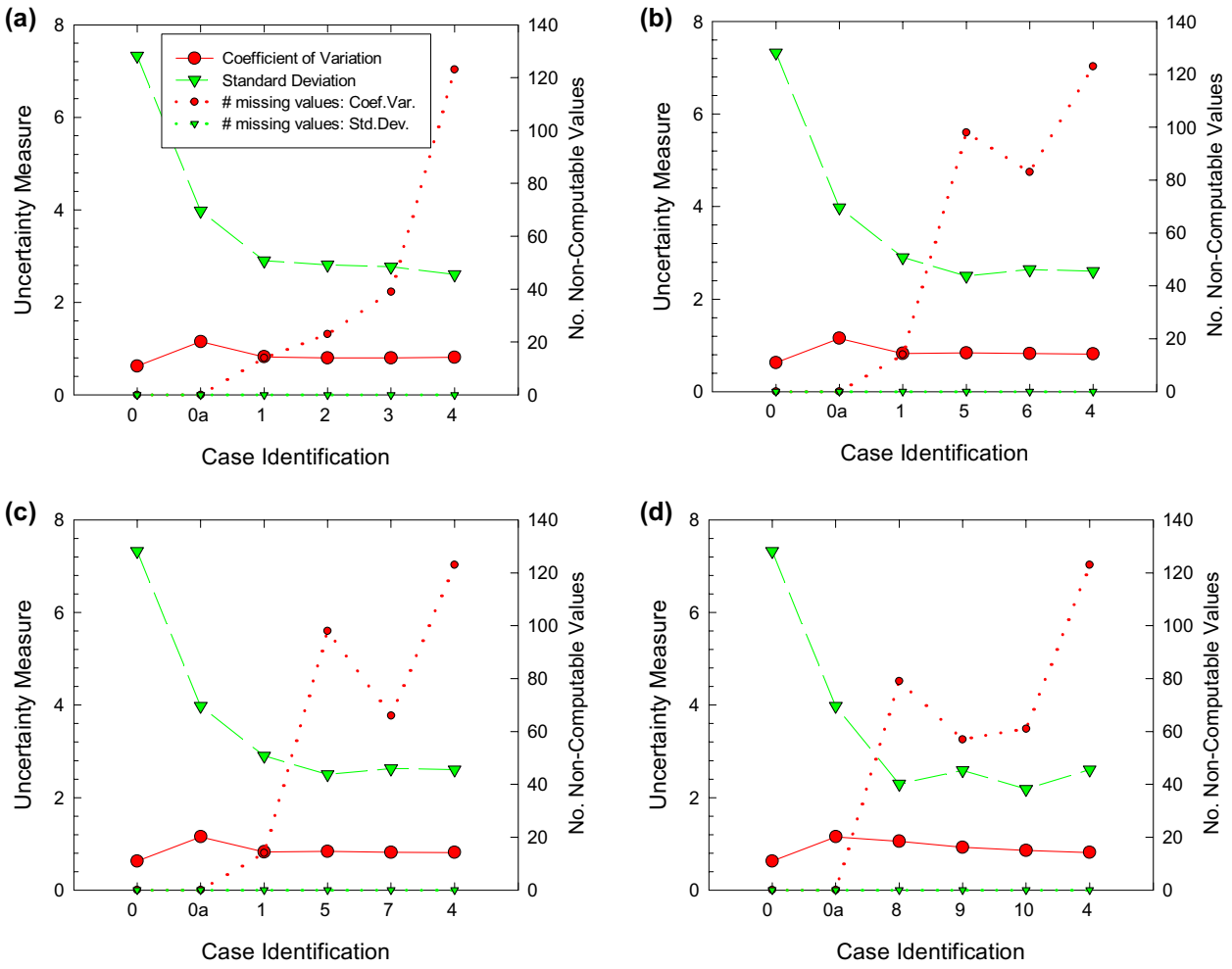

Figure 47. Global, summary uncertainty values for the four hypothetical drilling sequences. (a) Drilling Sequence 1; (b) Sequence 2; (c) Sequence 3; and (d) Sequence 4. Explanation in part (a) only. Number of non-computable values shown to examine potential bias in results; total node count: 125,000.

The greatest decrease in uncertainty is obtained by the addition of the first drill hole, which is reasonable, in that the first drill hole provides the first substantive information from the actual subsurface. Recall that the models for both Case 0 and Case 0a are unconditional and the fracture-frequency distribution (histogram) is based solely on outcrop fracture frequency measurements.

Note also that the graphical "progression" from Case 0 to Case 0a is not really a *progression* involving the addition of information to the modeling. Case 0 used a prior fracture frequency distribution based on the average fracture frequency of all outcrops examined, whereas Case 0a used a prior distribution that was based only on outcrops located within the footwall structural domain. More specifically, the fracture-frequency prior distribution for Case 0a was selected, *somewhat in retrospect*, in light of the apparently anomalous high frequency of fracturing revealed by the outcrop data set as a whole in contrast to the in-situ fracture frequencies indicated by "later" drilling. That the global coefficient of variation value for Case 0 behaves in a markedly different manner than the global standard deviation value for the same case is attributed to standardization of the former by dividing by the markedly greater mean values (overall value: 8.41; table 5), in contrast to the lower mean values of Case 0a (overall value: 2.23; table 5).

An illustration presenting the corresponding *normalized* global uncertainty measures is given in figure 48. Both the computation and purpose of this normalization process was described on page 31. Specifically, it allows comparison of the standard-deviation-based and coefficient-of-variation-based global uncertainty measures on a common scale. In general, the visual impression of the four hypothetical drilling sequences is quite similar to that conveyed by the raw (non-normalized) values shown in the preceding figure. Closer examination of part (d) of figure 48, however, indicates a noticeable departure from the nearly identical global uncertainty values exhibited by the drilling-constrained cases of Drilling Sequences 1, 2, and 3. There is also a marked difference between the behavior of the two different global uncertainty measures.

Specifically, in Figure 48(d), whereas the normalized coefficient of variation exhibits a progressive decrease in global uncertainty as conditioning data are added from the pre-drilling Case 0a through Cases 8, 9, 10, and 4 (unlike the situation for Drilling Sequences 1, 2, and 3) , the normalized global average standard deviation exhibits oscillatory behavior. First, the addition of one drill hole, AN-1 in Case 8, drops the normalized uncertainty below the average drilling-related uncertainty that serves as the normalizing value. Addition of a second drill hole, MIU-1, increases the normalized average standard deviation value above the normalizing value, and addition of the third drill hole, specifically MIU-2, decreases the normalized average standard deviation value once again. Finally, the fourth addition of a drill hole, borehole MIU-3, again increases the average standard deviation value.

The origin of this oscillatory behavior of the normalized standard-deviation-based uncertainty measure is not understood, and it may not be of particularly great significance. However, Drilling Sequence 4 is the one sequence that does not start out with a deterministically located fault zone (compare figure 44 with any of figures 38, 40, or 42). It is highly likely that the prominent continuous negative slope of the normalized coefficient-of-variation-based uncertainty measure [which is more pronounced in part (d) than in parts (a) through (c) of the figure, where it is almost absent] is directly related to this progressive increase of the constraints on the dip of the Tsukiyoshi Fault across Cases 8, 9, 10, and 4.

Global Uncertainty Across the "Drilled Quadrant"

Examination of any of the images summarizing the various modeling cases indicates quite clearly that the drill hole information obtained as part of any of the drilling sequences hypothe-

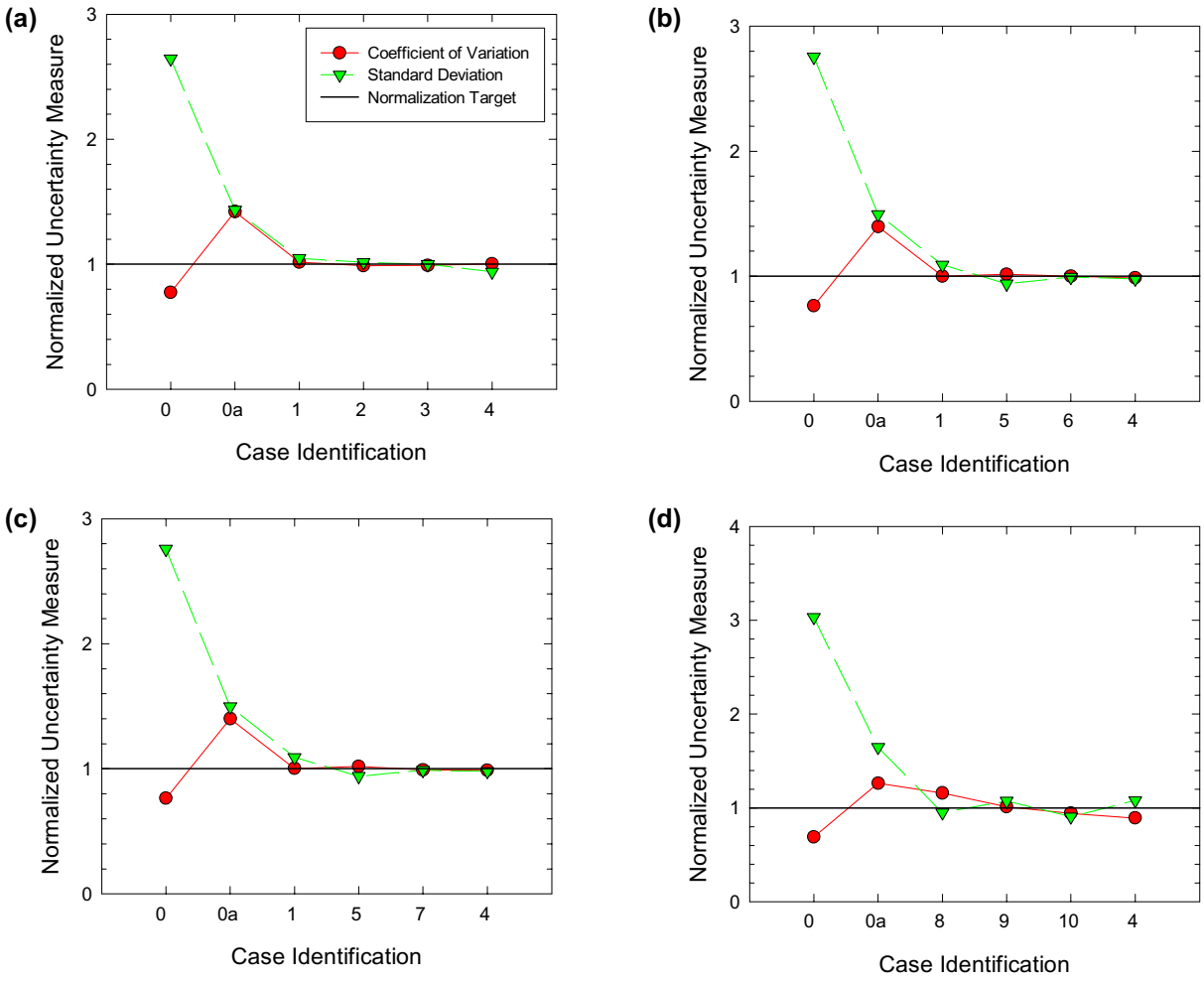

Figure 48. Global, normalized uncertainty values for the four hypothetical drilling sequences. (a) Drilling Sequence 1; (b) Sequence 2; (c) Sequence 3; and (d) Sequence 4. Explanation in part (a) only. See discussion of normalization calculation and purpose on page 31.

sized for this study influences only a portion of the entire model domain (less than approximately 41 percent by grid-node count). The definite majority of the borehole information is from above the trace of the Tsukiyoshi Fault, and there are virtually no hard, drilling-related data from the lower half of the model domain. Therefore, in all four drilling scenarios, the majority of the model is unconditioned by measured data. Additionally, for those modeling cases for which the dip of the Tsukiyoshi Fault is not constrained deterministically (all of Drilling Sequences 1–3), the impact of the unknown fault dip, which is modeled stochastically both in the pre-drilling case and in Cases 8, 9, and 10 of Drilling Sequence 4, works to increase apparent (visual) uncertainty throughout this unconditioned portion of the model.

We have created similar "global" uncertainty measures for what we term the "drilled quadrant" of the model. As described in the section on *Computation of Global Uncertainty Measures* (beginning on page 30), which specifies details of the actual computations, the drilled quadrant includes the portion of the model domain that is affected, ultimately, by all four drill holes,

regardless of the sequence in which they are introduced into the modeling. Figure 49 presents both the effect of the coefficient-of-variation calculation of the range of variation expressed by this uncertainty measure and the spatial extent of the drilled quadrant. Notice that the normalization of the standard deviation by the mean value markedly reduces the layering effect of the different fracture-frequency zones defined in the prior models.

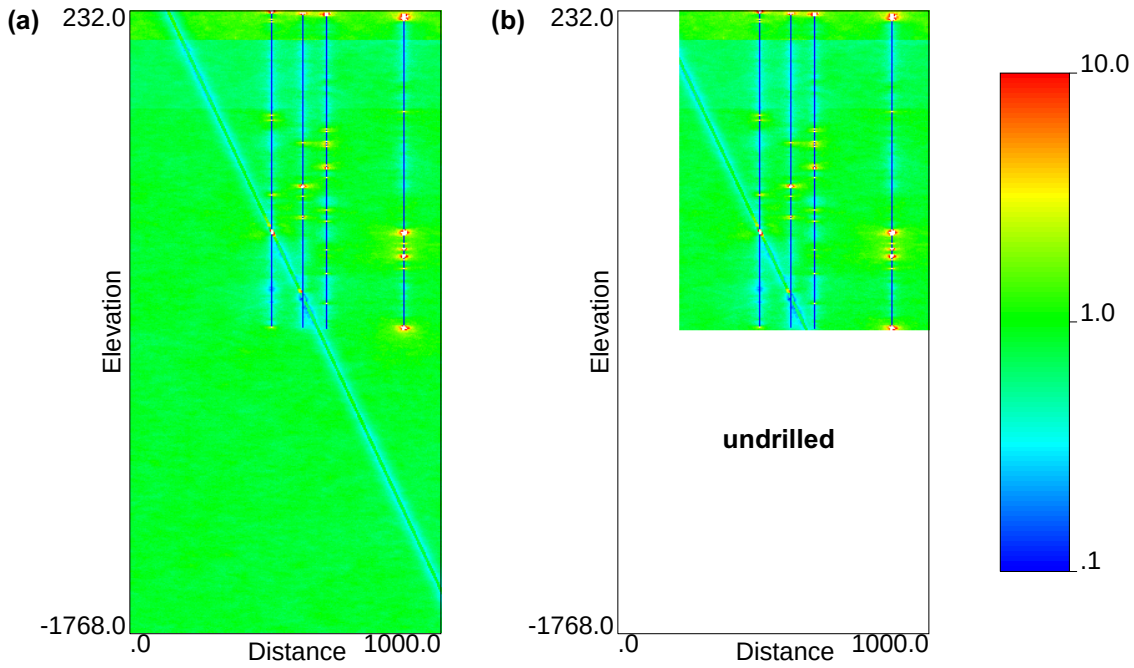

Figure 49. Comparison of (a) the full-field coefficient of variation computation vs. (b) the "drilled quadrant" computation of the same quantity for Modeling Case 4 (with all four boreholes).

Figure 50 presents the quadrant version of the raw uncertainty measures in summary form, and figure 51 presents the normalized version of the same information. In general, the same trends with respect to progressive reduction of uncertainty with successive additions of borehole data to the modeling cases that were observed for the full-model-domain versions of the uncertainty figures are observed in figures 50 and 51. Additionally, the same somewhat anomalous behavior of uncertainty with respect to Case 0 and Case 0a is repeated as well. This behavior was attributed to standardization of the conditional standard deviations in Case 0 by the higher overall expected mean fracture frequency value for this case, in contrast to that of Case 0a.

What is *not* necessarily immediately obvious is that the absolute magnitudes of the coefficients of variation for the drilled quadrant are markedly reduced with respect to the magnitudes of these same values computed for the full extent of the model domain. In fact, comparison of the equivalent parts of figure 50 with those in figure 47 suggests that the values of the quadrant coefficients of variation are one-half or less of the values for the full-field quantities. The original values are somewhat less than 1.0 and the quadrant values are on the order of 0.3. We attribute this reduction not only to the influence of the conditioning data, which should act to reduce variability from realization to realization, but also to the exclusion of a vast number of essentially uncondi-

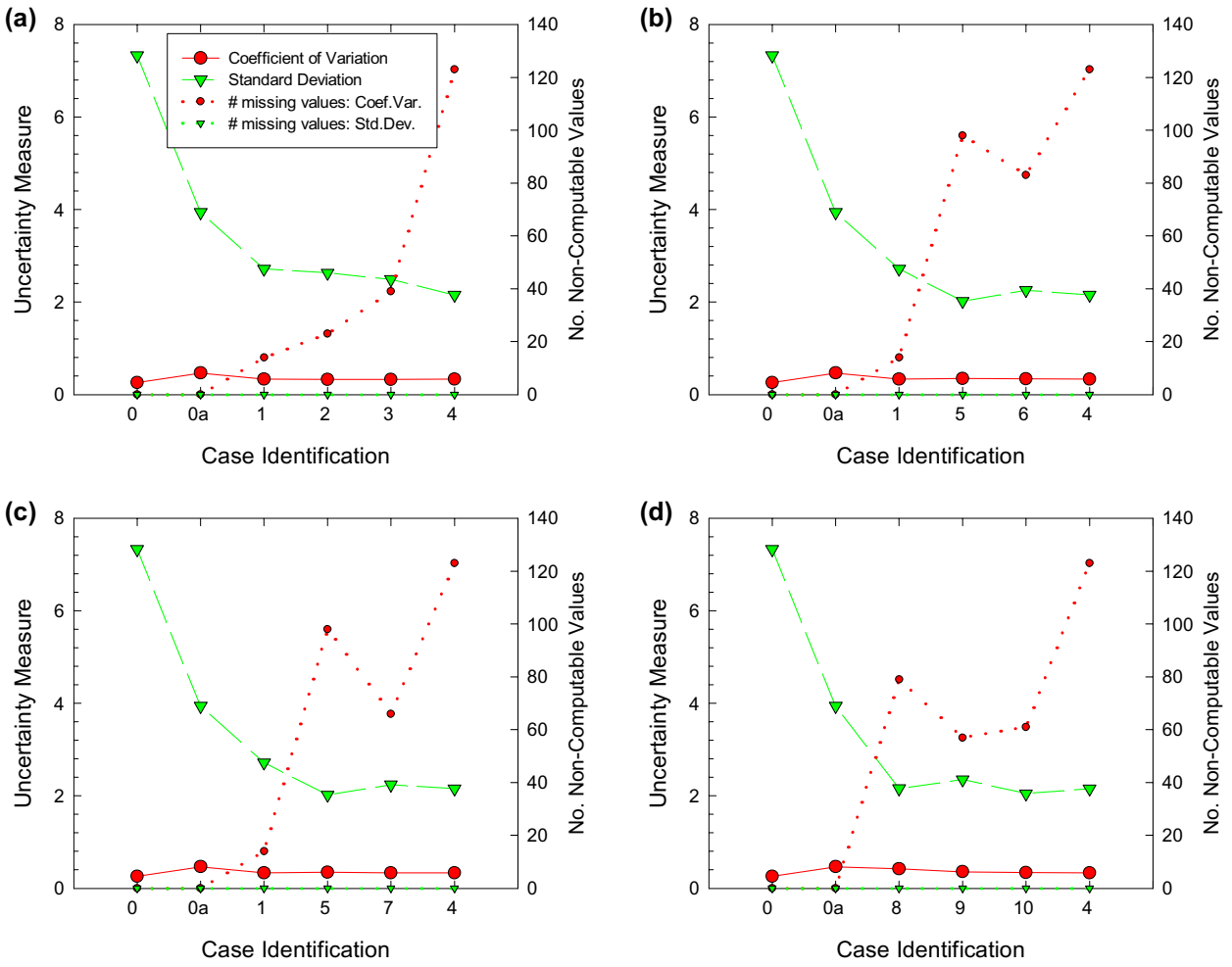

Figure 50. Basic summary uncertainty measures for the drilled quadrant of the model domain, as discussed in the text. (a) Drilling Sequence 1; (b) Sequence 2; (c) Sequence 3; and (d) Sequence 4. Explanation on part (a) only. Number of non-computable values shown to examine potential bias in results; total node count: 125,000.

tioned grid nodes that are located within the blank areas of figure 49(b). This effect is completely lacking for the normalized quadrant uncertainty values, because of the effect of "double" normalization of the coefficients of variation in this latter instance.

Impact of Uncertainty in the Prior Model vs. Uncertainty in the Simulated Models

Understanding the relationship between the uncertainty contained in the prior models of fracture frequency and that uncertainty present in the final, conditionally simulated models of fracture frequency is also of interest in this modeling exercise. However, the concept of uncertainty in the prior models is relevant only to some of the modeling cases described in table 3 — those cases for which the position of the Tsukiyoshi Fault is not deterministic by virtue of inclusion of drill hole MIU-3 in the composite data set.

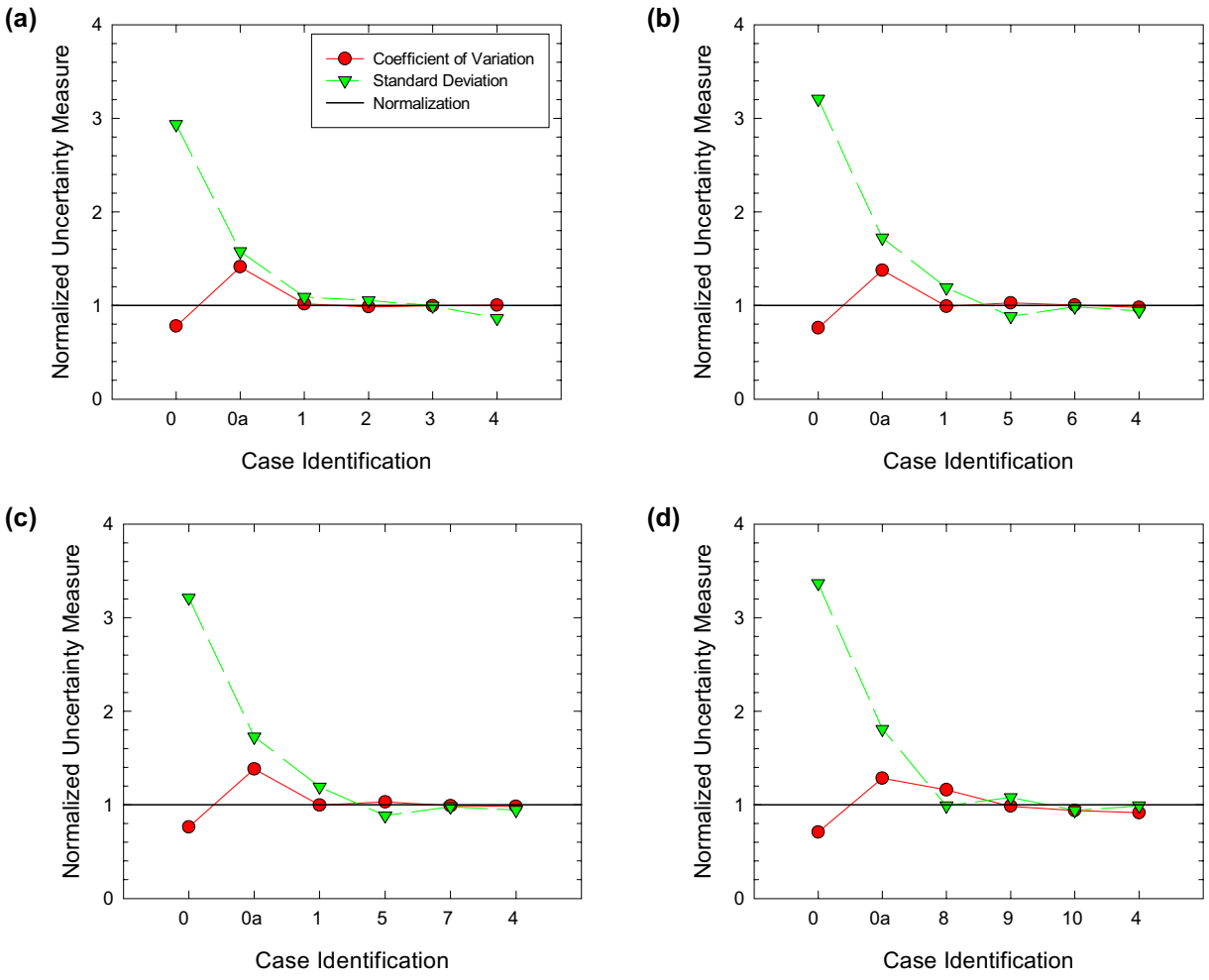

Figure 51. Normalized summary uncertainty measures for the drilled quadrant of the model domain, as discussed in the text. (a) Drilling Sequence 1; (b) Sequence 2; (c) Sequence 3; and (d) Sequence 4. Explanation on part (a) only.

Uncertainty Associated with Stochastic Fault-Prior Models — Figure 52 presents an explicit comparison of the average uncertainty measures, both as coefficients of variation and as standard deviation, for Cases 0, and 0a (pre-drilling), and for Cases 8, 9, and 10a (all belonging to Drilling Sequence 4, prior to addition of the final hole of this sequence). One set of histogram bars represents the average uncertainty associated with the stochastic fault-prior models, whereas the other set of bars represents the uncertainty associated with the final simulated models incorporating those fault priors. These results are given both for the full model domain (because the stochastic fault prior affects the entire domain) and for the drilled quadrant in separate parts of figure 52.

Parts (a) and (b) of figure 52 show with the coefficient-of-variation approach to global uncertainty, whereas parts (c) and (d) involve the standard-deviation approach. Note that the absolute magnitude of the coefficients of variation obtained from the entire model domain [part (a)]

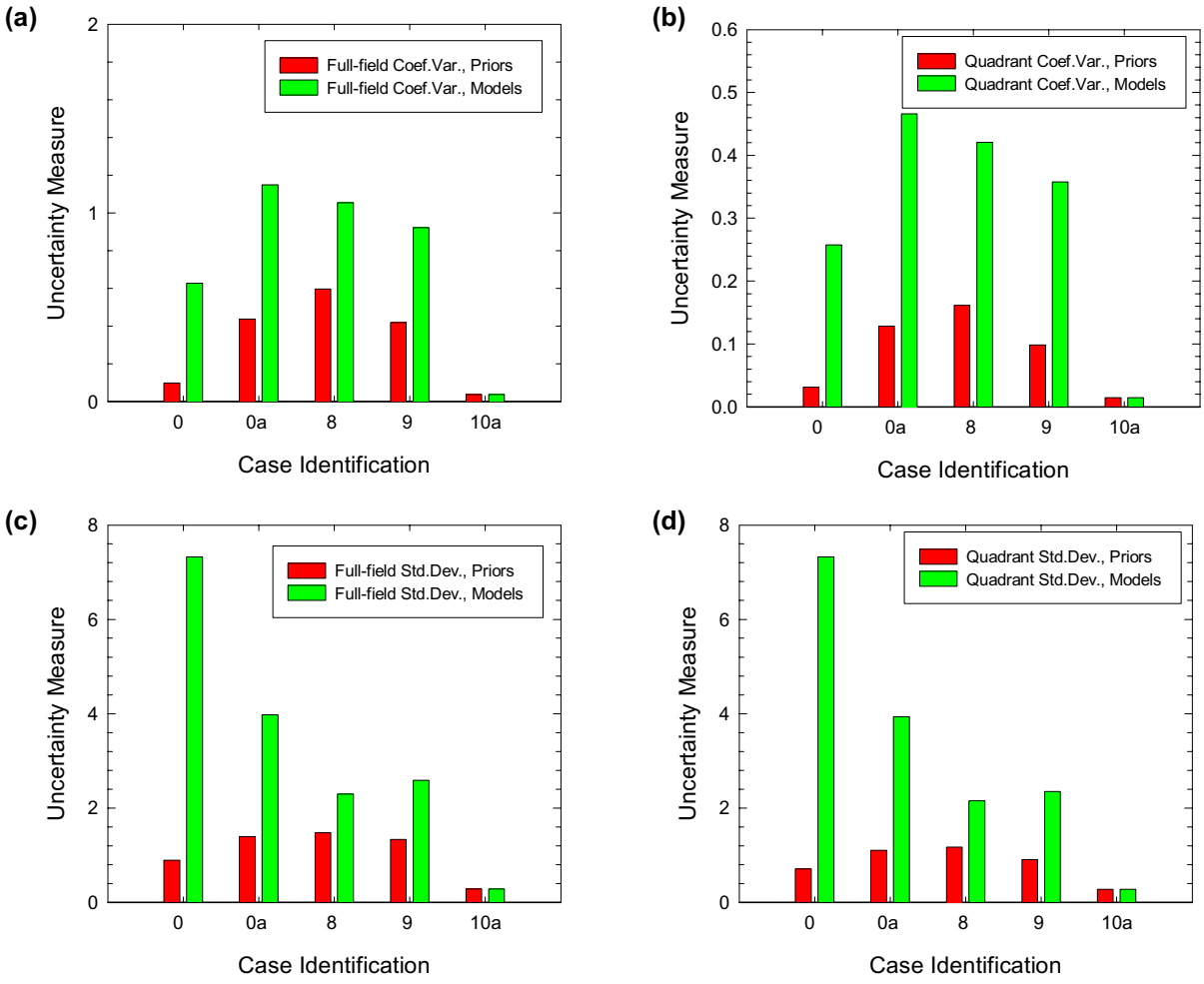

Figure 52. Comparison of global uncertainty in the prior fracture frequency model (red bars) with global uncertainty in the final simulated models (green bars) for cases with stochastic prior models (all belong to Drilling Sequence 1). (a) Full-field coefficients of variation; (b) full-field standard deviations; (c) drilling-quadrant coefficients of variation; (d) drilling-quadrant standard deviations.

and for the drilled quadrant [part (b)] differ by roughly a factor of two, with the average coefficient of variation from the drilled quadrant being smaller. We attribute this difference in magnitude to the normalization of the standard deviation at each grid node by the mean values at those same grid nodes. That this is the cause of the smaller values and that this observation is not directly related to the reduced variability as a whole is suggested by comparison of parts (c) and (d) of figure 52, which show the average uncertainty for the two modeled regions in terms of standard deviation. These two images are essentially identical. Note, however, that the uncertainty in the final models does decrease progressively with the addition of successive drill holes to the drilling data set (from Case 0/0a to Cases 8, 9, and 10a).

Overall interpretation of the results presented in figure 52 is somewhat difficult, because of the different absolute values of the two different uncertainty measures. However, one might be tempted to conclude that *as much as approximately half of the uncertainty exhibited by the final*

simulated models might reasonably be attributed to uncertainty contained within the fault-prior models for these fully stochastic cases. This conclusion applies to the evaluation of the entire modeling domain, even though somewhat less than three-quarters of that domain is completely unconstrained by drill-hole data. *For the drilled quadrant only, the fraction of uncertainty contributed by the fault-prior models might be considered to be closer to one-third to one-quarter.*

This value of one half of the global uncertainty being related to the fault priors derives from figure 52(a), in which the global coefficient of variation for the fault prior is roughly one half the value of the global coefficient of variation for the average simulated model for Cases 0a, 8, and 9. Recall that the coefficient of variation for Case 0 is inherently going to indicate a different value because of the higher background fracture frequency suggested by the outcrop studies as a whole (table 5). Normalization of the standard deviations in this case by this larger mean-frequency value results in a smaller magnitude of the coefficient of variation.

The pronounced decrease in the uncertainty measures for Case 10a is not fully understood. However, reference back to figures 35 and 36 (page 85 and page 86,respectively), which graphically portray the fundamental differences between these two cases [in one (Case 10) the fault is deterministic and in the other (Case 10a), the fault is stochastic but *very* tightly constrained], suggests that the degree of constraint in the stochastic case is so strong that there is scarcely any variability between realizations for either the fault prior by itself or for the conditional simulations as a whole. For a wholly deterministic model, the uncertainty is precisely zero, and we would logically expect both types of global uncertainty measures to approach this value as a stochastic model became more and more tightly constrained.

If we consider the results in figure 52 for only the drilled-quadrant portion of the domain [parts (b) and (d) of the figure], it would appear that the stochastic-fault-prior models contribute a markedly smaller fraction of the total uncertainty — perhaps roughly one fourth, based on the coefficient of variation values in part (b) of figure 52. This somewhat contradictory interpretation (the drilled quadrant is where the measured data values influence the simulations, and yet the uncertainty contribution attributable to those data via the simulation process is larger) can be explained by reference to the possible geometries of the fault-prior model(s) shown in figure 16, in particular [compare also with figure 49(b)]. For the "full" model domain case [figures 52(a) and (c)], the stochastic fault trace can "sweep" throughout a very significant portion of the total area involved. In contrast, for the drilled-quadrant case [figures 52(b) and (d)], the portion of the "domain" that can be affected by the stochastic fault is much reduced. Thus, we can logically expect that the uncertainty contributed by the fault-prior models should decrease as a proportion of the total uncertainty.

At first consideration, that the uncertainty associated with the final models, which include actual subsurface conditioning data via drill holes, would be *greater* (substantially greater in some instances) than the uncertainty associated with the fault-prior models (which contain no drill hole data at all) may seem counterintuitive. One might reasonably expect uncertainty to *decrease* with the addition of the drill hole information. However, recall that the global uncertainty measures are actually defined as ***variability***, which is then taken as an empirical ***surrogate*** for uncertainty, per se. The fault-prior models, whether or not the fault itself is taken as deterministic or stochastic, actually contain very little variability, because the spatial distribution of *background* fracture fre-

quency is assumed, a priori, to be constant, at least within fixed zones. Thus, with the exception of a nominally 80-meter band (two-sigma width of 40 m on each side of the fault trace) directly associated with the Tsukiyoshi Fault, the variation in prior-fracture-frequency values across the replicate fault priors is precisely zero. It is during the geostatistical simulation process that this (unvarying) prior estimate is merged with the hard data (of only limited spatial influence) to produce a fully varying spatial distribution of fracture frequency conditioned to both the prior estimates and the measured values.

Uncertainty Associated with Deterministic vs. Stochastic Prior Models —Because there is no uncertainty associated with the fault-prior models associated with the drilled cases of Drilling Sequences 1, 2, and 3, it is interesting to compare the total uncertainty across all of the different modeling cases. These results are presented in Figure 53; however, only results for the drilled quadrant of the model domain are given, because of the greater relevance of this region to the objectives of this study.

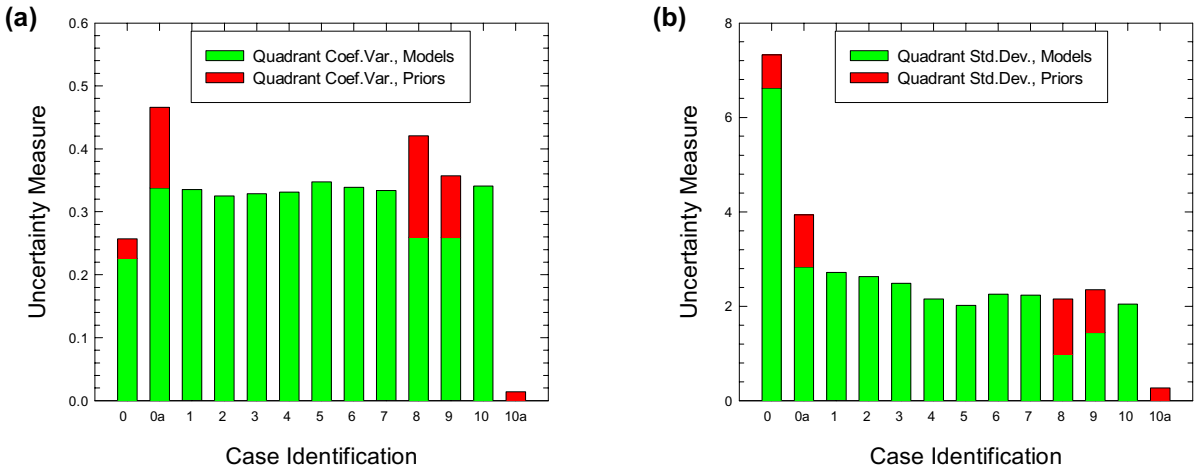

Figure 53. Comparison of drilled-quadrant uncertainty measures for all modeling cases. (a) Coefficients of variation; (b) standard deviations. Uncertainty associated with fault-prior models shown separately, with the total height of each bar representing overall uncertainty partitioned into prior-model-related and simulation-related components.

In contrast to figure 52, for which the uncertainty measures associated with the (stochastic) fault-prior models were shown as separate values from the uncertainty measures associated with the final models, figure 53 shows the two different types of uncertainty on the same bar. This makes explicit the fractional contribution of the fault-prior models to the total uncertainty of the final models. For the cases involving stochastic prior models, the uncertainty value associated with those models was simply subtracted from the final uncertainty value, and the part associated with the prior models stacked on top of the remaining quantity in a different color. For the cases involving deterministic fault-priors, this subtraction is meaningless as there is no uncertainty in the fault-prior models, and the entire uncertainty value (bar) shown represents uncertainty associ-

ated with the stochastic simulation process. Again, note the difference in absolute magnitude of the two different global uncertainty measures.

The impact of uncertainty associated with the unknown location of the fault itself, with its higher-fracture-frequency zone, is clearly indicated in the differences between the pre-drilling Case 0a and the first-drill-hole cases of Case 1 (for Drilling Sequences 1, 2, and 3) and Case 8 (Drilling Sequence 4). In both parts (a) and (b) of the figure, the difference in total uncertainty between Case 0a and (in particular) Case 1 is attributable to the stochastic fault location vs. a deterministic fault location with zero uncertainty.

Effect of Progressively Increasing Constraints on Fault Location — The behavior of this uncertainty partitioning for Cases 8, 9, and 10 (Drilling Sequence 4) is also interesting. Recall that Case 8 had an unconstrained fault prior and only one drill hole (borehole AN-1). Case 9 had a poorly constrained fault-prior model, constrained effectively only by the lack of penetration of the Tsukiyoshi Fault by the second borehole in the sequence, drill hole MIU-1. Accordingly, the prior-model-related uncertainty, shown in red, appears to decrease between the two models, but the total uncertainty, shown by the overall heights of the two bars, increases from Case 8 to Case 9. As discussed in the sections on Cases 8, 9, and 10 under the *Comparison of Summary E-Type Models with Prior Models* (page 79 through page 84), an explanation was hypothesized for this increased uncertainty as related to lateral juxtaposition of conflicting fracture-frequency data in the two boreholes involved in Case 9. Addition of a third drill hole (borehole MIU-2) to Case 10 converts the fault-prior model to a deterministic situation with zero prior-related uncertainty. However, the addition of measured information and the associated changes in the spatial continuity model (variogram) cause the quantity of simulation-related uncertainty to increase, even though total uncertainty decreases.

It is also important to note that the *total* uncertainty (as measured by the standard deviation) associated with Case 8 (overall bar height), with only one borehole, is markedly less than the total uncertainty associated with Case 0a, the pre-drilling case for this same drilling sequence. Both Case 0a and Case 8 have the same unconstrained prior fault model, for which the dip of the fault can vary stochastically from dips of 55 to 90 degrees. Indeed, the heights of the fault-prior (red) portion of the two bars for these cases in figure 53(b) appear virtually identical.

Effect of a Layered Fault-Prior Model — Although it is tempting, and indeed logical, to attribute some of this decrease in total uncertainty to the addition of the first drill hole data in Case 8, there may be a contribution to the reduction in uncertainty that could be attributed to the addition of a layered component to the prior model of fracture frequency. Specifically, compare the prior models of figures 25(a) and 33(a). This prior estimate of layering is then held constant across all of the simulations in Case 8. Although the prior estimate of layering changes between Case 8 and the succeeding Cases 9, 10 (10a), and 4 because of the addition of additional drill-hole data into the composite data sets, it appears as though the injection of additional information via the prior estimates involving a set of expected background fracture frequencies may be reducing the total uncertainty over the completely unconstrained Case 0a. If this is the case and the effect of the more precise specification of the locally varying mean values does contribute to the reduction of overall uncertainty, *then it may be that indirect (i.e., geophysical) methods of estimating major changes in fracture intensity prior to drilling could be of significant value.*

A potential difficulty with this explanation involving a layered prior estimate for the locally varying mean, however, involves the differences in uncertainty reduction between moving from Case 0a to Case 8 (as just discussed), and moving from Case 0a to Case 1. In the Case 1 instance, there is zero uncertainty associated with the fault prior, because the fault, as identified by drill hole MIU-3, is deterministic. Also, the prior for Case 1 is layered, as it is for Case 8 (and, indeed, for all other cases involving at least one drill hole). Examination of the differences between the relevant uncertainty bars in figure 53 for the standard-deviation-based uncertainty measure and the coefficient-of-variation-based measure may be instructive in this respect.

Recall that Case 8, involving only the most distant drill hole (AN-1), led to the assumption of a layered prior model (ignoring for now the impact of the stochastic fault dip) with a distinctly lower overall background fracture frequency (figure 10; table 6) than was inferred for any of the other modeling cases (figures 9 through 11; table 6). In the presence of heteroscedasticity, a population with a generally smaller magnitude of values will tend to exhibit a lower standard deviation than a population with a generally larger magnitude of values. In the current instance, the non-fault-related uncertainty bar in figure 53(b), the standard deviation, is much lower in value than the (also non-fault-related) uncertainty bar in figure 53(a), the coefficient of variation. Because the coefficient of variation is defined as the standard deviation divided by the mean [also see equation (7), page 30], the lower mean background frequency value in Case 8 is discounted to some extent, compared to Case 1. Notice, though, that the effect of lowered non-fault-related uncertainty in Case 8 *is not completely removed* by this normalization process. This would tend to suggest that the introduction of layering into the prior spatial-frequency model *does* exert some discernible effect on overall uncertainty.

SUMMARY AND CONCLUSIONS

Summary of Modeling Activities

Four hypothetical drilling sequences have been defined to examine the effects of the sequential addition of drill-hole-derived information regarding fracture frequency in granitic rocks at the future location of the MIU research facility site in central Japan. Beginning with a pre-drilling situation, in which the only available information on fracture frequency in the subsurface is based on outcrop fracture-mapping studies, measured fracture frequency data from deep boreholes are added, one drill hole at a time, and the fracture frequencies throughout the entire modeled domain are modeled probabilistically using geostatistical techniques.

The geostatistical algorithm of sequential Gaussian simulation has been employed for this modeling and uncertainty-assessment exercise. Following identification (or assumption) of the spatial correlation structure for a given modeling case, 100 equally likely, replicate realizations of fracture frequency, conditioned to the available drill hole measurements (if any), were generated and post-processed to yield both a model of "expected" fracture frequency for the domain and of the uncertainty associated with that expected-value model. Uncertainty in this case is defined as the variability across the 100 individual simulated models for each modeling case.

Uncertainty, or variability among members of a particular suite of geostatistical realizations, has been demonstrated to vary spatially. Uncertainty is effectively zero at the location(s) of conditioning data, specifically at boreholes, in that a *measured* value of, for example, 6 fractures per meter is not subject to *modeling* uncertainty. Uncertainty is large at great distances from conditioning data, and the specific spatial patterns of uncertainty distribution surrounding and in between boreholes is dependent upon both the data locations and the spatial continuity (variogram) model identified from the data.

Spatial variability of uncertainty among different realizations for a particular modeling case is also a function of knowledge regarding the position of the Tsukiyoshi Fault in the subsurface. The surface location of the fault trace is known, as well as the dip of the fault in outcrop. However, the exact position of the fault trace at depths of up to 2 km in the subsurface is uncertain unless and until that fault plane is penetrated in one or more boreholes. Three of the hypothetical drilling sequences identify the fault at depth in the first drill hole (borehole MIU-3). The fourth drilling sequence does not identify the precise subsurface position of the Tsukiyoshi Fault until addition of the final borehole. For both this fourth drilling sequence and the pre-drilling case for which no drill-hole information exists, the position of the fault is modeled stochastically, with a variety of potential fault dips bounded by geologically and geophysically inferred limits and with a modal expectation identical to the dip of the fault in outcrop. Spatial contrasts in uncertainty between modeling cases involving stochastic fault-prior models and those with a deterministic fault-prior model are considerable.

Uncertainty has also been summarized on a "global" basis for each drilling and modeling case, both for the entire model domain as a whole and for the "drilled" quadrant. This distinction was presumed necessary in that only somewhat more than one-quarter of the entire domain was sampled (and conditioned in the simulation process) by drilling. Two different measures of global

uncertainty have been defined: one based on the standard deviation and one on concepts of the coefficient of variation. The two measures differ in absolute magnitude, but the coefficient-of-variation-based measure tends to discount the effect of statistical heteroscedasticity and locally varying prior expectations of variable fracture intensity by normalizing the standard deviations by the locally varying mean values.

Interpretive Conclusions and Implications

The geostatistical modeling activities involved in this analysis and generation of stochastic fracture-frequency models lead to some definite conclusions and implications for sequential drilling site-characterization activities. These are given below in list form for emphasis, with additional discussion interspersed.

1. Comparison of the two global uncertainty measures for each drilling sequence indicates a common, progressive decrease in uncertainty from the pre-drilling (no subsurface data) case to lower values with the successive additions of information based on the drill-hole-obtained fracture-frequency measurements.

Interestingly, the addition of even a single drill hole to any of the drilling sequences results in a marked reduction of global uncertainty, and the global uncertainty associated with the addition of more drill holes to the data sets decreases the global uncertainty disproportionately less.

2. It is possible that it is the introduction of a layered background-fracture-frequency prior (based on the subsurface data from at least one drill hole, in the current instance) that is generating the "one-drill-hole" reduction in global uncertainty.

It would be possible to test whether it is the presence of the layered (spatially-specific) prior frequency model alone that is driving the uncertainty reduction by generating a layered fault prior and generating a suite of simulations, but *not* explicitly introducing a conditioning drill hole data set. The results of this test might lead to conditional implication 3, below.

3. If the uncertainty reduction is observed in the proposed numerical experiment, then it may be that geophysical investigations, or other remotely sensed data bearing on the subsurface fracture distribution for large vertical intervals of rock, would be of substantial value *prior* to drilling.

Returning to the actual observations from modeling effort:

4. It was demonstrated that there is a general lack of large, progressive reduction in uncertainty with increasing drill-hole data content. In other words, the additions of boreholes 2, 3, and 4 in each sequence did not produce an apparently proportional decrease in uncertainty compared with the addition of drill hole number 1.

This lack of continued substantial reductions in global uncertainty is interpreted as follows. For the pre-drilling case, the only spatial correlation model that can be used is necessarily wholly assumed. For the cases involving one drill hole, a reasonable, measurement-based model

of spatial correlation can be developed in the vertical dimension, but the model of continuity in the horizontal dimension remains an assumed quantity. A somewhat arbitrary, and presumably (in retrospect) flawed *prior assumption* of horizontal-to-vertical anisotropy in the two ranges of spatial correlation affected the modeled ranges of horizontal correlation until quite late in the various drilling sequences, at which point, even the limited (sparse) experimental variogram computed in the horizontal dimension suggested a far shorter horizontal range of correlation than had been assumed a priori.

Thus, even though the "drilling" of additional boreholes in each hypothetical drilling sequence contributed more and more hard conditioning data, the revisions to the initial (unreasonably long-range) variogram models in the horizontal dimension meant that those additional measurements of fracture frequency exert a progressively diminishing sphere of influence within the model. The "plateau" of both global uncertainty measures across all drilling-related cases suggests that the drilling density thus far achieved at the MIU site, even within the drilled quadrant of the model, still is relatively insufficient to reduce global uncertainty to small values. The implication is:

5. Knowledge of the correct spatial correlation structure (variogram) exerts a very pronounced control on the uncertainty of modeling based upon limited subsurface data. Specifically, revisions to the spatial continuity model may more-or-less *completely offset* gains in information content produced by direct subsurface data acquisition. *Investments in estimating the correct spatial correlation model, and particularly in understanding the anisotropy* between the ranges of correlation in different directions, *should be particularly worthwhile* (see also item 9, below).

Demonstration of this implication number 5 would be relatively easy (although time-consuming) to accomplish. One could simply rerun each of the modeling cases considered in this study using a prior assumption of *isotopic* spatial correlation patterns (variograms) instead of the anisotropic, 5:1 horizontal-to-vertical ratio assumed a prior in the present activities. We suspect that this closer approximation to the (apparently) true spatial correlation structure from the very beginning would indicate a much more substantial decrease in global uncertainty with the addition of each successive drill hole to the various drilling sequences.

The global uncertainty associated with each modeling case has been partitioned into a portion that is related to uncertainty in the prior models of fracture frequency, principally including uncertainty related to the position of the Tsukiyoshi Fault, and uncertainty associated with the simulation process and the incompleteness of data to condition the models.

6. For modeling cases with a deterministic fault-prior model (Drilling Sequences 1, 2, and 3, as well as the final modeling case for Drilling Sequence 4), that portion of global uncertainty related to uncertainty in the fault is zero.

7. For Drilling Sequence 4, in which the position of the Tsukiyoshi Fault is progressively more constrained with each stage of drilling, *the uncertainty associated with the fault-prior model decreases as more constraints on the location of the fault at depth are added.*

However, the uncertainty associated with the simulation and with the available data has been observed to *increase* with the addition of more drill holes at the same time that the total uncertainty is decreasing. This counter-intuitive uncertainty behavior is attributed to the previously mentioned (item 5, above) changes in the spatial continuity model, or variogram, brought about by increased knowledge of spatial correlation patterns in the horizontal dimension associated with larger numbers of boreholes.

The most important contributors to *global* uncertainty that have been identified by this modeling exercise appear to be two-fold (items 8 and 9 below).

8. The basic distribution of likely fracture frequencies (the histogram) was highly uncertain prior to drilling (as the only estimate available was from outcrop studies), and that pre-drilling estimate turned out to be (apparently) quite inconsistent in representing actual subsurface conditions. Recall, however, that the original fracture frequency data from outcrop were *not* in the desired form (units of m^{-1}), and that several assumptions were required to bring the available data (units of m^{-2}) into the required format.

The standard-deviation global uncertainty measure is unquestionably greatest for Case 0, and is very much smaller for all drilling-related cases. This applies to both the full-field and the drilling-quadrant analyses. That a pronounced reduction of the standard-deviation based global uncertainty measure was obtained for Case 0a suggests that *a "reasonably accurate" global histogram is essential for a simulation-based study, in which the back-transformation of the simulated values is tied directly to that global histogram.* There is also clearly a heteroscedastic influence here, as the coefficient-of-variation-based global uncertainty measure for Case 0 was markedly different from the global uncertainty value based on the standard deviation. There is also a suspected influence of the locally varying mean incorporated into the prior estimates of fracture frequency (implication 2, above). Introduction of locally varying prior-estimated mean values definitely inserts spatial information into the modeling process, which might reasonably be expected to reduce global uncertainty. This effect was not directly investigated, however, and the existence of this effect was inferred based on indirect evidence.

9. The broad form of the spatial continuity models were demonstrated to be very influential on the global uncertainty of the final simulated models. Specifically, the *prior assumption* of relatively strong horizontal-to-vertical anisotropy based on geological inference proved to be incorrect (or at least inconsistent with later data) in the light of more advanced drilling data. The revisions to the anisotropy ratio that came with more advanced stages of drilling appear to have offset most of the gains in information obtained through that drilling, with the *apparent* result that the net reduction in uncertainty across the sequential addition of four boreholes is essentially zero. *This inference suggests that pre-drilling investigations directed toward confirming or eliminating gross anisotropy in the spatial correlation structure might have significant value.*

The impact of precisely locating the Tsukiyoshi fault in the subsurface was not as pronounced as might have been anticipated, at least on a global basis, as measured by our global uncertainty measures. However, the successive constraining of the fault location during Drilling

Sequence 4 clearly indicates some measure of progressive uncertainty reduction. Potentially the impact of a deterministic (Drilling Sequences 1–3) vs. a stochastic (Sequence 4) fault has been overshadowed in the modeling by the large error in assumed anisotropy ratio discussed in item 5, above. However:

10. It is clear that identification of the precise position of the fault may have far-reaching consequences *with respect to location-specific issues*, in distinct contrast to a simple global evaluation of overall (non-location-specific) uncertainty.

REFERENCES

Caine, J.S., Evans, J.P., and Forster, C.B., 1996, Fault zone architecture and permeability structure: *Geology*, v. 24, p. 1025–1028.

Deutsch, C.V., and Journel, A.G., 1998, *GSLIB Geostatistical software library and user's guide*, New York: Oxford University Press, 369 p.

Goovaerts, P., 1997, *Geostatistics for natural resource characterization*, New York: Oxford University Press, 483 p.

Isaaks, E.H., and Srivastava, R.M., 1989, *An introduction to applied geostatistics*, New York: Oxford University Press, 561 p.

Olea, R. (ed.), 1991, *Geostatistical glossary and multilingual dictionary*, New York: Oxford University Press, 177 p.

Yusa, Y., and Yamakawa, M., 1992, Tono in-situ research facilities for studies of the geological environment, in *29th International Geological Congress Guidebook*, field trip B18, p. B18-1–B18-9.

Yusa, Y., Ishimaru, K., Ota, K., and Umeda, K., 1992, Geological and geochemical indicators of paleohydrogeology in Tono uranium deposits, Japan, in *Paleohydrogeological methods and their applications, Proceedings of an NEA Workshop*, November 9–10, 1992, Paris, France, p. 117–146.

GLOSSARY

This glossary is intended to be a reader's guide to some geostatistical terms used within the main body of this report. Accordingly, the definitions and other explanations provided for the various words or phrases ("geostatistical jargon") are not necessarily intended as a complete, formal definition of the terms as they might be used in other situations. A comprehensive glossary of geostatistical terminology has been compiled by Olea (1991).

anisotropy ratio	the ratio between the range of spatial correlation in two different directions. In this report, the anisotropy ratio is defined as the ratio between the range of correlation in the horizontal dimension divided by the range in the vertical dimension, and invariably has a magnitude greater than 1.0.
coefficient of variation	a standard summary statistical quantity defined as the standard deviation of a sample or population divided by the mean of that sample or population. The quantity attempts to normalize the measure of variability (standard deviation) by the typical magnitude of the values involved (as represented by the average.
conditional	applied to a geostatistical process which "anchors" the resulting model to a specific set of measured (conditioning) data. Also applied in other contexts which imply that something else has already happened; i.e., the conditional probability of attribute *x* given that attribute *y* is already known.
conditional simulation	a geostatistical simulation technique in which the simulated values are "anchored" to a specific set of real-world measured data values. A conditional simulation will reproduce those measured values at those locations within the model subject to discretization limitations of the modeling grid.
conditioning data	the measured values used in a ***conditional simulation***.
conditional standard deviation	the usual standard deviation statistical measure of variability among a sample or population applied to a conditional simulation such that the quantity represents the variability among corresponding points in a suite of replicate models that are conditioned to a set of measured values.
conditional variance	see also ***conditional standard deviation***. The conditional variance is the square of the conditional standard deviation (or more precisely, the conditional standard deviation is the

square root of the conditional variance). The theoretical variance operator in this report is represented as *Var*{___}, and it is estimated empirically by both the sample and populations variances (see footnote on page 29).

E-type model — *"Expected-value model"* — a summary geostatistical model constructed from a set of replicate simulations of some type by computing the arithmetic average of all corresponding spatial locations within the model domain.

expectation, expected value — a statistical concept involving the theoretically true "central tendency" of a population. Although there a several different measures of central tendency for a given sample or population (typically listed as the mean, the median and the mode), it can be demonstrated that the arithmetic average, or mean value, is theoretically equivalent to the expectation. The theoretical expectation operator in this report is represented as *E*{___}, and the expectation is estimated empirically by the arithmetic mean.

experimental (or data) variogram — a two-dimensional plot (graph) showing one-half the average squared difference (gamma, γ) of all pairs of points separated by the same separation vector distance, $\boldsymbol{h}$. Strictly speaking this quantity is known as the "semivariogram," but because a number of different "variogram-like" measures have been defined within the geostatistical literature in recent years, the term "variogram" is becoming a more generic term.

fault-prior model(s) — in this report, this term refers to a numerical description of fracture frequency, including both "background" and "fault-related" fracture frequencies at all spatial locations within the model domain that is assumed *prior* to the actual geostatistical modeling process. The prior model represents our ***expectation*** in advance of ***conditioning*** the model to actual measured values.

Gaussian simulation — a simulation algorithm or technique in which the (spatially varying) conditional distribution of the continuous variable of interest is assumed to be completely defined by the mean and variance of a bivariate-normal (Gaussian) distribution, and in which the mean and variance of that distribution are taken as the kriged value and kriging variance respectively (the solutions to the ***kriging*** equations).

heteroscedasticity — the common statistical observation or "state of being" that measures of variability within a sample or populations (e.g., variance, standard deviation) are directly proportional to the magnitude of the values being considered. Sets of larger values are commonly observed to exhibit larger variances/ standard deviations than similar sets of smaller values (subject to the mathematical limitation that the variance is greater than one). In contrast to "homoscedasticity", in which the measures of variability are essentially uniform and independent of the magnitudes of the values being considered (a fundamental assumption underlying many statistical and geostatistical concepts).

indicator(s) — a geostatistical transformation technique in which each original data value is transformed to either a 1 or a 0 depending upon whether or not the original value exceeds or does not exceed a particular threshold value. Note that indicators may be defined in different orders (1 and 0 or 0 and 1) for different purposes.

indicator simulation — a geostatistical simulation algorithm or technique in which an indicator variable of some type is what is being generated. The indicator variable may be a categorical variable, or the indicator variable(s) may be a (set of) indicator transform(s) of an underlying continuous variable.

kriging — a weighted least-squares averaging procedure for sample data in which the weights assigned to each datum included in the estimate are computed from the variogram via the ***spatial covariance*** matrix.

modeling uncertainty — here, the uncertainty that is induced in a suite of replicate geostatistical simulations that is related to the lack of complete and exhaustive knowledge regarding a site. In contrast to measurement uncertainty, which is an issue of precision of measurement, and which is not typically addressed by geostatistics.

nesting — a term used to describe the construction of a unified ***variogram model*** by mathematical addition of the results of several, simpler underlying model types.

nugget (effect) — a ***variogram parameter*** that describes unresolvable variability at very short separation distances. A nugget effect may result from measurement uncertainty (measurement error) in the data, or, more commonly, be a reflection of the fact

	that the shortest available sample-pair spacings are larger than some type of physical control on the ***spatial correlation structure*** of the phenomenon being investigated.
prior estimate	an estimate of some quantity made prior to availability of, or without direct knowledge of, the actual value. In this report, we refer to "fault-prior models" or "prior estimates of fracture frequency" in the sense that we generate, based on available knowledge, a numerical representation of (potentially fault-related) fracture frequency prior to "drilling" a particular borehole and actually measuring the true fracture frequency.
prior information	information which is available (at a given time) used for some purpose prior to obtaining other, more specifically relevant information.
range	a ***variogram parameter*** describing the spatial distance over which the relevant spatial correlation pattern operates. Mathematically, the *range* is a variable in the equation for the ***spatial covariance***.
residuals	a common statistical term for the departures of a specific measured value from its predictor. Least-squares regression, for example, minimizes the average squared residuals from a predictor line (linear or otherwise).
sequential [simulation]	a geostatistical simulation algorithm that generates the spatially varying simulated values sequentially, one after another, along a uniquely defined random path that visits all grid nodes to be modeled within the spatial domain. Because both ***conditioning data*** and any nearby previously simulated values within a specified search neighborhood are used to estimate the spatially varying ***conditional*** probability density function from which the simulated values are then drawn at random, the sequential process is essential to the process of inducing the desired spatial correlation pattern into the resulting model.
sill	a ***variogram parameter*** that describes the amount of variability attributed to a particular ***spatial correlation pattern*** at the maximum ***range*** of spatial correlation. Mathematically, it is the result produced by an equation for the ***spatial covariance***.

simulation	a geostatistical modeling technique that emphasizes reproduction of measured data (conditional simulation) and the overall statistical character of a population of sample data, specifically the histogram and variogram. Based on concepts of random sampling from some type of distribution of values, such that each replicate simulation of a suite is statistically indistinguishable and equally likely.
simple kriging	see ***kriging*** — a variant of linear least-squares regression in which the mean value, or ***expectation***, of the regression is known (or assumed). In contrast to ordinary kriging, in which the mean value (expectation) is implicitly re-estimated at every location based on some "neighborhood" of nearby sample values.
spatial covariance	the statistical covariance matrix for a number of sample data in which the spatial (geometric) positions of those data are explicitly considered and which for the basis for the computation. The spatial covariance matrix is computable from the ***variogram model*** in a geostatistical analysis. The matrix is also used to determine the weights assigned to the various sample values in the ***kriging*** process.
surrogate	used to describe the use of one quantity to derive some other desired quantity; generally based on a (strong) regression relationship between the two variables under consideration.
uncertainty	used in this report to refer to the theoretical lack of direct knowledge about some quantity of interest, e.g., the actual fracture frequency at a specific spatial location. Alternatively, to place bounds on a particular unknown quantity. In this report, we estimate the theoretical uncertainty *empirically* by means of some computed measure of ***variability*** based on a finite number of replicate stochastic simulations.
unconditional	applied to a geostatistical process in which there is no attempt to "anchor" the model to a specific set of measured data. See ***conditional simulation***.
variability, variation	used in this report to refer to empirically observed differences among members of a suite of replicate simulations. If 100 simulations are generated, it is possible to describe, objectively and mathematically, the variability of the simulation at a specific grid node or over the entire set of grid nodes. In contrast to ***uncertainty***, which is used here as a more theoretical construct.

variogram	a somewhat generic term used to refer to the spatial correlation structure or spatial continuity patterns exhibited by a set of spatially distributed data. See ***experimental variogram*** and ***variogram model***.
variogram model	a mathematical equation or linear combination of similar equations that is used to compute the ***spatial covariance*** or describe the spatial correlation patterns/structure of a set of experimental data; a ***variogram model*** may also be assumed a priori.
variogram parameters	collectively the ***nugget***, ***sill***, and ***range*** variables that are used to describe a ***variogram model***.

Distribution

Dept. 6115 MS 0735
Susan Altman
Tom Corbet
Sean McKenna (3)
Erik Webb

Dept. 6118 MS0750
James Krumhansl

Dept. 6113 MS 0706
Chris Rautman (5)

Dept. 6852 MS-0776
Hong-Nian Jow

Dept. 6805 MS 0731
NWM Library (10)

Dept. 8945-1 MS 9018
Central Technical Files

Dept. 9616 MS 0899
Technical Library (2)

Dept. 9612 MS 0612
Review and Approval Desk for DOE/OSTI

Junichi Goto
Tono Geoscience Center
Japan Nuclear Cycle Development Institute
959-31, Jorinji, Izumi, Tokishi
Gifu T509-5102 JAPAN

Kaoru Inaba
Tono Geoscience Center
Japan Nuclear Cycle Development Institute
959-31, Jorinji, Izumi, Tokishi
Gifu T509-5102 JAPAN

Hiroaki Ito
Tono Geoscience Center
Japan Nuclear Cycle Development Institute
959-31, Jorinji, Izumi, Tokishi
Gifu T509-5102 JAPAN

Katsuhiko Maeda
Tono Geoscience Center
Japan Nuclear Cycle Development Institute
959-31, Jorinji, Izumi, Tokishi
Gifu T509-5102 JAPAN

Hitoshi Makino
Tokai Works
Japan Nuclear Cycle Development Institute
4-33, Muramatsu, Tokai-Mura
Naka-Gun, Ibaraki, 319-1194 JAPAN

Toshiyuki Matsuoka
Tono Geoscience Center
Japan Nuclear Cycle Development Institute
959-31, Jorinji, Izumi, Tokishi
Gifu T509-5102 JAPAN

Katsushi Nakano
Tono Geoscience Center
Japan Nuclear Cycle Development Institute
959-31, Jorinji, Izumi, Tokishi
Gifu T509-5102 JAPAN

Hiromitsu Saegusa
Tono Geoscience Center
Japan Nuclear Cycle Development Institute
959-31, Jorinji, Izumi, Tokishi
Gifu T509-5102 JAPAN

Atsushi Sawada
Tokai Works
Japan Nuclear Cycle Development Institute
4-33, Muramatsu, Tokai-Mura
Naka-Gun, Ibaraki, 319-1194 JAPAN

Masao Shiotsuki
Tokai Works
Japan Nuclear Cycle Development Institute
4-49, Muramatsu, Tokai-Mura
Naka-Gun, Ibaraki, 319-1184 JAPAN

Seietsu Takeda
Tono Geoscience Center
Japan Nuclear Cycle Development Institute
959-31, Jorinji, Izumi, Tokishi
Gifu T509-5102 JAPAN

Shinji Takeuchi (3)
Tono Geoscience Center
Japan Nuclear Cycle Development Institute
959-31, Jorinji, Izumi, Tokishi
Gifu T509-5102 JAPAN

Masahiro Uchida
Tokai Works
Japan Nuclear Cycle Development Institute
4-33, Muramatsu, Tokai-Mura
Naka-Gun, Ibaraki, 319-1194 JAPAN